



Modellierung von Ladungs- und Exzitondynamik in amorphen organischen Halbleitern

Zur Erlangung des akademischen Grades eines
DOKTORS DER NATURWISSENSCHAFTEN
von der Fakultät für Physik
des Karlsruher Institut für Technologie
genehmigte
DISSERTATION

von

Dipl.Phys. Franz Symalla

geboren am 05.04.1984
in Freiburg i.Br.

Tag der mündlichen Prüfung: 05. Mai 2017
Referent: (apl.) Prof. Dr. Wolfgang Wenzel (INT)
Korreferent: Prof. Dr. Gerd Schön (TFP)



Modeling of charge and exciton dynamics in amorphous organic semiconductors

Thesis for the attainment of
the academic degree
Doctor rerum naturalium Dr. rer. nat
accepted by the faculty of Physics
Karlsruhe Institute of Technology

by

Dipl.Phys. Franz Symalla

born on April 05. 1984
in Freiburg i.Br.

Date of defense: May 05. 2017
Referee: (apl.) Prof. Dr. Wolfgang Wenzel (INT)
Coreferee: Prof. Dr. Gerd Schön (TFP)

Erklärung

Ich versichere hiermit, dass ich meine Doktorarbeit selbständig und unter Beachtung der Regeln zur Sicherung guter wissenschaftlicher Praxis im Karlsruher Institut für Technologie (KIT) in der aktuellen Fassung angefertigt habe.

Ich habe keine anderen als die angegebenen Quellen und Hilfsmittel benutzt und wörtlich oder inhaltlich übernommene Stellen als solche kenntlich gemacht.

Karlsruhe, 29.03.2017

Franz Symalla

Contents

1	Introduction	1
2	Fundamentals of charge transport in organic semi-conductors	5
2.1	Electronic structure of organic semiconductors	5
2.2	Microscopic hopping rates in disordered organic semi-conductors	7
2.3	Calculation of Marcus-rates for charge and energy transport	9
2.4	Mesoscale transport models in disordered organic semi-conductors	11
3	Modelling organic opto electronic devices	15
3.1	Modelling organic light emitting diodes	15
3.2	Processes	18
3.2.1	Charge Transfer	18
3.2.2	Charge injection and ejection	21
3.2.3	Charge recombination and separation	24
3.2.4	Exciton transfer	25
3.2.5	Exciton decay and quenching	28
3.3	Microscopic parameters	35
3.3.1	Creation of amorphous morphologies	36
3.3.2	Onsite energies	38
3.3.3	Transfer integrals	42
3.3.4	Reorganization energy	43
3.4	Kinetic Monte Carlo	44
3.4.1	Propagation of particles in the organic semiconductor	44
3.4.2	Computational challenges	47
3.4.3	Kinetic Monte-Carlo state buffer	49
4	Charge carrier transport in bulk systems	53
4.1	Charge mobility in α -NPD	53
4.2	Current percolation in α -NPD	56
4.3	The Generalized Effective Medium Model	59
5	Charge transport in guest-host systems	65
5.1	Energy denominator	69
5.2	Calculation of superexchange coupling in mesoscopic morphologies	72
5.3	Superexchange in guest-host systems	72

6	Metal organic-semiconductor metal devices	83
6.1	Charge injection in disordered organic materials	83
6.2	Current voltage characteristics of α -NPD	89
7	Summary and outlook	91

Chapter 1

Introduction

Organic semiconductors (OSCs) are a class of organic materials made from conjugated small molecules (O(100) atoms) or polymers. Organic materials are usually grown as thin films which conduct charge [1] and which are often designed with optical band-gaps suitable for opto-electronic applications. Common application of these materials are as organic light emitting diodes (OLEDs)[2], organic photovoltaic cells (OPV)[3] or organic field effect transistors[4]. OLEDs are energy efficient light sources used in displays of mobile phones and flat screen televisions. With a film thickness of the order of 100 nm it is possible to create ultra thin, transparent[5] and bendable[6] displays. The major disadvantages of OLEDs compared to their inorganic counterparts are their shorter lifespan and lower brightness levels[7, 8]. Organic transistors can be utilized in inexpensive electronics, where computational performance is not crucial, e.g. as radio frequency identification (RFID) tags for logistic applications[9]. In conjunction with OLEDs, organic transistors enable the creation of electronic paper[10, 11, 12], bendable displays[6] or smart windows[13].

Organic solar cells promise a cheap and environmentally friendly alternative to inorganic solar cells[14]. Major drawback compared to inorganic solar cells is the reduced power conversion efficiency[15].

General strengths of organic electronics are scalable chemical synthesis, the low cost of the required materials[16] and if functionalized[17] appropriately the process-ability using wet chemistry methods like ink-jet printing[18] or spin coating[19]. The flexibility of the devices allow the integration of opto-electronic devices in many products as i.e. clothing [20].

Despite these advantages, several problems remain, some of which are rooted in a lack of physical understanding of the materials and devices. The major problems of OLEDs are the luminescence efficiency roll-off[21, 22, 23], color balance[24] and increased aging at high voltages[25]. Modern OLEDs are finely tuned multilayer systems, where each layer can comprise multiple organic materials serving a specific function[26, 27]. Key to build better OLEDs is a mesoscopic understanding of charge transport[28, 29, 30], which has been the focus of my research. Distribution of holes and electrons in the device determines efficiency of electron hole recombination. Exciton quenching mechanisms depend on the distribution and balance of charge carriers and excitons [31, 32]. Effective charge injection influences turn on voltage, resistance and charge carrier balance[33] in



Figure 1.0.1: A flexible OLED Display manufactured by the Korean manufacturer LG (source: www.digitaltrends.com)

the device.

Theoretical tools for the quantitative and material specific prediction of transport properties can support the development of improved and evermore complex materials and devices. A complete model has to account for hole and electron injection/ejection, charge propagation, electron-hole recombination and dissociation, exciton transport, exciton decay as well as interactions between the particles in the simulation[34].

Although the fundamental processes of charge and energy transport are understood, a predictive and detailed quantitative model of charge and exciton transport and interactions is lacking on the microscopic and mesoscopic scale.

The problem of a device simulation with molecular resolution is for one thing the required size of a realistic representation of the system, and for another thing numeric bottlenecks in the simulations due to a spread of timescales of the transport processes in strongly disordered systems over tenth of orders of magnitude. In my work I have developed a kinetic Monte-Carlo protocol to simulate charge and exciton transport in mesoscopic samples and devices of amorphous organic semi-conductors, which alleviates prohibitive numerical bottlenecks inherent to kinetic Monte Carlo simulations in strongly disordered systems. To allow the simulation of realistic systems, I developed methods to create realistic device representations on the 100 nm scale based on atomistic and quantum chemical calculations.

In chapter 2 of this thesis I give a fundamental background of charge and exciton transport in disordered organic semiconductors . In chapter 3.2 I detail a device model comprising processes and the corresponding rate expressions which are relevant for OLED and OPV simulation, including expressions for charge injection rates as well as charge separation and recombination rates free of heuristic parameters.

As rates for all processes in a mesoscale device can not be determined by ab-initio models, I introduce a stochastic expansion method to create a meso scale material model based on small atomistic morphologies and quantum chemical calculations in chapter 3.3. The calculation of coulomb interaction between charges in an amorphous device is a very prohibitive factor for device calculations as the coulomb potential on off-lattice sites has to be determined by a computational expensive ewald sum. I therefore present

a calculation scheme to efficiently calculate coulomb interaction in the given boundary conditions of an OLED.

The numerical convergence of kMC calculations is problematic for systems involving deep trap states, such as host-guest systems or materials with high energy disorder, due to rate distributions varying by 20 orders of magnitude. To ease this problem, I present an algorithm for the computational acceleration of state space sampling in strongly disordered systems in chapter 3.4. This algorithm accelerates kinetic Monte-Carlo simulations the more, the worse different segments of state space are connected, thus effectively enabling kinetic Monte-Carlo simulations in system with deep traps or high disorder.

To validate the transport model, I calculate field and temperature dependent hole mobilities in bulk systems of the prototypical hole transport material α -NPD in chapter 4. In this chapter I also discuss an alternative transport model for the estimation of bulk mobilities developed in collaboration with Sony [35].

In Chapter 5, the transport model is applied to investigate charge transport in two component light emission materials as used in OLEDs[36]. These materials consist of a small concentration of phosphorescent dyes in a host matrix of charge transport molecules. The dyes thereby act as traps for both charges and excitons. I show that direct transport from dye to dye is enhanced by an order of magnitude by taking into account transitions through virtual states on the host molecules[36].

To investigate the mechanism of charge injection I calculate current voltage characteristics in a device of α -NPD sandwiched between two gold electrodes and validate the results against experiment in chapter 6. Using an ab-initio based injection model I obtain good agreement with experimental IV-characteristics. I show that charge injection at high voltages is enhanced by 4 orders of magnitudes if the charge injection from the electrode uses virtual states of α -NPD molecules at the interface of electrode and the organic material.

The Formalism and methods introduced in this thesis were also employed in other works not presented in this thesis. The superexchange formalism and the kinetic Monte-Carlo program written for this thesis were used to calculate mobilities of metal organic frameworks(MOF) loaded with organic molecules[37]. In this work it is postulated that the conductivity of these systems is enhanced by hopping from dopant to dopant molecule through virtual states on the MOF. The methods to generate mesoscale morphologies and transfer-integrals which I introduced in Chapter 3.3, were applied in several other works which are not discussed in this thesis. [38, 39] solve the stationary Master-equation of rates calculated with aforementioned methods to obtain temperature, field and density dependent mobilities of pure organic materials. In [39] an mobility enhancement at high fields is observed if transfer integrals involving molecular superexchange are taken into account. In [40] the time dependent Master-equation is solved to predict impedance spectroscopy data in good agreement with experiment.

Key-result of this work is the development of a numerically efficient method to calculate charge transport in small molecule based organic semi-conducting materials which

correctly predicts both bulk mobilities and device characteristics based on microscopic input parameters obtained by parameter free morphology and electronic structure models. Using this method the relevance of charge transfer hops through virtual states on bridging molecules is demonstrated for light emission layers used in OLEDs as well as for charge injection at the metal organic interface. The introduced method can be applied to simulate microscopic processes in OLED and OPV devices and identify microscopic bottlenecks to the device efficiency.

Chapter 2

Fundamental principles of charge transport in disordered organic electronics

In this chapter I will give a fundamental background on charge and exciton transport in disordered organic semiconductors. Section 2.1 gives a summary of the electronic structure of disordered organic materials which leads to hopping transport between strongly localized states. Section 2.2 introduces Miller-Abrahams and Marcus hopping rates. The calculation of Marcus rates for charge and energy transport using quantum chemical methods is discussed in section 2.3. Section 2.4 gives a brief overview of charge transport on the meso-scale.

2.1 Electronic structure of organic semiconductors

Organic semiconducting materials usually consist of non covalently bonded organic small molecules or polymers, mostly comprised of first and second row elements. Thin films of these molecules can be made by vacuum sublimation[41] or by various solution processing methods such as spin-coating[19], or inkjet printing[18]. Solution processing requires solubility of the molecules, a prerequisite not given for most small molecules, but readily achievable by engineering soluble sidechains[42, 17].

Cause for the conductive properties of organic molecules is an aromatic backbone of sp^2 bonded carbon atoms. While three of the four valence electrons of carbon form strong σ bonds with neighboring carbon atoms, the remaining electrons occupy delocalized out of plane π orbitals which are formed by hybridization of the p_z orbitals of the carbon atoms (see fig. 2.1.1). With an increasing number of carbon atoms, the energy levels of the delocalized π orbitals would get closer until they form a quasi continuum of states i.e. an energy band (e.g. graphene). The limited size of small molecules however results in a discrete spectrum of states on each molecule. In aromatic polymers, localization of π orbitals on partial segments of the backbone is caused by dihedral rotation leading to destructive interference between rotated p_z orbitals[43, 44].

In small molecule systems, the mostly Van-der-Waals bonded molecules often form an

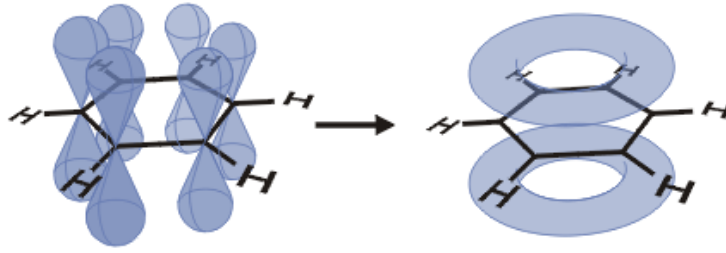


Figure 2.1.1: left: 6 rotational symmetric p_z orbitals of individual carbon atoms in benzene. right: Hybridization leads to delocalized orbitals (image license: wikimedia commons)

amorphous material. The irregular stacking of molecules leads to unique morphological electronic boundary conditions for each molecule, which result in a Gaussian distribution of the corresponding energy levels of different molecules in the morphology[45].

$$D_s(E) = \frac{n}{\sqrt{2\pi}\sigma_s} e^{-\frac{(E_s-E)^2}{2\sigma_s^2}} \quad (2.1.1)$$

where E_s is the average value of a given energy level s over all molecules, σ_s the standard deviation of the distribution and n the density of molecules. This disorder of electronic states and the weak coupling between the π -systems of different molecules leads to Anderson localization on the individual molecules[46]. On the individual molecules the π -orbitals stay delocalized and can accommodate additional electrons in unoccupied π -orbitals or allow for the removal of electrons from an occupied π orbital. The wavefunction overlap between π orbitals on different molecules then allows for hopping of this charge from molecule to molecule. In structures of highly ordered organic molecules, band transport is possible for molecules with a large enough electronic coupling [47].

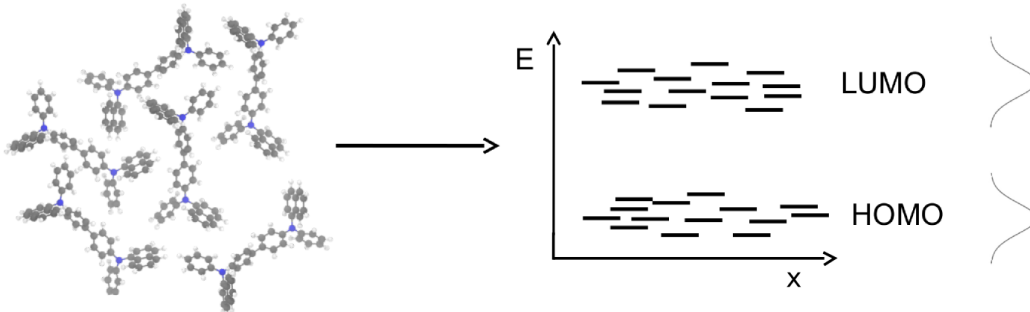


Figure 2.1.2: Schematic distribution of energies of the highest occupied and lowest unoccupied molecular orbital in amorphous organic semiconductors. Standard deviation of the energy disorder of typical hole conductors is $O(0.1 \text{ eV})$

2.2 Hopping rates in disordered organic semiconductors

Strong localisation of the electronic states on individual molecules means that transport will be the result of a succession of hops from one quasi stationary state to another quasi stationary state[46, 45]. One electron states on different small molecules are weakly coupled, such that the hopping rate can be calculated by Fermi's Golden rule[48, 49]:

$$\omega = \frac{2\pi}{\hbar} \sum_i \sum_f p_i \langle \Psi_f | H | \Psi_i \rangle^2 \delta(E_f - E_i) \quad (2.2.1)$$

where i,f denote final and initial states, p is the occupation probability of the initial state, $\langle \Psi_f | H | \Psi_i \rangle$ wavefunction coupling between final and initial states and $\delta(E_f - E_i)$ the resonance condition of the transfer. For charge or energy transfer between disordered molecules, the resonance condition is only met if energy is supplied or dissipated by molecular vibrations. If the ionic contribution of the expression are factored out and treated classically, an approximation is given by the Arrhenius type Miller-Abrahams rate[50]:

$$\omega_{if} = \omega_0 J_{if}^2 \begin{cases} \exp(-\Delta E_{if}/(k_B T)) & \text{if } \Delta E_{if} > 0 \\ 1 & \text{else} \end{cases} \quad (2.2.2)$$

where i,f denote initial and final electronic state, J_{if} the electronic coupling, ΔE_{if} the energy difference of final and initial electronic state, T the temperature and k_B the Boltzmann constant. For hops upwards in energy the resonance condition is met if the initial state gets thermally excited into a higher vibrational state, the probability of which is given by the Boltzmann factor. For hops downward in energy, this expression assumes that any amount of energy can be dissipated. In molecular systems this is not the case if ΔE_{if} is much bigger than the vibrational frequencies of the molecule. This rate expression is used to describe charge hopping from impurity to impurity in crystalline organic semi-conductors[51], where continuous amounts energy can be absorbed in electronic degrees of freedom but is also used to describe charge transfer in molecular organic semiconductors [52, 53]. Though individual rates for downward hops are systematically overestimated, measured quantities like charge mobility will only be little affected by this, as the charge transport bottlenecks are upward hops.

A more sophisticated hopping rate for molecular charge transfer was derived by Marcus [54, 55]. Marcus considered that the conformational response upon the charging of a molecule, both from the molecule itself and from a polarisable environment, creates an energy barrier for the charge transfer to another molecule, as the system is in a conformational state which accommodates the electron on its current molecule while a conformational reorganization to accommodate the electron on the other molecule is a slow process. In addition to this energy barrier, the Frank-Condon principle makes a transition of the electron from molecule A to B while in a conformation which accommodates the charge state on A very unlikely.

The conformational state of the system however fluctuates thermally. Marcus theory states that at some point the system will fluctuate in a conformational transition state

in which the states of either molecule being charged are in resonance, such that energy conservation and Frank Condon principle for a transition are observed. The energy barrier for the charge transfer is then given by $E_T - E_A$, where E_T denotes the energy of the entire system in the transition state and E_A the energy of the system in the ground state if the charge sits on molecule A. For weak electronic coupling between the charge states on molecule A and B and with the approximation of harmonic conformational degrees of freedom, the height of the injection barrier was derived as [48, 54]:

$$E_T - E_A = \frac{(E_B - E_A + \lambda)^2}{4\lambda} \quad (2.2.3)$$

for charge transfer in solids E_A/E_B is the ground state energy of the system if the charge sits on A/B and λ is the so called reorganization energy. The reorganization energy is given by

$$\lambda = \frac{1}{2} \sum_j k_j (Q_j^A - Q_j^B)^2 \quad (2.2.4)$$

where Q_j^A and Q_j^B are the equilibrium values of the j th normal mode coordinate Q and k a reduced force constant $2k_j^A k_j^B / (k_j^A + k_j^B)$, which for identical molecules is the energy that has to be paid to bring the system where molecule B is charged in the conformational state it would have if molecule A was charged. This is illustrated in fig 2.2.1 for a one dimensional reaction coordinate.

Marcus formulated his rate by using the Boltzmann occupation ratio of the resonant

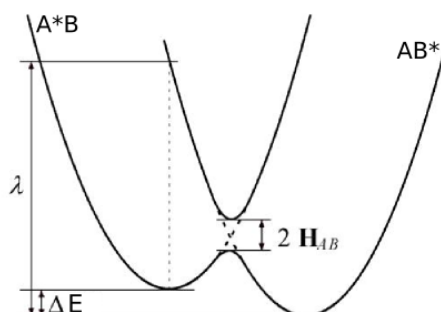


Figure 2.2.1: Crossing parabola of the potential energies of a molecular dimer if molecule A is charged (left parabola) and if molecule B is charged (right parabola) as function of a 1-dimensional conformational reaction coordinate. To obey energy conservation and Frank-Condon principle a charge transfer has to go through the transition state, where both parabola cross. The reorganization energy λ is visualized as the energy required to bring the system charged in state B into the equilibrium conformation the system has when molecule A is charged. (image license: wikimedia commons)

transition state as:

$$\omega_{if} = \frac{2\pi}{\hbar} |J_{if}|^2 \frac{1}{\sqrt{4\pi\lambda k_B T}} \exp\left(-\frac{(\lambda + \Delta E)^2}{4\lambda k_B T}\right). \quad (2.2.5)$$

where $\Delta E = E_B - E_A$.

2.3 Calculation of Marcus-rates for charge and energy transport

This section details how to calculate Marcus hopping rates for charge and exciton transport in realistic systems using quantum chemical methods. To this end reorganization energy λ , transfer integral J_{if} and energy difference ΔE have to be evaluated.

charge transfer The reorganization energies λ of a charge transfer between two molecules of the same type can be calculated using Nelson’s four point procedure [56] employing Density Functional Theory (DFT).

- calculate the total energy E_1 of a conformationally relaxed molecule in vacuum.
- add an electron to the molecule and calculate the total energy E_2 in the structure from step 1.
- relax the structure of the charged molecule and calculate the total energy E_3
- remove the additional electron and calculate the total energy E_4 in the structure from step 3
- $\lambda = (E_2 - E_3) + (E_4 - E_1)$

For charge transfer between molecules of a different type I approximate the reorganization energy as $\lambda_{I,II} = \frac{1}{2}(\lambda_{I,I} + \lambda_{II,II})$, where $\lambda_{I,I}$, $\lambda_{II,II}$ are the reorganization energies between two molecules of type I and two molecules of type II respectively.

To obtain the energy difference $\Delta E = E_B - E_A$ of final and initial state of a hole transfer, on-site energies E_A and E_B are taken as the eigenvalues of the highest occupied molecular Kohn-Sham orbital (HOMO) of each molecule. For electron transport rates, on-site energies E_A and E_B are taken as the eigenvalues of the lowest unoccupied molecular Kohn-Sham orbital (LUMO). The electronic coupling J_{ij} was calculated as [57]:

$$J_{ij} = \frac{\hat{H}_{ij} - \frac{1}{2}(\hat{H}_{ii} + \hat{H}_{jj}) S_{ij}}{1 - S_{ij}^2} \quad (2.3.1)$$

\hat{H}_{ii} is the HOMO(LUMO) eigenvalue of molecule A, \hat{H}_{jj} the HOMO(LUMO) of molecule B, \hat{H}_{ij} is the matrix element between the HOMO(LUMO) orbitals on A and B,

$$\hat{H}_{ij} = \langle \varphi_i | \hat{H}_{KS} | \varphi_j \rangle \quad (2.3.2)$$

where \hat{H}_{KS} is the effective one electron Hamiltonian of the (neutral) dimer system and $\varphi_{i,j}$ are the HOMO(LUMO) orbitals of molecule A and B, which are each extended with zeros on the basis function of the respective other molecule to match the Hilbert space of the dimer Hamiltonian. S_{ij} is the overlap matrix element of the extended HOMO(LUMO) orbitals.

$$S_{ij} = \langle \varphi_i | \varphi_j \rangle \quad (2.3.3)$$

The overlap is nonzero as the basis-functions of A and B are non-orthogonal.

Environmental effects on electronic structure calculations The disordered arrangement of molecules leads to unique electrostatic environment for every molecule. To take this into account, energy eigenvalues and orbitals of the molecules in a given amorphous morphology are calculated using the Quantum Patch method [58, 59]. The electronic structure of the molecules is thereby equilibrated by coupling single molecule DFT calculations of all molecules by the electrostatic potential resulting from the charge densities of all calculations. Practically this is done in an iterative procedure that calculates the ground state charge density of each molecule, then fits point charges on the position of all atoms of a molecule to reproduce its electrostatic potential. In the next step all molecules are exposed to the point charges of the other molecules and the new molecular ground states are calculated. This procedure is repeated until the ground state energy of all molecules in the system is converged to a given accuracy. The dimer Hamiltonians are then calculated by performing one DFT calculation for every dimer in the equilibrated electrostatic environment.

Excitation energy transfer Strongly localized Frenkel excitons lead to a conformational reorganization with a reorganization energy of $\lambda > k_B T$. Here the formalism of Marcus theory can also be used to obtain an approximation of intermolecular exciton transfer rates[57]. E_A and E_B in 2.2.5 are then excitation energies of the final and initial states on molecule A and B. For the total energy transfer rate a sum over the rates to many final states has to be taken as written in 2.2.1. The reorganization energy for the energy transfer can be calculated with Nelsens four point procedure by exciting instead of charging the system. In the regime of weak electronic coupling, the matrix element J_{if} of the exciton transfer can be written as [49]:

$$J_{if} = \langle \Psi_A^* \Psi_B^0 | V_{Coul} | \Psi_A^0 \Psi_B^* \rangle \quad (2.3.4)$$

where the final and initial state wavefunction are approximated as a (implicitly antisymmetrized) product of the mono-molecular wavefunctions Ψ_A and Ψ_B in their excited (*) and unexcited state. For illustration purposes let us now consider a two electron system, one spinless electron per molecule. Let one electron be in the HOMO orbital on molecule B and the other (excited) electron in a LUMO orbital of molecule A, both in the frozen meanfield potential of the full system. The wavefunction of the initial state of the energy transfer is then $\Psi_i = \Psi_A^* \Psi_B^0 = \frac{1}{\sqrt{2}}(\varphi_{A,L}^I \varphi_{B,H}^{II} - \varphi_{A,L}^{II} \varphi_{B,H}^I)$ where L/H denotes the LUMO/HOMO respectively and I/II are the electron coordinates. With the wavefunction of the final state $\Psi_f = \Psi_A^0 \Psi_B^* = \frac{1}{\sqrt{2}}(\varphi_{A,H}^I \varphi_{B,L}^{II} - \varphi_{A,H}^{II} \varphi_{B,L}^I)$ the electronic coupling becomes

$$\begin{aligned} J_{if} &= \frac{1}{2} \langle \varphi_{A,L}^I \varphi_{B,H}^{II} - \varphi_{A,L}^{II} \varphi_{B,H}^I | V_{Coul} | \varphi_{A,H}^I \varphi_{B,L}^{II} - \varphi_{A,H}^{II} \varphi_{B,L}^I \rangle \\ &= \langle \varphi_{A,L}^I \varphi_{B,H}^{II} | V_{Coul} | \varphi_{A,H}^I \varphi_{B,L}^{II} \rangle - \langle \varphi_{A,L}^I \varphi_{B,H}^{II} | V_{Coul} | \varphi_{A,H}^{II} \varphi_{B,L}^I \rangle \end{aligned} \quad (2.3.5)$$

If spin were considered in formulating the wavefunctions, the final expression would look the same except for a factor of 2 before the first term of the sum. The first part of the sum

describes an transfer of the electron in the LUMO of molecule A to the HOMO on molecule A simultaneously with the transfer of the an electron from the HOMO of molecule B to the LUMO of molecule B. This correlated excitation/deexcitation requires no orbital overlap between the molecules and is called Förster transfer[60]. If the molecules are far apart the leading term of the coulomb interaction between the HOMO-LUMO overlap density on molecule A and the HOMO-LUMO overlap density on molecule B will be the dipole term, such that the electronic coupling can be approximated as the coulomb interaction energy of the dipole of the overlap densities of molecule A with the dipole of the overlap density of molecule B.

$$\langle \Psi_A^* \Psi_B^0 | V_{Coul} | \Psi_A^0 \Psi_B^* \rangle \approx \kappa \frac{|\vec{d}_A| |\vec{d}_B|}{|r_{AB}|^3} =: V^{dd} \quad (2.3.6)$$

where \vec{d}_A and \vec{d}_B are the dipoles of the overlap densities of the single molecular excitations, r_{AB} the intermolecular separation and κ an orientation factor, which reflects the relative orientation of the two transition dipoles with respect to the intermolecular separation axis. To practically calculate this rate the transition dipole (of the mono molecular many-electron systems) can be directly obtained from a TD-DFT calculations. The second part of the sum of eq.2.3.5 describes an transfer of the electron from the LUMO of molecule A to the LUMO of molecule B with a simultaneous electron transfer from the HOMO of molecule B to the HOMO of molecule A, which is referred to as Dexter transfer[61]. As this transfer requires wavefunction overlap between the molecules, it is only possible if the molecules are close to each other. If the coupling between the molecules is weak, this term will also be very weak. In the case of triplet excitons, Förster transfer is forbidden by the Pauli-exclusion principle, i.e. the triplet can not deexcite without a spinflip. Dexter transfer is however still possible, as the charge transfer from HOMO to HOMO can happen from either the spin-up or spin-down electrons in the acceptor HOMO.

2.4 Mesoscale transport models in disordered organic semi-conductors

The microscopic hopping rates discussed in the previous chapter lead to diffusive transport in the organic material. As hops have to overcome a hopping barrier due to the energy disorder of electronic states on different molecules and the conformational change the molecules undergo upon changing their charge state, the hopping process is only possible by absorbing thermal energy. Due to eq. 2.2.5 hops upwards in energy are exponentially stronger suppressed than hops down in energy. As the number of hopping targets grows quadratic with the distance from the molecule, there is a trade-off between short hopping distances which increase the electronic coupling and long hopping distances which increase the chance to find a target state with a low energy[46].

At low charge concentrations, the equilibrium density of occupied states $n(E)$ is given by

$$n(E) = D(E) \frac{1}{1 + e^{(E-E_F)/k_B T}} \quad (2.4.1)$$

where $D(E)$ is the density of states of HOMO-energies for the distribution of holes and LUMO energies for the distribution of electrons, E_f is defined as the energy of the lowest unoccupied state. For high charge densities the tail of the Gaussian density of states $D(E)$ is filled, so that E_f is increasing. Fig. 2.4.1 illustrates the density of HOMO levels occupied by holes depending on energy. Only the tail states of the distribution are occupied, which restricts possible path for hopping transport to few sites.

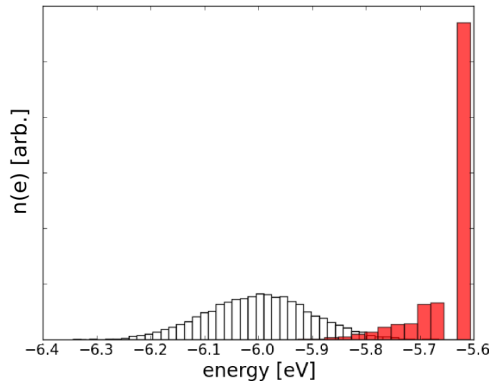


Figure 2.4.1: The normalized HOMO-energy distribution in a 8000 molecule system with a HOMO disorder of $\sigma = 4k_B T$ is shown in white. In red the the time averaged distribution of states occupied by holes. A single tail state at the right is occupied the majority of the time.

The higher the energy disorder, the smaller the number of molecules to which hopping transport is not suppressed by the Boltzmann factor of the Marcus rate equation 2.2.5. This means that there are hopping path through the system with strongly varying resistance. The major contribution to the charge transport comes from a small set of percolation path. As the energy disorder reduces the hopping connectivity, the number of percolation path becomes smaller with increasing energy disorder[62]. In fig. 2.4.2 this is illustrated for four $50 \times 50 \text{ nm}^2$ networks of hopping sites with energy disorder between $2-5k_B T$.

The percolative nature of the charge transport means, that the representation of the system needs to be sufficiently large to sample the percolation path which defines the conductance of the system[63]. From fig. 2.4.2a) it seems apparent, that a different random distribution of site energies would lead to a different percolation path with a different resistance.

Masse et. al.[63] found a power law-dependence of the conductance fluctuation $\delta(L) = (\frac{L_0}{L})^\kappa$ on the lengthscale L of the system representation. The edge length of the cubic system L_0 , at which conductance fluctuations are of the order of the mean conductance, is found to depend on the energy disorder of the system as $L_0 \propto \sigma^\nu$. The exponent ν depends on topology and used rate-equation but was for all considered cases found to be between 0.85-0.89. κ was for all considered systems found to be 1.52.

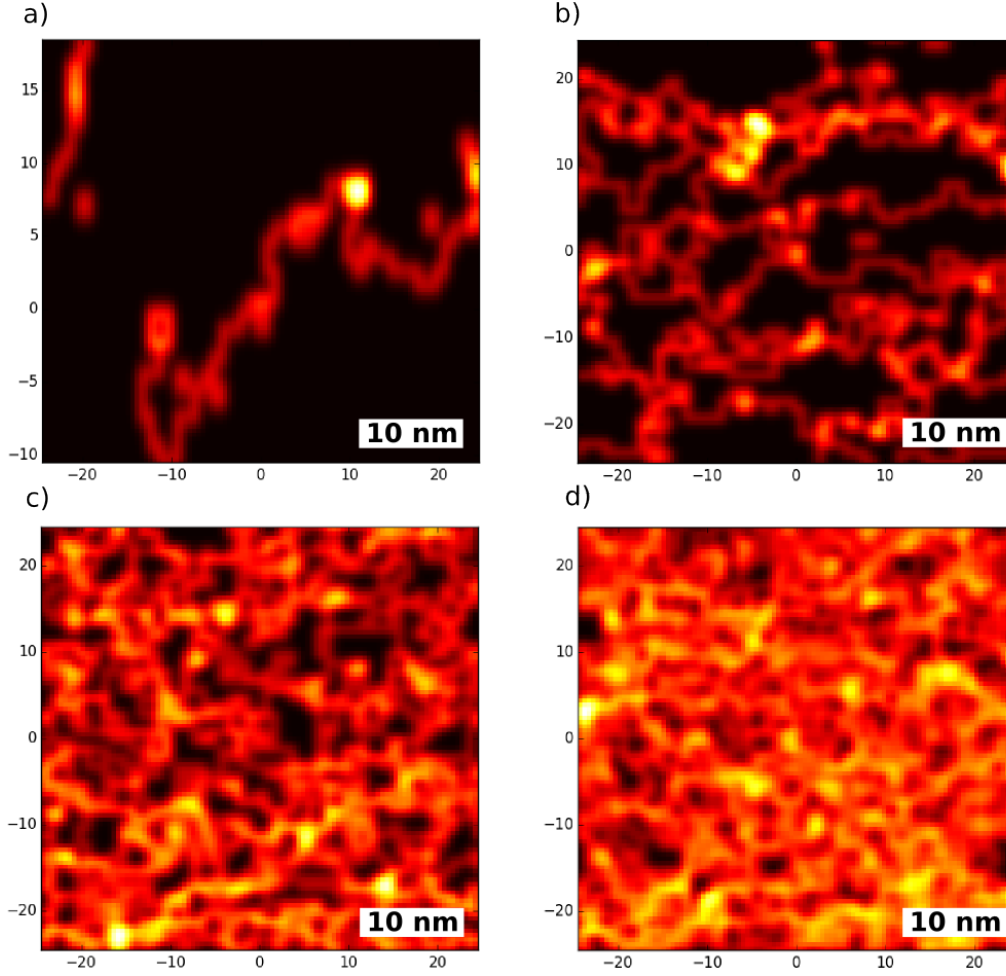


Figure 2.4.2: Hole current densities in a periodic network of hopping sites with varying disorder σ of HOMO energies, obtained by kinetic Monte-Carlo simulations (see Chapter 3.4). The current flows through red areas. $\sigma = 5k_B T$: One path of hole conduction is visible. The hotspot is a well connected sub-network in which random ring-currents occur. b) $\sigma = 4k_B T$ the number of current pathways increases. c) $\sigma = 3k_B T$ d) $\sigma = 2k_B T$ Most hopping sites in the system can be reached.

Given a temperature $T \gg 0$ and a finite concentration of charge carrier in an organic semiconductor, the charge carriers will diffuse in the system by randomly hopping from molecule to molecule. Applying an electric field F will reduce hopping barriers in the rate equation 2.2.5 in direction of the field and lead to a drift of the charge carriers in field direction. The non-zero average drift velocity $\langle v(F) \rangle$ then allows to define the mobility μ of the material as

$$\mu(F) = \frac{\langle v(F) \rangle}{F}. \quad (2.4.2)$$

To calculate mobilities in this kind of system, Bässler [64, 65] applied a kinetic Monte-Carlo (KMC) protocol, which simulates the random diffusion of (independent) electrons. He modeled the organic semiconductor as a cubic lattice with a Gaussian distribution of

energies where each node represents a molecule, and found a disorder dependence of the mobility of:

$$\mu(F = 0) = \mu_0 e^{-\frac{4}{9}\sigma^2} \quad (2.4.3)$$

where σ is the reduced disorder strength.

The strength of an explicit Monte-Carlo simulation is that it can be extended to take into account charge creation and the interaction of electrons, holes and excitons. Later works include charge injection rates to simulate current voltage characteristics of organic semi-conductors[62, 34] and electron hole recombination to simulate the operation of full OLED[28, 66, 67, 67] or OPV devices [68, 69]. The Monte-Carlo device simulations are usually performed on simple cubic lattices, where hopping parameters are fit to reproduce experimentally measured data.

In other work, charge transport calculations were performed based on microscopically generated amorphous morphologies, where hopping parameters were calculated using quantum chemical methods [70, 71]. The size of systems for which quantum chemical calculations can be performed are however well below the system sizes relevant to capture percolation effects. To solve this Problem Andrienko et al. suggested methods to extrapolate quantum chemical parameters to meso-scale systems[72, 73].

A numerically often more stable approach to obtain charge transport related expectation values is to solve the steady state[52] or time dependent [40] Master-equation for all pairs of molecules in a 3d morphology. The draw backs of these methods lie in the realm of application as explicit particle interactions can not be included.

Chapter 3

OSC Device modelling

In this chapter I will present a model to simulate the operation of OLED or OPV devices by explicit creation, propagation and annihilation of individual electrons, holes and excitons in a material or device. Before detailing the transport model I will review design principles and performance critical processes in OLEDs in chapter 3.1 to motivate the computational modeling. In Chapter 3.2 I will present rate equations for all processes which I consider in the device simulation. In the following Chapter 3.3 I will then show how a mesoscopic representation of a realistic system can be created based on atomistic and quantum chemical simulations, and how the parameters required for the calculations of the transition rates can be calculated. In Chapter 3.4 I will introduce the kinetic Monte-Carlo algorithm used to propagate the system state based on the calculated rates. I will further discuss the pitfalls of kinetic Monte Carlo simulations in highly disordered systems and introduce numerical tools to alleviate performance and convergence problems of the kinetic Monte Carlo algorithm.

3.1 Modelling organic light emitting diodes

Optoelectronic devices such as OLEDs or OPVs consist of thin films of amorphous materials made up of various types of organic molecules, which serve different purposes in the device[34]. Fig. 3.1.1 shows an energy level diagram of a typical white OLED. At the right-most of the stack is the p doped hole injection layer NHT5:NDP2 attached to a transparent Indium tin oxide electrode (not shown). The ionization potential of most organic semiconductors is higher than the workfunction of indium tin oxide or similar electrodes, resulting in a hole injection barrier between electrode and organic material[74, 75, 76, 77]. In the hole injection process, holes from the electrode hop to localized states on the organic molecules. Due to the energy disorder of the OSC, the hole injection barriers vary for a typical OSC by 5-10 times room temperature, such that injection into the material is locally inhomogeneous[78, 79]. The inhomogeneous molecular ionization potentials further lead to a spatially inhomogeneous distribution of charge in thermal equilibrium. Due to the weak electrostatic screening in the OSC (typical relative permittivity $\epsilon_r = 4$ [80]) the electric field of the injected charges will further affect injection barriers. From the injection layer, holes transfer through a hole transport and electron blocking layer to a red light emission layer. In the emission layer a part of the holes will form tightly bound

excitons, which will ideally decay radiatively to emit light, with electrons coming from the cathode, while the remainder of the holes has to travel to the green and blue emission layers. Emission layers are often made as host-guest systems which consist of a mixture of 85%-99% charge transport molecules and 1% - 15% light emitting molecules [81, 82]. The correct emitter concentration is thereby a sensitive trade-off between competing effects, which are adversarial to the device operation [67]. Emitter molecules are designed as traps for excitons in order to reduce exciton quenching by an energy transfer to excited or charged molecules [83, 84]. When an electron and a hole form a molecular exciton it will in three of four cases be a spin triplet due to spin statistics. In order to harvest light from the triplet excitons, emitters commonly include heavy metals such as iridium to facilitate intersystem crossing between singlet and triplet which allows radiative decay of the exciton in the order of microseconds [85, 86, 87]. To reduce energy transfer of the triplets to other excitons or charges in the system, triplet diffusion is reduced by lowering emitter molecule concentration, as an energy transfer to the host is energetically unfavorable. Conversely, a percentage of holes has to reach the emission layers for different colors. As the emitters also act as charge traps, thickness of the layer and emitter concentration have to be balanced to ensure a possibility of charge percolation through the layer [88]. In the design of the OLED it has to be further factored in to have a balanced concentration of holes and electrons in the emission layers [89, 90] to ensure efficient exciton formation, as a high concentration of free charge increases the likelihood of energy transfer from excitons to charged molecules, where the energy can be dissipated thermally due to a dense density of states of the charged molecule or trigger degradation effects [91, 92]. In modern OLEDs hole and electron blocking layers are used to improve charge carrier balance and luminescence efficiency [93]. Considering the complexity of the trade-offs existing in OLED stack design and having in mind that transport, especially through layers consisting of multiple molecular species, is percolative in nature and strongly depends on charge concentration [52], it is apparent that simulation of the interdependent processes in the OSC may bolster the understanding and development of complex organic semiconductors. In prior work, lattice based experimentally parametrized kinetic Monte-Carlo device models successfully reproduced current-voltage characteristics of OLEDs and OPV devices [34, 68]. In other works, kinetic Monte-Carlo charge transport calculations of pure organic material samples have been performed based on microscopic information obtained by quantum chemical methods [70, 71]. This work sets out to improve existing [34, 72] and develop new simulation methods to predict charge and energy transport in complex organic semi-conductor systems. New aspects in particular are ab-initio based rate expressions for injection, charge separation and charge recombination processes, a method to generate transfer integrals for samples containing $O(10^6)$ molecules, an accelerated kinetic Monte-Carlo protocol for highly disordered systems and efficient routines for the evaluation of the coulomb potential in off lattice systems.

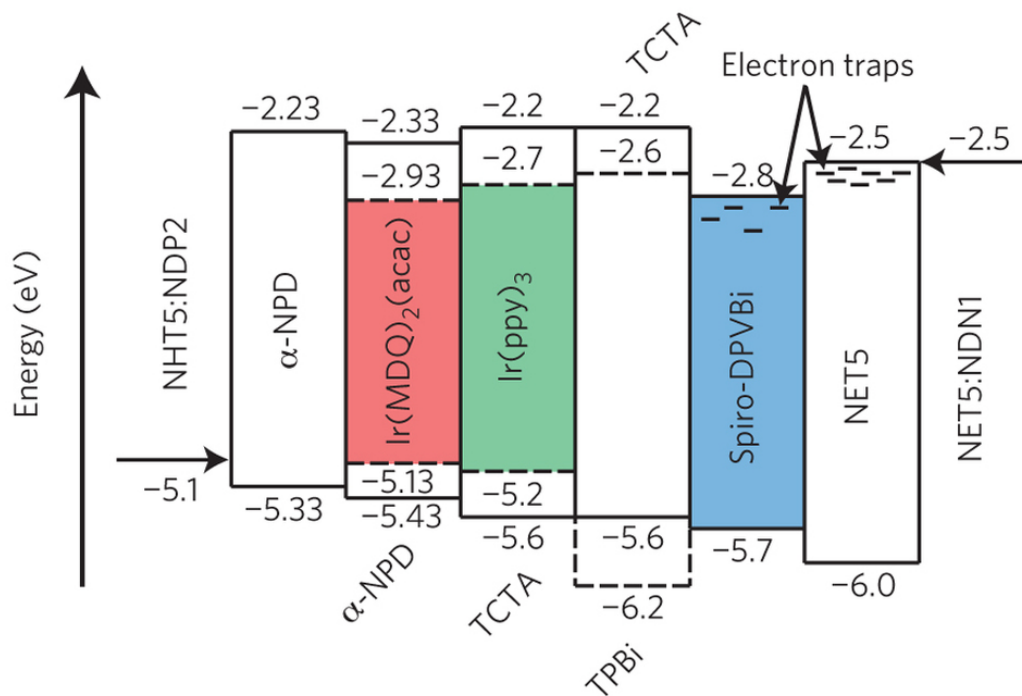


Figure 3.1.1: Band diagram of a multilayer stack of organic thin films, which acts as a white light emitting diode [34]. Electrons enter from the right, holes from the left. Dashed lines in the band diagram represent the HOMO/LUMO levels of the minority component of the thin films made of two molecular species. The majority component serves as charge transport molecule, the minority component as light emitter. The color in the figure represents the color of the emitted light. The left most layer is attached to a transparent indium tin oxide layer. Light emission takes place on blue fluorescent dye to the right and in red and green phosphorescent emission layers to the left. (image source: [34])

3.2 Processes

In the following section, all processes and their corresponding rates included in the device simulation are detailed. Rate expressions are based on microscopic properties of the system avoiding heuristic rates wherever it seems feasible to obtain the microscopic information which is required for an ab-initio based rate from quantum chemical or other theoretical tools.

Charge carriers and excitons in disordered organic semiconductors are strongly localized and states on different molecules are weakly coupled (see Chapter 2). Thus, we model the time propagation of charge and energy in the device as a succession of discrete and independent events (*e.g.* charge hopping processes or exciton decay), which are described by transition rates of the individual processes. Fig. 3.2.1 gives an overview of the processes which I consider for the device simulation of an OLED. Charge injection, ejection and transport, electron-hole recombination (generation of Frenkel-excitons or direct annihilation), exciton transport and charge separation are included in the simulations. Explicitly included exciton quenching mechanisms are radiative decay and energy transfer to charges or other excitons. In the model implicitly included exciton quenching mechanisms are interface and impurity quenching processes. In practice, none of the systems investigated in this thesis include molecules (impurities) with inter-band gap states. A discussion of further exciton quenching mechanisms can be found in Section 3.2.5

3.2.1 Charge Transfer

Rates of charge hopping processes between states ψ_i^A and ψ_j^B , where an additional electron (or hole) is localized on either molecule A or molecule B are estimated using Marcus theory (see Section 2.2).

$$\omega_{ij} = \frac{2\pi}{\hbar} |J_{ij}|^2 \frac{1}{\sqrt{4\pi\lambda_{ij}k_B T}} \exp\left(-\frac{(\lambda_{ij} + \Delta E_{ij})^2}{4\lambda_{ij}k_B T}\right). \quad (3.2.1)$$

where $J_{ij} = \langle \psi_i | H | \psi_j \rangle$ is the electronic coupling between the states, λ the reorganization energy of the charge transfer and ΔE_{ij} the energy difference between state i and j (calculation details in Section 3.3). Weak electronic coupling ($J_{ij} < k_B T$) and energy disorder lead to typical hopping rates in the order of 10^9s^{-1} . Thus, I assume electrons and holes to have ample time to relax to the local ground state before the next hop, such that I always assume ψ_i to be the state with lowest energy on the molecule from which the hop originates. For the state ψ_j on the target molecule, I equally only consider the state with the lowest energy. In case of an electron transfer this means that ΔE corresponds to the difference in electron affinity of the two molecules, in the case of an hole transfer to the difference of ionization potentials.

Fig. 3.2.2 shows the spectrum of an cationic α -NPD molecule as calculated using density functional theory (hybrid B3LYP functional). The first excited states are approximately 0.1eV higher in energy than the ground state. Considering the exponential energy penalty in Eq. 3.2.1, it is clear that for hops upwards in energy, the dominant contribution to the hopping rate ω_{ij} will come from the hop to the final state of lowest energy. Both the

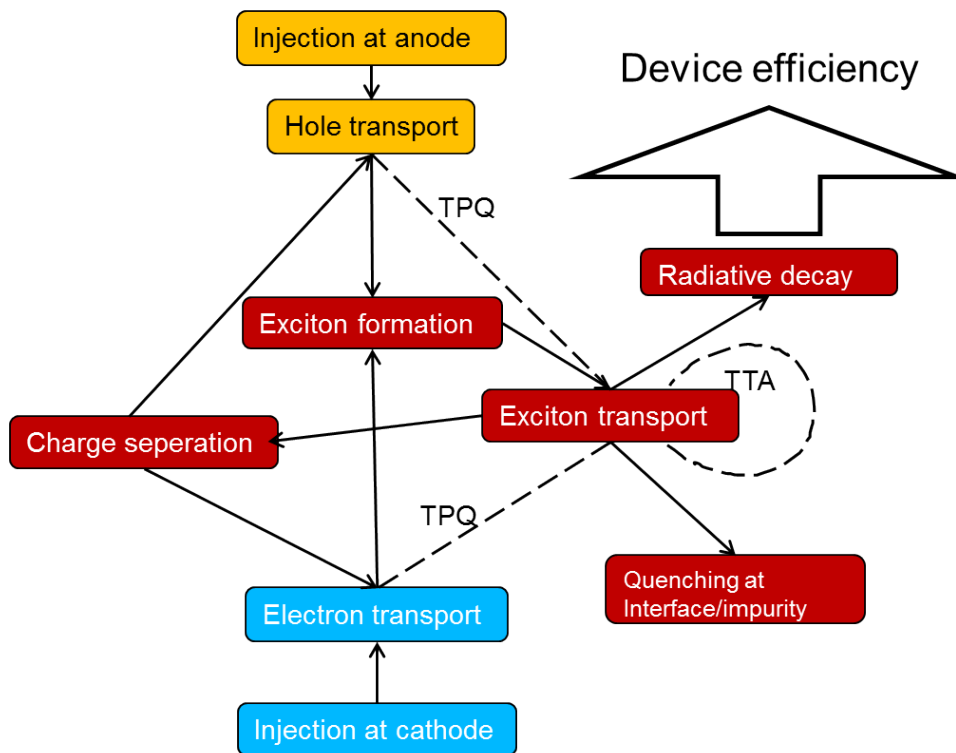


Figure 3.2.1: Overview of the processes included in the device simulation. Localized charges are injected at the anode and cathode. If electrons and holes meet on a single molecule, they form strongly bound excitons. Excitons can decay radiatively, transfer their excitation energy to other charges (triplet-polaron-quenching, TPQ, see Section 3.2.5) or excitons (triplet-triplet-annihilation, TTA, Section 3.2.5), or disassociate in spatially separated electron hole pairs.

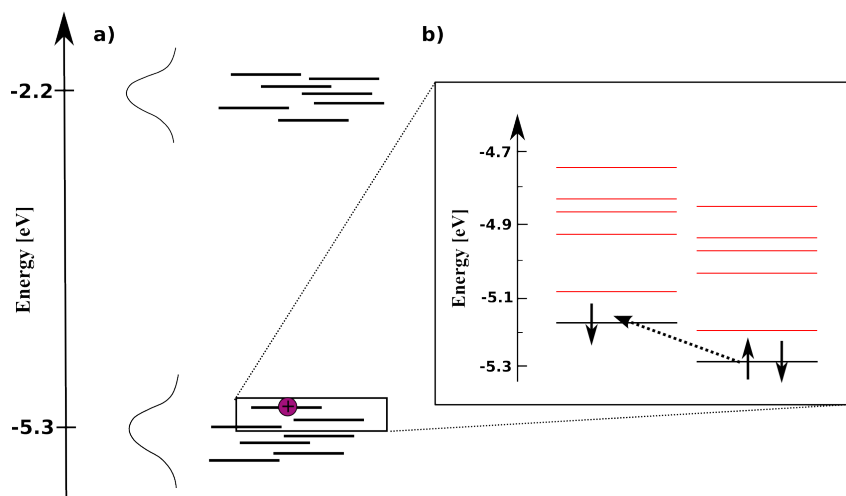


Figure 3.2.2: a) sketch of α -NPD HOMO and LUMO levels. HOMO and LUMO levels on individual molecules vary due to conformational and electrostatic disorder. A hole in a high homo level is symbolized by a pink circle. b) Energy levels of positively charged α -NPD. The energies of occupied orbitals are shown in black, the energy of unoccupied levels are shown in red. For hopping processes upwards in energy, a charge transfer to unoccupied levels is very unlikely in Marcus theory.

packing of the molecules in an amorphous matrix and the inhomogeneous electrostatic environment make a degenerate ground state unlikely. For hops downwards in energy, the assumption that the only relevant contributions to ω_{ij} come from the ground state to ground state transition is inaccurate. In the inverted Marcus regime [54] ($\Delta E_{ij} > -\lambda_{ij}$), a transition to a higher energy state on the target molecule might yield significant contributions to the hopping rate. As typical variance of the energy disorder in a pure amorphous OSC is around 0.1eV [94] and typical reorganization energies are around 0.2eV, downward hops in the inverted Marcus regime can be expected to be rare in a pure material. However, at the interface between two material types or in a material consisting of different molecular species, downward hops to an excited state of the target molecule might be relevant due to the additional offset in electron affinities/ionization potentials of the different molecular species. Nonetheless, an underestimation of the hopping rates of steep downward hops, is not relevant for the overall drift velocity of the charge, as the asymmetry in the Marcus exponent between upward and downward hops $(\lambda_{ij} + \Delta E_{ij})^2 > (\lambda_{ij} - \Delta E_{ij})^2$ means that upward hops will generally be slower and as such predominantly determine drift velocity in the material. An extension of the hopping model, which includes second order transitions through virtual states is given in Chapter 5

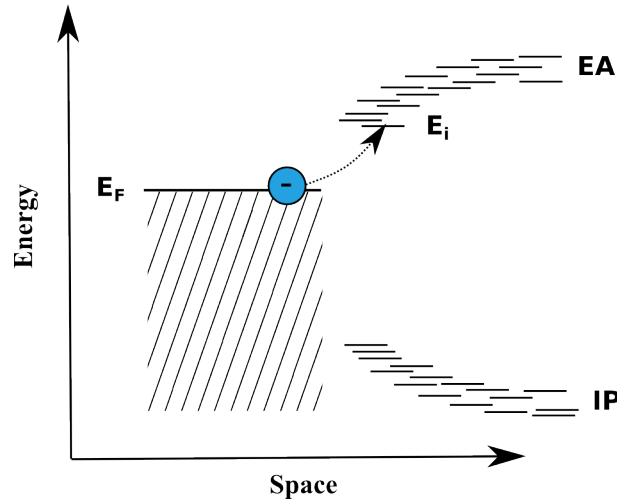


Figure 3.2.3: Schematic molecular ionization potential and electron affinities in proximity of a metallic contact. Electrostatic screening of the metal surface lowers the electronic energy. Due to the energy disorder, electron and hole injection barriers vary from molecule to molecule.

3.2.2 Charge injection and ejection

In the models used in this work, charge injection from the electrode is treated as a charge hopping process from a bath of charges to individual molecules in the OSC. I model injection rates using generalized form of Miller-Abrahams rates (see Section 2.2) [68].

$$\omega_i = \omega_0 |J^2| \begin{cases} \exp(-\Delta E_i / (k_B T)) & : \Delta E_i > 0 \\ 1 & : \text{else} \end{cases} \quad (3.2.2)$$

ΔE_i is an injection barrier, which will be discussed later. For hops downwards in energy, this rate respects that the metal can dissipate continuous amounts of energy.

In this model, the electronic coupling between an exponentially decaying wavefunctions of the molecule and the metal only depends on the distance of the molecular center to a smooth surface. This neglects the spatially inhomogeneous wavefunction on randomly rotated molecules. However, the distribution of charges over the organic molecules at the interface to the electrode at thermal equilibrium only depends on the differences of the electron affinities of the molecules with respect to each other and to the workfunction of the electrode and not on their electronic coupling, as long as rates for ejection and injection fulfill detailed balance.

If we consider Fig. 3.2.3, an increase of electron affinities of the molecules with decreasing distance to the electrode can be seen. This increase in electron affinity is due to the electrostatic boundary conditions at the electrode, which require a constant electrostatic potential Φ at the electrode surface. An electron at distance r to the electrode thus induces electronic screening which can be modeled using image charges. Consequently the potential energy of the electron is lowered by

$$\Phi_{\text{screening}} = \frac{1}{8\pi\epsilon_0\epsilon_r} \frac{-q}{2r} \quad (3.2.3)$$

where $-q$ is the charge of an electron. The factor 8 instead of 4 in the denominator of the coulomb energy originates from the fact that when a charge approaches the electrode

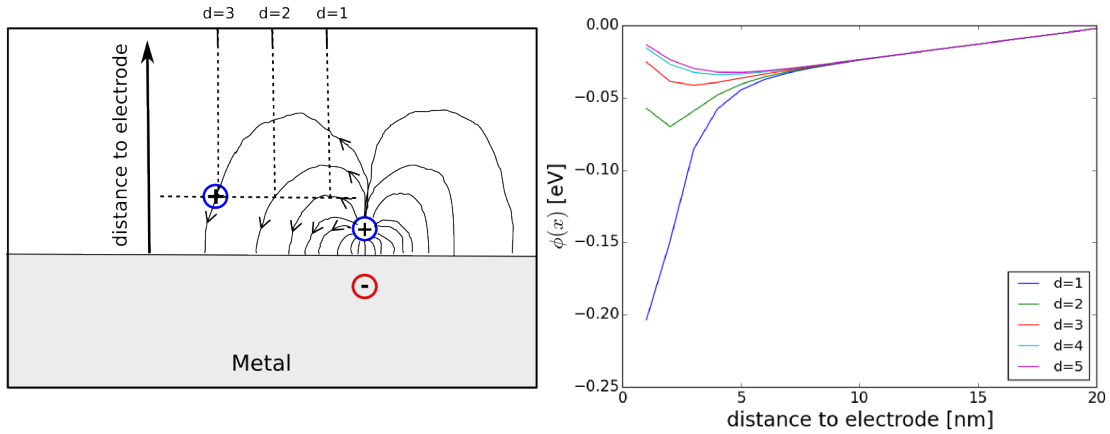


Figure 3.2.4: a) Field lines created by a hole near to an electrode. Holes close to the electrode are pushed towards the electrodes by other holes. b) The coulomb potential created by a hole close to the electrode as a function of the distance to the electrode for lateral displacements of $d = 1\text{nm}$ to 5nm as indicated by dotted lines in a).

from infinite distance, its mirror charge approaches from negative infinite distance so that the integrated coulomb energy when a charge moves from infinity to r is lower by a factor of two.

The lowered Coulomb potential at the electrode leads to an accumulation of charge at the interface. To estimate the energy barrier for diffusion away from the electrode consider a charge hopping process from a site at interface distance r_1 to distance r_2 . An external bias field \vec{F} will change the electrostatic contributions to the energy difference (neglecting other charges and energy disorder for now) such that the barrier for the hopping process will be $\Delta E_{12} = \frac{1}{16\pi\epsilon_0\epsilon_r} \left(\frac{[-q]}{r_2} - \frac{[-q]}{r_1} \right) - q\vec{F} \cdot (\vec{r}_2 - \vec{r}_1)$. Considering r_1 and r_2 close to the electrode ($\mathcal{O}(1\text{nm})$), a hopping distance of $\approx r_2 - r_1 = 1\text{nm}$, and a relative permittivity of $\epsilon_r = 4$, the required field strength to create a negative ΔE_{12} (removing the hopping barrier) is $> 4\text{V}/100\text{nm}$. The barrier to leave the electrode is increased further if there is a finite charge accumulation close to the electrode as the dipole moment created by the charge and the image charge causes an attractive potential close the interface for other charges of the same sign (see Fig. 3.2.4).

Over time, charge will diffuse away from the charge accumulation near the electrode and will be replenished from the electrode. In case the electronic coupling between electrode and molecules is larger than a certain threshold, the replenishment of the surface charge is potentially faster than the diffusion current away from the electrode. In this case, the mean charge concentration in the organic material becomes independent of the metal-organic coupling strength. (Under conditions which would deplete the surface charge, details of the electrode-molecule coupling would of course be more important).

Turning our attention back to Eq. 3.2.2, the injection barrier is given by

$$\Delta E_i = W - E_i = W - E_i^{\text{bulk}} - \frac{1}{16\pi\epsilon_0\epsilon_r(r)} \frac{[-q]}{r} - \Phi_{\text{dyn}} - qF \cdot r_i \quad (3.2.4)$$

where W is the workfunction of the metal, E_i^{bulk} is the electron affinity of the molecules in the bulk phase (see Section 3.3.2), r is the distance of a charge to the electrode, F is

the field perpendicular to the electrode and Φ_{dyn} is the field created by other charges in the system in the given electrostatic boundary conditions (see Section 3.3.2). In contrast to the Marcus rate (Eq. 3.2.1), there is no barrier for hops far down in energy. Physically this corresponds to the ability of the conductors bands to absorb and dissipate continuous amounts of energy, a feature not possible in the discrete energy spectrum of the molecules.

Although the pre-factor ω_0 in Eq. 3.2.2 is usually employed phenomenologically, a rough approximation can be constructed using Fermis Golden rule. Let us consider a transition from the electrode to the molecule upwards in energy. For an injection barrier $\Delta E_i > k_B T$ The electron transfer will then start from a state in the conductor with a occupation probability roughly proportional to $e^{-(E-E_F)/k_B T}$, where E_F is the Fermi energy in the conductor. We further consider the reaction coordinate along the path of geometric relaxation of a charged molecule upon de-charging. The conformational hopping barrier for a hop on the neutral molecule will then be smallest along this reaction coordinate, so that a vibrational excitation along this reaction coordinate is the ‘‘cheapest’’ way to reach a confirmation for the electron transfer. We further assume this vibration as the only relevant contribution for the charge transfer, as the occupational probabilities of transition points along other reaction paths will be suppressed stronger by the Boltzmann factor. Under this assumption, the (relevant) vibronic density of states on the target molecule can be approximated as:

$$D(E) \approx \begin{cases} \frac{1}{\hbar\omega_{\text{ct}}} & \text{if } E - E_i > 0 \\ 0 & \text{else} \end{cases} \quad (3.2.5)$$

with

$$\omega_{\text{ct}} = \vec{\omega} \cdot \vec{x}_{\text{ct}} \quad (3.2.6)$$

where $\vec{\omega}$ is the vector of vibrational eigenmodes of the molecule and \vec{x}_{ct} the unit vector of the reaction coordinate of the charge transfer in the basis of the normal coordinates. The total transition rate ω_{if} is then roughly given as a sum of all transitions with initial states weighted by their occupation probability.

$$\omega_{\text{if}} = \frac{2\pi}{\hbar} J^2 \rho(E) = \frac{2\pi}{\hbar} J^2 \int_{E_i}^{\infty} \frac{e^{-\frac{E-E_i}{k_B T}}}{k_B T} \frac{1}{\hbar\omega_{\text{ct}}} dE = \frac{2\pi}{\hbar} J^2 \frac{1}{\hbar\omega_{\text{ct}}} e^{-\frac{E_f-E_i}{k_B T}} \quad (3.2.7)$$

If we now assume that the reorganization will mostly involve c-c bond stretches with $\hbar\omega_{cc} \approx 4k_B T_{\text{room}}$ we can estimate the transition rate as

$$\omega_{\text{if}} \approx \frac{2\pi}{\hbar 4k_B T_{\text{room}}} J^2 \begin{cases} e^{-\frac{E_f-E_i}{k_B T}} & \text{if } \Delta E_{\text{if}} > 0 \\ 1 & \text{else} \end{cases} \quad (3.2.8)$$

where the Boltzmann factor can be dropped in the second line, as the target state is lower then the Fermi level of the conductor, such that a resonant state can always be found. I would like to remark that this prefactor is roughly two times the prefactor of the Marcus rate (Eq. 3.2.1) for typical reorganization energies of 0.2eV. Although my estimation was very crude, this ratio seems very reasonable as a Marcus like charge transfer involves the reorganization of two instead of one molecules. An estimation of the metal organic transfer integrals J is given in Chapter 6.

3.2.3 Charge recombination and separation

Separation of a localized exciton in an electron hole pair, where the electron is localized on molecule A and the hole on molecule B is schematically depicted in Fig. 3.2.5 a). The separation of the exciton takes place as a charge transfer process of either electron or hole to the neighboring molecule. As the binding energy of the exciton has to be paid, a separation of the strongly bound exciton is only likely if there is large enough difference in ionization potential or electron affinities on the two molecules that localization of the charge carriers on two molecules is favored. This might be the case at the interface between two different molecules and be enhanced/weakened by the local electrostatic potential and the intrinsic disorder of electron affinity and ionization potential.

From Fig. 3.2.5 it is clear that there are two distinct final charge separated states. One state where the electron is on molecule B (right) and the hole on molecule A (left), the other state vice versa. Due to the asymmetry of the situation illustrated in Fig. 3.2.5, it is apparent that the rates for both processes will be vastly different. The system might gain energy through an electron transfer to molecule B, but would have to pay for an hole transfer to molecule B. I estimate the rates for these charge transfers as before using the Marcus rate equation 3.2.1.

Transfer integrals $J_{ij} = \langle \psi_i | H | \psi_j \rangle$ are assumed to be identical to the corresponding charge transfer integrals (Section 3.3.3), reorganization energies are calculated as described in λ (Section 3.3.4). The energy difference for an electron transfer from molecule A to molecule B is given by

$$\Delta E^{\text{sep}} = \Delta E_A^{\text{sep}} + \Delta E_B^{\text{sep}} + \Delta E_{\text{Coulomb}} = |IP_A| - |EA_B| - |E_A^*| - \frac{1}{4\pi\epsilon_r\epsilon_0} \frac{1}{r_{AB}} \quad (3.2.9)$$

where IP_A is the ionization potential of molecule A, EA_B the electron affinity of molecule B and E_A^* the excitation energy of the exciton on molecule A. The electron affinity is here understood as the energy gained by adding another electron from vacuum to the neutral molecule, the ionization potential as the energy that has to be paid to remove an electron from a neutral molecule. Eq. 3.2.9 then follows from comparing initial and final state total energies of the system. In Eq. 3.2.9 this is done by separating the energy difference into the difference of total electronic energy of molecule A ΔE_A , the difference of total electronic energy of molecule B ΔE_B and the classic coulomb interaction of the separated electron hole pair (see the illustration in Fig. 3.2.5 b)). This separation is valid as long as excited and ground states are localized on the individual molecules.

The energy difference for a hole transfer from molecule A to molecule B is equivalently given by:

$$\Delta E_{\text{sep}} = \Delta E_A + \Delta E_B + \Delta E_{\text{Coulomb}} = |IP_B| - |EA_A| - |E_A^*| - \frac{1}{4\pi\epsilon_r\epsilon_0} \frac{1}{r_{AB}} \quad (3.2.10)$$

These expressions give the energy differences for a charge separation into the lowest states on the individual molecules. Rates for charge transfer processes into higher energy states can be obtained if initial and final state energies are modified accordingly. In Eq. 3.2.9 $|EA_B|$ has to be replaced by $|EA_B| - E_-^*$, where E_-^* is the energy difference of the anionic ground state and the excited anionic state the electron hops to on molecule B. In case of

an hole transfer in an excited cationic state on molecule B, $|IP_B|$ in Eq. 3.2.10 has to be replaced by $|IP_B| - E_+^*$.

Charge recombination to form an exciton is treated as the reverse process of charge separation and equally quantified using Marcus rates. The energy difference for charge recombination into an excited state E_A^* is simply given by:

$$\Delta E^{\text{sep}} = -\Delta E^{\text{sep}} \quad (3.2.11)$$

Depending on ionization potential and electron affinities of the involved molecules there may be many excited states into which recombination is energetically favorable. In an OLED light emitting layer, where recombination tends to take place by a charge transfer from a transport molecule to an oppositely charged emitter molecule, this would be the case.

If we consider charge recombination in systems that may contain states which lie in the HOMO LUMO gap (this could be the case at a strongly disordered interface of two different organic materials or in a system containing impurities), as illustrated in Fig. 3.2.5c) for the first case, two modes of direct (thermal) recombination of electrons and holes also have to be considered. In the first case, thermally assisted Marcus-like charge transfer from a low lying electron state on molecule B into a high lying hole state on molecule A would annihilate electron and hole directly. I quantify this again using Marcus rates. The energy difference of the electron transfer from anionic molecule A to cationic molecule B, which leads to direct recombination is given by

$$\Delta E^{\text{recom}} = |EA_A| - |IP_B| + \frac{1}{4\pi\epsilon_r\epsilon_0} \frac{1}{r_{AB}} \quad (3.2.12)$$

where the ionization potential of the former cation accounts for the energy which is set free when the electron hops to molecule A while the electron affinity of the former anionic molecule B and the classic coulomb energy of the formerly separated pair has to be paid for. If the gap between $|EA_A|$ and $|IP_B|$ is big enough, the Marcus rate enters the inverted regime, *i.e.* suppresses direct recombination. Would this not be the case, OLED would not emit light. Considering Eq. 3.2.12, it is interesting to note that molecules with small polarizability and thus low relative permittivity will have a bigger contribution from the classical term and begin to recombine directly at larger $|EA_A| - |IP_B|$ gaps. The second case of direct recombination occurs, if a molecule has excitation energies small enough that its excitations can couple to vibrations.

3.2.4 Exciton transfer

Excited state energy transfer is accounted for as Dexter and Förster type transfer as described in Chapter 2, (see Fig. 3.2.6). Dexter transfer describes a simultaneous charge transfer of an excited electron from molecule A to an excited state on molecule B and an electron from molecule B to the non-excited state on molecule A, see Fig. 3.2.6. As all charge transfers I describe this using Marcus rates as shown in Eq. 3.2.1, where the electronic coupling is the coupling between the overlap densities of single electron excited

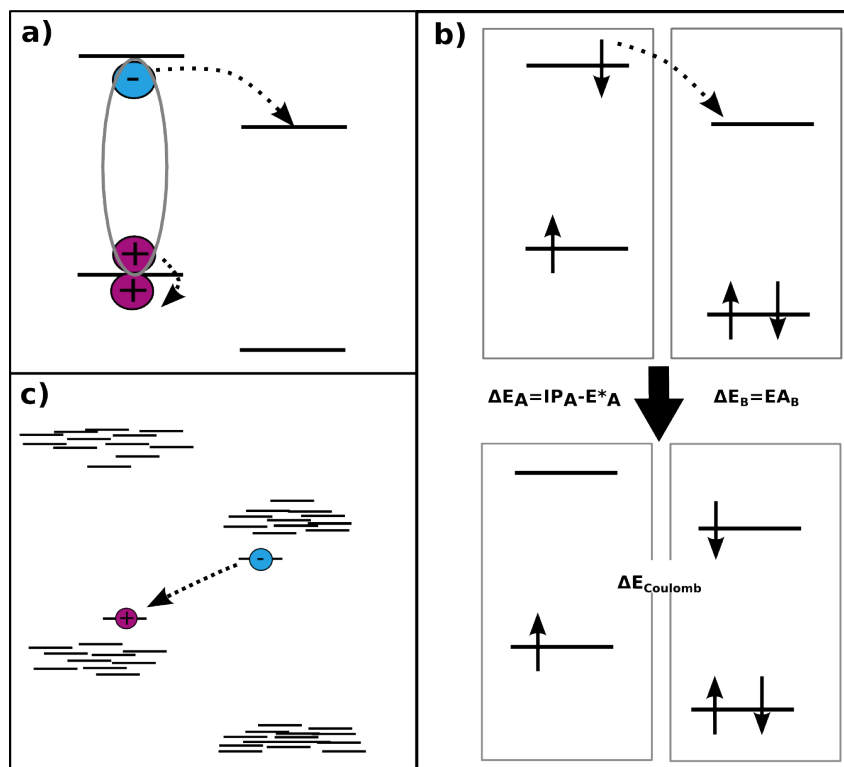


Figure 3.2.5: a) Illustration of the charge separation of an strongly bound exciton in an electron hole pair, where electron and hole are finally localized on different molecules. Black lines represent HOMO and LUMO levels of two molecules with equal HOMO-LUMO gap but with an energy offset between the electronic levels. Charge separation takes place through a charge transfer of the electron to the molecule with the lower lying LUMO. The binding energy of the exciton is accounted for by a general offset in the energy levels of the two molecules. b) Schematic occupation of single electron states on molecule A (left) and B (right) before (top) and after (bottom) charge separation. The energy difference of final and initial state can be calculated by comparing final and initial state of the individual molecules. The complete removal of an electron from the molecular ground state of molecule A costs the ionization potential. As the system is however in an excited state, part of the ionization is already paid for. On molecule B, the energy gained by the charge separation is simply given by the electron affinity. The energy of the final state is lowered by the Coulomb interaction of the now separated charge monopoles. c) Distribution of HOMO and LUMO levels on an interface of molecules of type A and B. A hole in a very high lying state on a molecule of type A and an electron in a low lying state on a molecule of type B can have an increased rate for direct charge recombination, as the energy gap gets closer to energies of molecular vibrations.

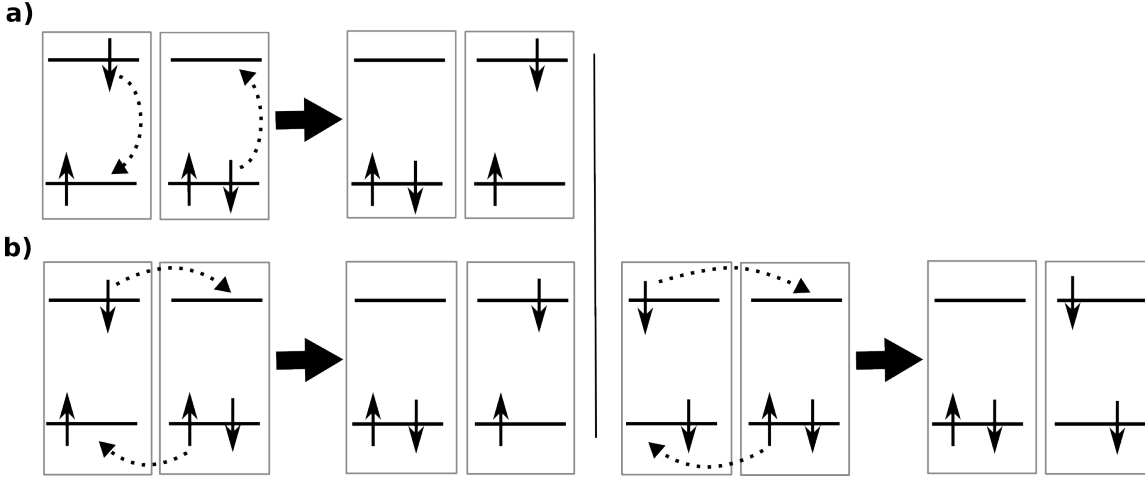


Figure 3.2.6: a) Förster excitation energy transfer of a spin-singlet as a correlated deexcitation/excitation on both molecules. Due to the Pauli principle, this is not possible for triplets without a spin flip. b) Dexter excitation energy transfer. A simultaneous charge transfer of electron and hole from the right to the left shown on the left for a singlet and on the right for a triplet

states on A and B (which can be approximated as the LUMO LUMO overlap) and the single electron ground states on A and B (HOMO HOMO overlap), see Chapter 2.

$$\langle \Psi_A^* \Psi_B^0 | H | \Psi_A^0 \Psi_B^* \rangle \approx \int \int d\vec{r}_1 d\vec{r}_2 \psi_{\text{LUMO}}^A(\vec{r}_1) \psi_{\text{LUMO}}^B(\vec{r}_1) \frac{1}{|r_1 - r_2|} \psi_{\text{HOMO}}^A(\vec{r}_2) \psi_{\text{HOMO}}^B(\vec{r}_2) \quad (3.2.13)$$

Förster transfer describes an energy transfer as an de-excitation on molecule A correlated with an excitation on Molecule B. For negligible overlap of the transition densities on molecule A and molecule B, the interaction is to first order mediated by the dipole interaction of the transition densities. The electronic coupling is given in Chapter 2:

$$\langle \Psi_A^* \Psi_B^0 | H | \Psi_A^0 \Psi_B^* \rangle \approx \kappa \frac{|d_A^{\vec{r}}| |d_B^{\vec{r}}|}{|r_{AB}|^3} =: V^{\text{dd}} \quad (3.2.14)$$

The excitation energy transfer rate is then

$$\omega_{\text{EET}} = \frac{2\pi}{\hbar} |V^{\text{dd}}|^2 J \quad (3.2.15)$$

where J is the spectral overlap of emission on A and absorption on B. In this work, I approximate Eq. 3.2.15 in two different ways. In the first approach, the spectral overlap is approximated using Marcus-rates [57].

$$\omega_{\text{EET}} = \frac{2\pi}{\hbar} |J_{\text{dd}}|^2 \frac{1}{\sqrt{4\pi\lambda_{\text{EET}}k_{\text{B}}T}} \exp\left(-\frac{(\lambda_{\text{EET}} + \Delta E_{\text{EET}})^2}{4\lambda_{\text{EET}}k_{\text{B}}T}\right) \quad (3.2.16)$$

where λ_{EET} is the reorganization energy of the energy transfer and ΔE_{EET} is the energy difference between the ionically relaxed excited state on molecule A and the excited state energy of molecule B in its neutral conformation.

Averaging Eq. 3.2.15 over many pairs one can obtain the phenomenological expression

$$\omega_{\text{EET}} = \frac{1}{\tau_{\text{A}}} \left(\frac{r_0}{r_{\text{AB}}} \right)^6 \quad (3.2.17)$$

where r_0 is called Förster radius, τ_{A} the fluorescence lifetime of molecule A. The sixth power can be directly read of from Eq. 3.2.15 and 3.2.14. The inverse of the fluorescence lifetime is proportional to the square of the transition dipole.

The latter rate expression 3.2.17 for the Förster energy transfer is used in the kinetic Monte-Carlo simulations, if energy transfer-rates are given as experimental input. This expression neglects dependence of the transfer rates on the molecular orientation and the disorder in both excitation energies and transition dipoles. The rate expression 3.2.16 based on Marcus theory accounts for this microscopic information but uses a crude approximation on the spectral overlap. More sophisticated rates explicitly account for the vibronic coupling [57], but obtaining the necessary microscopic parameters is cumbersome.

As Dexter transfer requires wavefunction overlap, it will only yield appreciable rates on short distance, but as it is a direct transfer of electrons, it is possible for both singlet and triplet excitons. The polynomial distance dependence of the Förster rate allows for long range transfer. However, the electron spin on the individual molecules has to be preserved, such that an energy transfer of a triplet would require a spin-flip on both molecules. This can not be induced by the dipole - dipole coupling of the transition densities but would require intersystem crossing through *e.g.* spin-orbit coupling. This means that singlet excitons will generally have higher energy transfer rates than triplets.

3.2.5 Exciton decay and quenching

A principal goal of OLED simulations is to understand processes which limit the energy to light conversion efficiency. A fraction of the input energy is dissipated as heat during the charge transport process due to the resistance of the organic semiconductors. With increasing operating voltage, the fraction of non-radiatively decaying excitons increases [28, 66]. The radiative decay rate of an exciton is given by $\omega_{S_0} = \frac{1}{\tau_{S_0}^{\text{A}}}$ for a singlet in the first excited state on molecule A, and by $\omega_{T_0} = \frac{1}{\tau_{T_0}^{\text{A}}}$ for a triplet in the first excited state on molecule a. I only consider the lowest lying excited states as radiative, as I assume all higher excitation to rapidly relax into S_0/T_0 states. For a typical emitter molecule like Ir(ppy)₃, fluorescence lifetime is in the order of hundred picoseconds and while triplet lifetime is in the order of milliseconds. Radiative triplet decay is possible in the case of Ir(ppy)₃ due to the high spin-orbit coupling of iridium. A direct thermal decay of an optically excited electron is highly unlikely due to the very weak coupling between electronic states separated by $> 2\text{eV}$ by molecular vibrations ($\hbar\omega < 0.1\text{eV}$). Thermal decay will mainly take place through inter band gap states or at interfaces as accounted for in Section 3.2.3.

Under low operating voltage, well designed OLEDs show power to light conversion

efficiencies of nearly 100 %. At higher voltages however, the efficiency of the OLED drops, suggesting an exciton quenching mechanism which depends on the concentration of free charges and excitons in the system *i.e.* interaction between charges and excitons. In this work, I am mainly interested in the effect of exciton - exciton/charge interactions. As they lead to non radiative decay of the excitons, I only account for charge - exciton interactions (up to second order) which could either induce a thermal decay of the exciton or involve an energy transfer from the exciton to another exciton/charge. First order charge-exciton interactions (*e.g.* singlet-triplet conversion) which do not lead to dissipation of the excitation energy are not accounted for in this work.

In the following, I will discuss energy transfers from excitons to other quasi particles. At the end of the section, I will discuss the possibility of thermal decay induced by the perturbation of the excited states through free charges.

Second order energy transfer interactions leading to exciton quenching are shown in Fig. 3.2.7 for electron-triplet interactions, in Fig. 3.2.8 for triplet-triplet interactions and in Fig. 3.2.9 for triplet-singlet and singlet-singlet interactions. I refer to triplet energy transfer to a charge as triplet-polaron quenching (TPQ), energy transfer from a singlet to a charge as singlet polaron quenching (SPQ), energy transfer from a triplet to another triplet as triplet-triplet annihilation (TTA), energy transfer from a triplet to a singlet or vice versa as singlet triplet annihilation (STA) and energy transfer from singlet to singlet as singlet singlet annihilation (SSA).

Due to the small overlap of the states localized on the different molecules, the inter-molecular exchange interaction is far weaker than intra-molecular exchange. Thus, the spin quantization axes on the molecules may differ, such that an electron with “spin up” on molecule A may have both “spin-up” and “spin-down” contributions on molecule B. In the illustrations 3.2.7-3.2.9, possible transitions are considered as made up from all relative spin directions of A and B, which are linear independent.

Charge-exciton quenching

On phosphorescent emitter molecules, contributions from the singlet-electron interactions, as shown in Fig. 3.2.8, also have to be considered for the triplets, due to the strong spin-orbit coupling on the molecule. The only allowed second order triplet-electron interaction which quenches the exciton (and does not involve a spin flip), involves a charge transfer of the extra electron on molecule A to molecule B correlated with an higher excitation of molecule B, which can thermally cascade into its charged ground state. This effectively corresponds to an annihilation of the triplet on molecule B, and a charge transfer of the extra electron on molecule A to molecule B. The same decay channel is available for the singlet (red and cyan in Fig. 3.2.8). Additional final states for a singlet-electron energy transfer, can be reached through a Förster transfer, which excites the extra electron (blue and pink) or through a mixed Förster/Dexter transfer (green).

Although all singlet decay channels are also available for triplets by spin orbit coupling, for a given initial state I assume dexter transitions not involving intersystem crossing as dominant over dexter singlet decay channels, which would involve intersystem crossing to the triplet. For a triplet on a molecule directly neighboring an electron, I would thus

consider the triplet contribution from Fig. 3.2.8a) and dismiss the cyan, red and green channels from b). Long-range (no wavefunction overlap) energy transfer is only possible as a Förster process involving intersystem crossing, which excites the extra electron and deexcites the exciton (blue and pink in Fig. 3.2.8b)). Among the blue and pink processes, I assume the blue one to occur with a significantly higher rate, as in the Marcus picture both processes have a hopping barrier due to the change in ionic confirmation needed for the excitation. In the blue process, this hopping barrier is lowered by jumping into a lower excited state in the dense spectrum above the HOMO-LUMP gap. For the pink process, there is no such lower state available. Thus, the final states I consider in total, are either an excitation (Fig. 3.2.8b)) of the extra electron, or a charge transfer on the triplet (blue in Fig. 3.2.8a)).

Energy transfer rates for these processes can be calculated with the formalism described above (see Section 3.2.4) if excitation energies, transition dipoles and the direct transfer integrals of the charged and excited molecules can be calculated. In practice, this goes beyond the limits of computationally feasible quantum chemistry methods, such that I approximate the energy- and charge-transfer rates to an already excited or charged molecule by the energy transfer rates to the same neutral molecule. Effectively this means the following:

- If a charge hops on the site of an exciton (in this approximation with a rate independent of the excitation of the molecule) it is assumed to quickly (thermally) cascade into its ground state. The exciton is destroyed.
- If an exciton hops on the site occupied by a charge carrier (with a rate independent of the charge state of the molecule), the exciton is destroyed and the charge assumed to quickly (thermally) cascade into its ground state.

These interactions qualitatively lead to an increase in exciton quenching with higher charge concentration simply because more molecules to which an energy transfer takes place are either charged or excited.

Exciton-exciton quenching

Fig. 3.2.8 shows possible triplet-triplet interactions leading to the annihilation of an exciton. Final states of the interactions are either a separated electron-hole pair (blue and red boxes in Fig. 3.2.8) or a highly excited exciton (green and pink box). Although visualized as a singlet exciton, the highly excited exciton might be both a singlet or triplet, as it is formed in a process involving a charge transfer between the molecules, which may have different spin quantization axes. This green/pink transfer is a Dexter charge transfer, while the charge separation processes (red and blue) involve both an intermolecular charge transfer and an intramolecular excitation.

The singlet-triplet and singlet-singlet interactions (see Fig. 3.2.9) have additional interaction paths, as the singlets can deexcite on their molecules, but end up in the same final states - either separated charges or highly excited excitons. At this point it is not feasible to calculate the exact rates for these processes and I treat them according to some interaction rules.

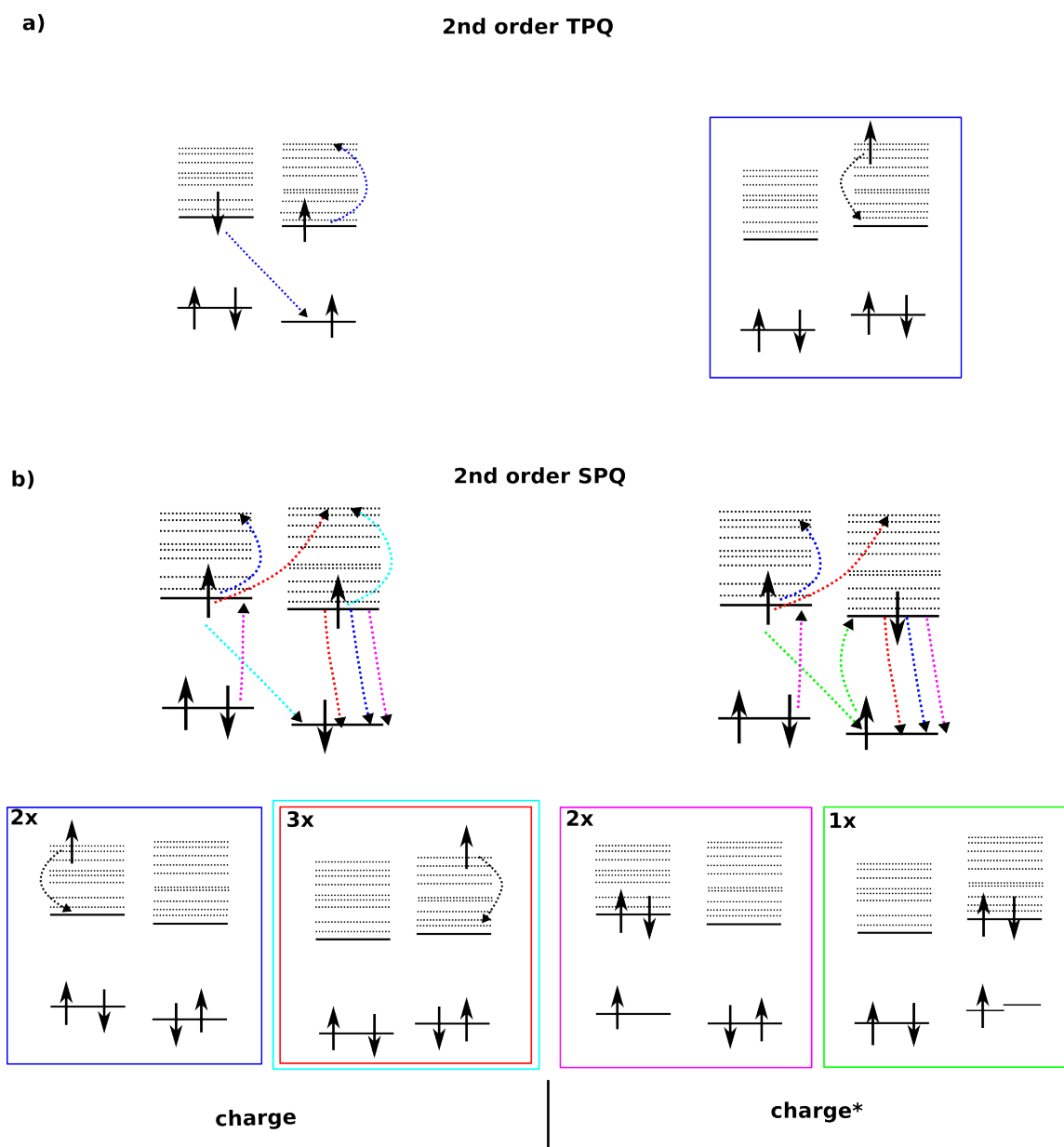


Figure 3.2.7: Second order electron-exciton interactions, which lead to radiation free exciton quenching. Pairs of dashed arrows of the same color show allowed transition path not involving spin flips. The final configurations of the transitions are shown in boxes of the respective color. Full black lines symbolize HOMO and LUMO levels, dashed black lines higher unoccupied levels. Black dashed arrows down to the LUMO level symbolize thermal deexcitation. a) Triplet to electron energy transfer as correlated charge transfer and excitation. This requires wavefunction overlap of the left LUMO and the right HOMO. b) Singlet to electron energy transfers. On molecules with strong spin-orbit coupling, these transitions are also possible for triplets.

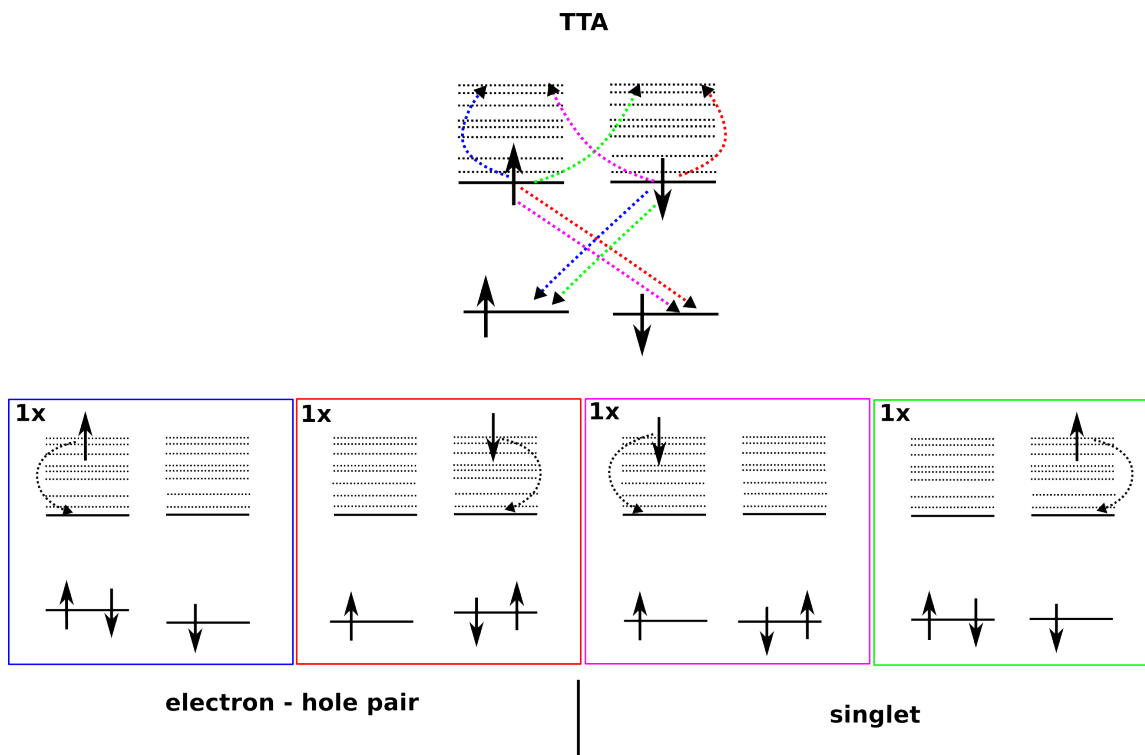


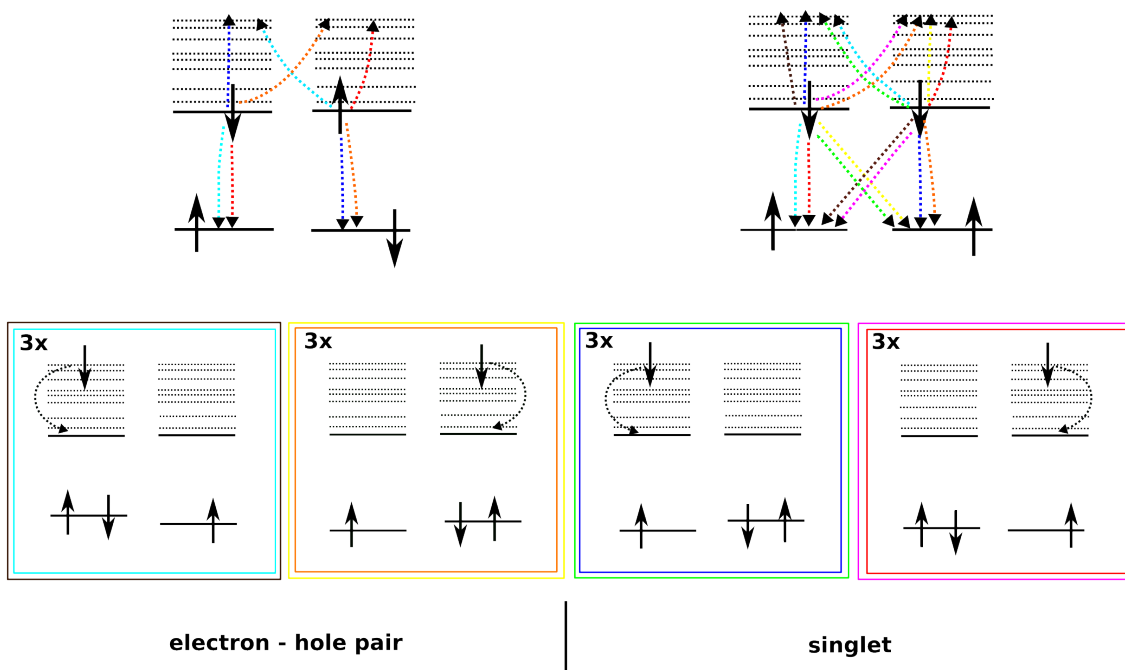
Figure 3.2.8: Second order triplet-triplet interactions, which lead to radiation free exciton quenching. Pairs of dashed arrows of the same color show allowed transition path not involving spin flips. The final configurations of the transitions are shown in boxes of the respective color. Full black lines symbolize HOMO and LUMO levels, dashed black lines higher unoccupied levels. Black dashed arrows down to the LUMO level symbolize thermal deexcitation. The final state of the interactions are either a separated electron - hole pair (blue, red) or an highly excited exciton (pink, green). All shown interactions require wavefunction overlap between the molecules. On molecules with strong spin-orbit coupling, interactions shown in Fig. 3.2.9 are also possible for triplets.

- If an exciton hops on the site of another exciton (in this approximation with a rate ignorant of the excitation of the molecule) the hopping exciton is destroyed. In 50% of cases, the second exciton is also destroyed and a separated electron hole pair is created. In the other 50% of cases, the exciton on the target site survives. In both cases, either the highly excited left-over exciton or in case of the electron hole pair the excited electron are assumed to quickly (thermally) cascade into the lowest excited state or lowest charged state respectively.

I will now estimate the possibility of thermal decay induced by an perturbation of the excited states through the electric field of free charges, which can lower excitation energies, and thus increases the likelihood for an energy dissipation by molecular vibrations. In typical phosphorescent emitter-molecules like $\text{Ir}(\text{ppy})_3$, the T_0 -excitation involves a local charge transfer from the iridium atom in the center to one of the organic ligands on the same molecule, such that a thermal decay of the excitation can be facilitated by a strong gradient of the electrostatic potential. An interaction of charge monopoles with

a)

2nd order SSA



b)

2nd order STA

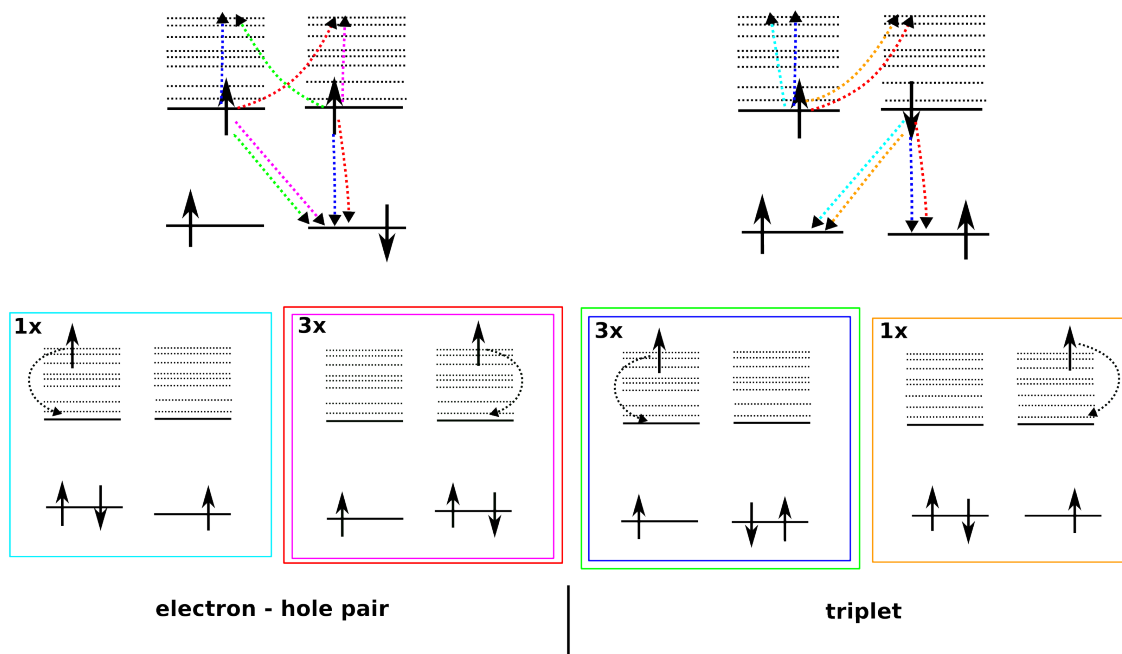


Figure 3.2.9: Second order exciton-exciton interactions, which lead to radiation free exciton quenching. Pairs of dashed arrows of the same color show allowed transition path not involving spin flips. The final configurations of the transitions are shown in boxes of the respective color. Full black lines symbolize HOMO and LUMO levels, dashed black lines higher unoccupied levels. Black dashed arrows down to the LUMO level symbolize thermal deexcitation. The final state of the interactions are either a separated electron - hole pair (blue, red) or an highly excited exciton (pink, green). a) shows singlet-singlet reaction path, b) singlet triplet reaction path. All shown interactions require wavefunction overlap between the molecules. On molecules with strong spin-orbit coupling, all SSA interactions are also possible for triplets.

the strong dipole of the exciton could lower the excitation energy, such that a thermal dissipation of energy becomes more likely. If we consider a T_0 energy $> 2\text{eV}$, it is however very unlikely to create a field strong enough to induce a thermal decay of the exciton. To lower excitation energies to the order of molecular vibrations ($< 0.1\text{eV}$), the electric potential would need to drop by 2eV on the length scale of the molecule. If we consider a positive monopole on a molecule next to a molecule with a charge transfer excitation, such that the distance of the monopole to the positive pole of the dipole at the iridium center is 1nm and the distance to the negative pole on the organic ligand is 0.5nm , the potential created by the monopole would drop by $\frac{q^2}{4\pi\epsilon\epsilon_r}(\frac{1}{0.5\text{nm}} - \frac{1}{1\text{nm}}) = 0.36\text{eV}$ over the length of the dipole, to first order lowering the energy of this excited state by the same amount. Single charges should thus not be sufficient to perturb the excitation enough to induce thermal decay. A concentration of charges that would create strong enough local fields seems also unlikely as the electric fields enter the exponent of the charge transfer rates (see Eq. 3.2.1) and thus act against the build up of the required local charge densities. This leaves an energy transfer to charges or other excitons as the most plausible way for concentration dependent non-radiative exciton energy dissipation.

3.3 Microscopic parameters

In the following I will discuss how to create a model of the organic material and to how to obtain the parameters needed to calculate the transition rates introduced in section 3.2. To correctly account for percolation effects of the charge transport in disordered OSCs, investigated morphology samples have to be of the order of $100 \times 100 \times 100 \text{ nm}^3$ corresponding to $O(10^6)$ molecules. (see 2).

It is computationally unfeasible both to calculate the growth of an atomistic morphology of this size and to calculate the electronic structure of this mesoscale morphology. To generate morphologies and electronic structure parameters needed to construct the hopping rates for the kMC calculations I randomly generate both morphology and electronic structure parameters following parameter distributions of atomistic/electronic calculations.

This approach can be motivated by considering the drift-diffusion of an electron between a sufficiently separated start and endpoint in an amorphous OSC in the direction of an applied bias. The electron mobility μ in this material is given by

$$\mu = \frac{v}{E} = \frac{x}{t \cdot E} \quad (3.3.1)$$

where x is the distance separating the start and endpoint and E the applied electric field. The transit time is given by the sum of the inverse hopping rates along the path of the electron.

$$t_{transit} = \frac{1}{\omega_1} + \frac{1}{\omega_2} + \dots \quad (3.3.2)$$

In case of an isotropic and disordered material, any material model, with the same distribution of hopping rates and site distances exhibits the same electron drift velocity. It is thus not necessary to create a mesoscopic morphology which is indistinguishable from a atomistic morphology but sufficient if hopping rates calculated on a model morphology follow the distribution of rates of the atomistic system.

Marcus hopping rates depend on three microscopic parameters: the energy difference between final and initial state ΔE_{ij} , reorganization energy of the charge transfer λ_{ij} and electronic coupling between final and initial state J_{if} .

$$\omega_{ij} = \frac{2\pi}{\hbar} |J_{ij}|^2 \frac{1}{\sqrt{4\pi\lambda_{ij}k_B T}} \exp\left(-\frac{(\lambda_{ij} + \Delta E_{ij})^2}{4\lambda_{ij}k_B T}\right). \quad (3.3.3)$$

To generate a faithful distribution of hopping rates, it is thus sufficient to reproduce the, if necessary correlated, distributions of ΔE_{ij} , λ_{ij} and J_{if} .

In section 3.3.1 I give an account how to construct topologies of $O(10^6)$ molecules, based on small $O(10^3)$ atomistic morphologies.

In section 3.3.2 I present how time dependent electron affinities and ionization potentials of the OSCs are calculated.

In section 3.3.3 I will present a method to construct transfer-integrals for charge transfer on the generated morphologies.

In section 3.3.4 I will discuss how to obtain reorganization energies of the charge transfer.

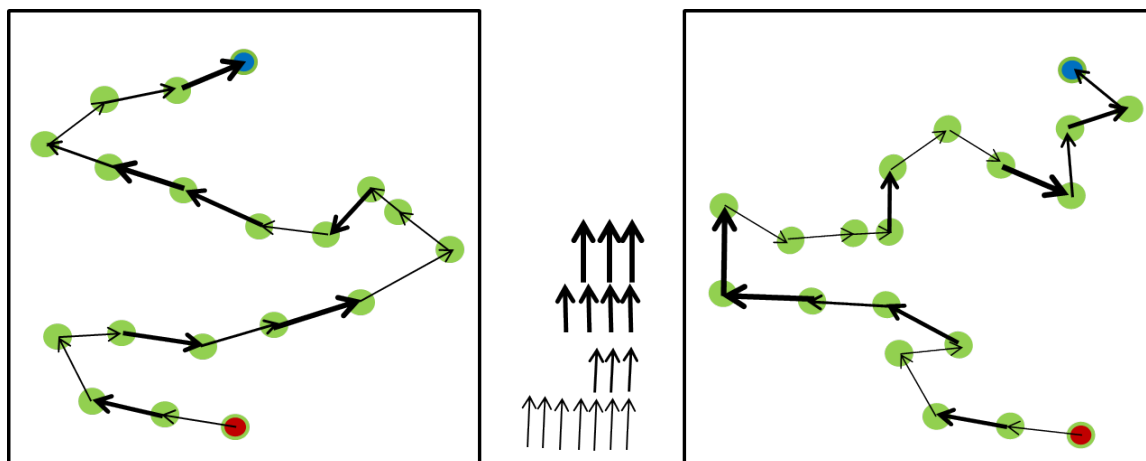


Figure 3.3.1: Two symbolic hopping path between a red and blue point separated by a fixed distance. The thickness of black arrows is proportional to the hopping rate of the respective hop. The equal distribution of hopping rates along both path is shown in the middle. The transit time from red to blue is independent from the hopping path, as long as the distribution of rates individual hopping rates along both path is identical.

3.3.1 Creation of amorphous morphologies

The creation of the morphology can be divided in two steps. In the first step an atomistic morphology is created by means of a Monte-Carlo protocol, which simulates vapor deposition of molecules [95]. Before the start of the deposition simulation an all-atom position dependent energy function (forcefield) is parametrized. This forcefield describes inter-molecular interactions by an atomistic Lennard-Jones and electrostatic potential, intra-molecular interaction by a conformation dependent energy function parametrized with DFT. The electrostatic potential is sourced by point charges on the position of all atoms. The point charges are taken as constant and for a single molecule fit to reproduce the electrostatic potential of this molecule in vacuum. Starting of with an empty simulation box, molecule after molecule is then added to the simulation box and equilibrated using a Metropolis Monte-Carlo algorithm.

Based on this microscopic morphology, a mesoscopic morphology is generated in a two step procedure. In the first step a mesoscopic distribution of points with equal density and which exhibits the same nearest neighbor distance distribution as the center of mass distances of the atomistic morphology, is generated. This is done using a modification of the dominance competition model of Baumeier et al. [73]. The original approach fits a gamma distribution to the nearest neighbor distance distribution. Points are randomly distributed in a periodic simulation box of given dimensions. To each point a radius drawn from the gamma distribution is assigned. If a point falls into the radius of another site, it is removed. If the radius of a new point encloses an already placed point, it is also removed. This procedure is repeated until the target density of points is reached. Here, I modify the radius assignment during the morphology creation by scaling the radii by a factor s , such that the mean square error between the nearest neighbor distance distribution of the resulting morphology and the atomistic target distribution is minimized. The resulting nearest neighbor distance distribution is illustrated for an

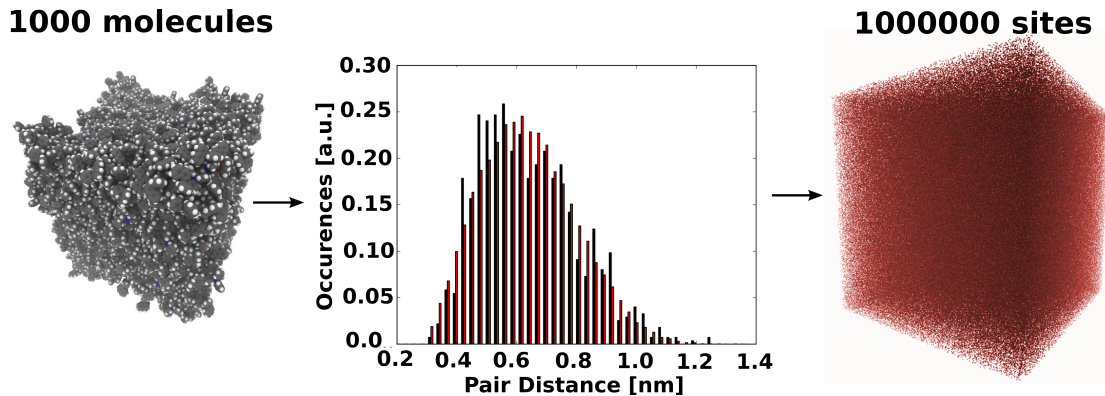


Figure 3.3.2: Stochastic expansion of the distribution of molecular centers of mass. Left: the van-der-Waals surface of an α -NPD morphology of 1000 molecules with generated by simulated vapor deposition. Middle: the nearest neighbor distance distribution for the deposited α -NPD morphology (black) and for a stochastically expanded distribution of 1,000,000 sites (red). Right: the expanded point distribution. (image source: SI in[36])

α -NPD sample in fig. 3.3.2 in red (stochastic) and black (atomistic). If a morphology contains different types of molecules, points have to be labeled by their molecule type. During growth, each point then draws not one but several radii, to reflect a different nearest neighbor distance distribution depending on the molecule types of the pair. The selection criterion described above can then be applied pair specific.

If the molecular sizes and shapes are similar, using just one nearest neighbor distance distribution will yield similar distributions than several pair specific distributions. A molecular type is then assigned by randomly drawing $x\%$ of the sites, corresponding to the fraction of molecules in the atomistic sample. In both cases the point distribution does not account for agglomeration and phase separation.

For morphologies of anisotropic molecules, the described algorithm, will by design reproduce nearest neighbor distance distributions and molecular densities, but fail to reproduce individual peaks of the radial distribution function. In 3.3.3 I will argue, why these crude approximations will only marginally affect charge transport.

Given the distribution of points, connections between the points have to be established. In the microscopic morphology I consider two molecules to be connected (direct hopping is possible) if the two nearest atoms of the molecules are closer than 0.7 nm (twice the typical Π -stacking distance), so that transfer integrals between molecules where an aromatic group of another molecule has squeezed in are not considered. For molecules with nearest atom distances close to 0.7 nm the transfer integrals are already insignificantly small, so that the final results are insensitive to the precise value of the cutoff distance. Comparing the center of mass distance with the nearest atom distance for each connected pair in the atomistic morphology, I obtain the center of mass distance dependent probability for two molecules to be connected. An example of this function is shown for the two hole conductors α -NPD and TCTA in 3.3.3. Using this probability function, connected pairs of the mesoscopic point morphology can be determined.

If periodic boundary in all or some dimension are needed, sites from opposing ends of the

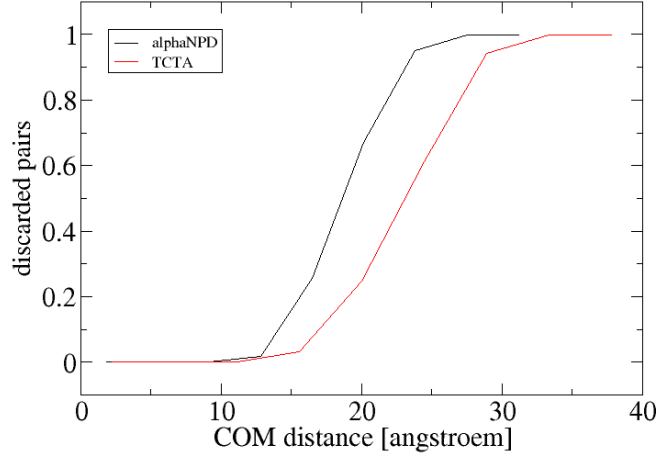


Figure 3.3.3: Probability of a pair of molecules to be not connected depending on their center of mass distance.

morphology are connected if a periodic copy of one site and the other site are connected.

3.3.2 Onsite energies

Charge transport rates in energetically disordered OSC, are mostly determined by the onsite energy difference of charge carriers between molecules[58]. Electron affinity (EA) differences for a hop from site i to site j are given by:

$$\Delta EA_{ij} = [EA_j^0 + |q|\Phi_j^{dyn}] - [EA_i^0 + |q|\Phi_i^{dyn}] + |q|\vec{F} \cdot \vec{r}_{ij} \quad (3.3.4)$$

where EA_x^0 is the electron affinity of molecule x at zero charge concentration, q the electron charge, Φ_x^{dyn} the electrostatic potential at site x caused by other charges in the given boundary conditions, \vec{F} an applied electric field and r_{ij} the vector from site i to j . Ionization potential (IP) differences for a hop from site i to site j are given by:

$$\Delta IP_{ij} = [IP_j^0 - |q|\Phi_j^{dyn}] - [IP_i^0 - |q|\Phi_i^{dyn}] - |q|\vec{F} \cdot \vec{r}_{ij} \quad (3.3.5)$$

where IP_x^0 is the ionization potential of molecule x at zero charge concentration.

EA_x^0 and IP_x^0 are calculated for a sample of a few hundred molecules using the Quantum Patch method[58] described in Chapter 2.3. In a pure isotropic material, the static part of the sample wide density of onsite energies is assumed to follow a Gaussian distribution.

$$g(E) = \frac{1}{\sigma\sqrt{2\pi}} e^{-\frac{E^2}{2\sigma^2}} \quad (3.3.6)$$

One contribution to the onsite energy is thereby due to conformational disorder, a second distribution due to the inhomogenous electrostatic potential created by the other

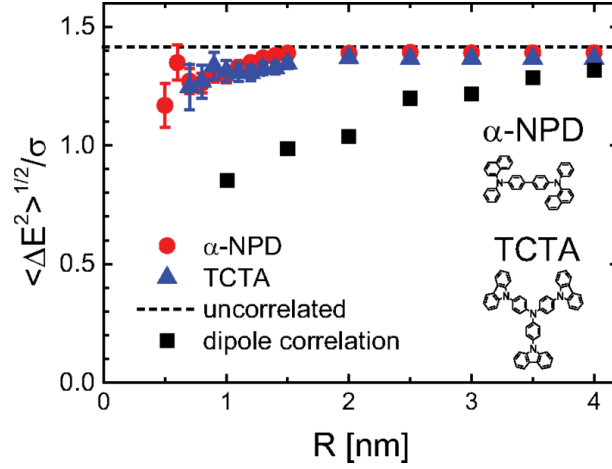


Figure 3.3.4: Spatial correlation of molecular IPs for two hole conductors α -NPD and TCTA and in a system where the total disorder is originated from monopole-dipole interaction. (image source: [38])

molecules[58].

The electrostatic contribution to the EA/IP on site i is to first order due to the monopole - dipole interaction of the added charge with the dipole moments of the surrounding molecules.

$$V_i^{EA^0/IP^0} = \pm \sum_{j \neq i} \frac{|q|}{4\pi\epsilon_0\epsilon_r} \frac{r_{ji}^{\vec{}} \cdot \vec{d}_j}{|r_{ij}|^3} \quad (3.3.7)$$

where the sum is over all surrounding molecules, \vec{d}_j the dipole of molecule j and r_{ij} the distance between site j and i . As neighboring sites feel a similar electrostatic environment, this electrostatic contribution to the onsite energy is spatially correlated.

The distribution of onsite energies for the $O(10^6)$ sites morphology is then generated as:

$$EA^0/IP^0 = a \cdot G_i + b \cdot V_i \quad (3.3.8)$$

where G_i is a random number drawn from $g(E)$, where σ is obtained from a fit of the EA/IP distributions from the Quantum Patch method, V_i is calculated from randomly oriented dipoles where the dipole strengths are obtained from Quantum Patch, a and b are fitting parameter chosen such that σ and a distance dependent energy correlation function $c = \sqrt{\langle \Delta E^2 \rangle (r)} / \sigma$ of the generated distribution matches the Quantum Patch data.

Fig.3.3.4 shows the spatial correlation of ionization potentials for the two hole conductors α -NPD and TCTA.

Coulomb interaction To calculate the dynamic contribution to eq.3.3.2 Φ_x^{dyn} caused by free charges in the OSC we need to consider the boundary conditions of the device. In bulk calculations I assume a periodic distribution of free charges and a coulomb cutoff that effectively calculates coulomb interactions as the interaction of every free charge, with the closest periodic image of all other free charges in the system.

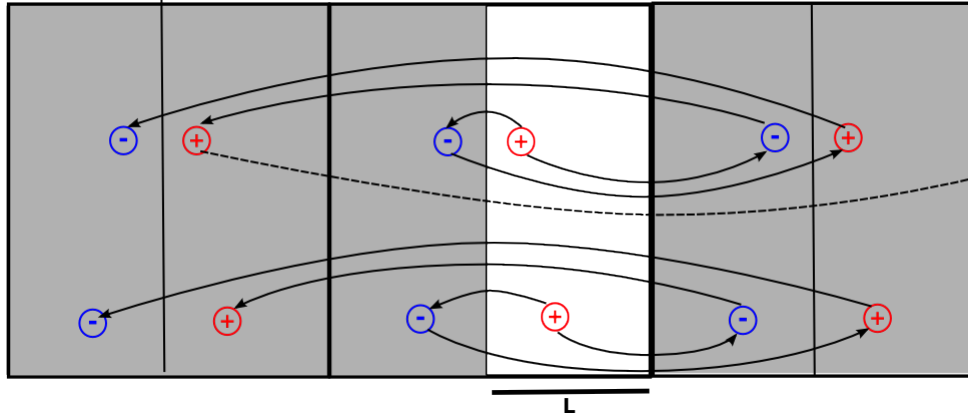


Figure 3.3.5: An OSC (white) connected to metallic contacts (grey). There are two holes in the system, which induce screening charges in the metal. An infinite series of image charges emulates the screening effect. If the simulation box L of the system is extended to include an electrode of the same size including the image charges, the netto charge in this extended system is 0. Periodically repeating the dipoles of this system generates the screening charges of the two electrode system.

As the coulomb potential does not only has to be calculated on the site of charges but also on potential hopping destinations at every kMC step, calculating the coulomb interaction to 27 periodic copies would slow down calculations severely. To mitigate this problem I introduce the following expression to calculate the closest periodic vector between two points in the simulation box.

$$\vec{r}_{ij} = (\vec{r}_i - \vec{r}_j + \text{floor}([\vec{r}_j - \vec{r}_i] \text{cdiv} \vec{P} + 0.5) \text{cprod} \vec{P}) \quad (3.3.9)$$

Where \vec{P} are the dimensions of the simulation box in x,y,z directions, cdiv/cprod operators, which perform a component wise division/product of two vectors. The coulomb potential at the site x Φ_x^{dyn} is then simply given by:

$$\Phi_x^{dyn} = \frac{1}{4\pi\epsilon_0\epsilon_r} \sum_j \frac{q_j}{\hat{r}_{xj}} \quad (3.3.10)$$

Where j sums over all charges except on site x and \hat{r}_{xj} is the closest periodic distance as defined above.

Calculations involving electrodes have to fulfill more involved boundary conditions, as the electrostatic potential at the leads has to be constant. Consider a system with two parallel slab electrodes as illustrated in fig. 3.3.5. The holes in the system need to be screened by an infinite series of mirror charges. The coulomb potential created by the charges and the series of image charges can be calculated easier if we ignore the boundary conditions of one of the electrodes and mirror all charges on the other electrode. If we repeat the compound system of charges and mirror images periodically the effect of the second electrode is reintroduced. This representation of the problem has the advantage,

that the individual periodic copies are charge neutral, so that the infinite series can be solved by an ewald sum [96].

$$\Phi_x^{dyn} = \frac{1}{4\pi\epsilon_0\epsilon_r} \sum_{\vec{n}} \sum_j^{2N} q_j \frac{erfc(\alpha|\vec{r}_{xj} + \vec{n}|)}{|\vec{r}_{xj} + \vec{n}|} + \frac{4\pi}{Vol_{sb}} \sum_{\vec{k} \neq 0} \sum_{j=1}^{2N} \frac{q_j}{|k|^2} e^{-\frac{|k|^2}{4\alpha^2}} \cos(\vec{k} \cdot \vec{r}_{xj}) \quad (3.3.11)$$

where j sums are over all charges, excluding an eventual charge on site x and its image, α is the Ewald parameter, \vec{k} the reciprocal space lattice vector $(2k_x\pi/L_x, 2k_y\pi/L_y, k_z\pi/L_z)$ (with $k_{x,y,z} = 0, 1, -1, \dots$), \vec{n} real space lattice vectors and $Vol_{sb} = 2L_xL_yL_z$ the volume of the simulation box.

As the explicit evaluation of this sum at every step for every potential hopping site is very expensive, I developed the following scheme to mitigate the computational cost. First a rectangular grid (L,L,L) with the same density of points as there are molecules in the amorphous morphology is introduced. Every molecule site x in the morphology is then assigned its closest grid point x' . The Ewald sum 3.3.11 is then split in two contributions.

$$\Phi_x^{dyn} \approx \left[\frac{1}{4\pi\epsilon_0\epsilon_r} \sum_j^N q_j \frac{1}{\hat{r}_{xj}} - q_j \frac{1}{\hat{r}_{xj^i}} \right] + [\Phi_{x'}^{dyn} - \frac{1}{4\pi\epsilon_0\epsilon_r} \sum_j^N q_j \frac{1}{\hat{r}_{x'j'}} - q_j \frac{1}{\hat{r}_{x'j^i}}] \quad (3.3.12)$$

where the first part of the sum is the coulomb potential on x caused by the closest periodic copies of all charges j and by the closest periodic copy of the closest image charges j^i of charges j , calculated with eq. 3.3.2. The distances are thereby the real distances of the amorphous morphology.

The second part of the sum consist of the full Ewald sum $\Phi_{x'}^{dyn}$ on the grid defined earlier, minus the (grid) interaction with the closest periodic charge and its first image charge. In effect long range interaction is treated on a grid, while short range interaction is treated accurately.

Due to the translational symmetry of the grid in directions parallel to the electrode, the Coulomb interaction of every grid point with every other Grid point correspond to $L \cdot L^3$ entries of data. It is thus possible to solve the second part of the sum in advance of an kMC calculation. During the simulation the calculation of coulomb interactions involves then the explicit calculation of the interaction with the nearest copies of the charges in the system and a (non-trivial) memory access to the tabulated data to correct for the long range interaction.

Excitation energies Excitation energies are approximated as independent from the coulomb field and as opposed to EA and IP as spatially uncorrelated, as the possible dipole - dipole correlation of an excitation with the dipoles of surrounding molecules is weaker then the monopole - dipole interaction taken into account for in the EAs and IPs. The approach to assign excitation energies is in principle the same as used for the uncorrelated part of EAs and IPs. Using the Quantum Patch method (Chapter 2.3), excitation energies are calculated for a representative distribution of

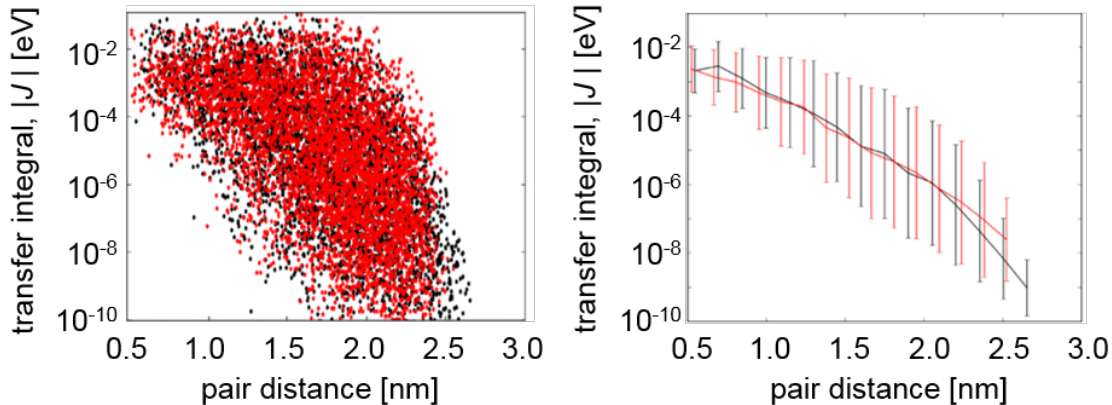


Figure 3.3.6: Stochastic expansion of the distribution of host-host hole transfer integrals for α -NPD:Ir(MDQ)2(acac). (a) The distribution of transfer integrals as obtained from the quantum patch method (black) and as generated for the stochastic morphology (red). (b) The distance dependent average and standard deviation of the distribution.

molecules. Excitation energies of molecules in the mesoscopic model are then assigned from a Gaussian fit to the microscopic data. In practice, although implemented in the developed transport model, this method was not applied for calculations in this thesis.

3.3.3 Transfer integrals

To calculate the Marcus rate of charge transfer from one molecule to another in a given pair, a transfer integral has to be assigned to the pair. For that purpose, the center of mass distance dependent distribution of transfer integrals of host-host, host-guest and guest-guest pairs is determined from the transfer integrals of a few thousand pairs of molecules, which are calculated on an atomistic morphology using the Quantum Patch method, see Chapter 2.3. For this, the pair distances of all pairs for which transfer integrals J_{ij} were calculated are binned in 100 intervals labeled by k . The decadic logarithms of the absolute value of the transfer integrals in each distance bin are divided into 100 intervals labeled by m . Each bin (k, m) is weighted according to the transfer integrals J_{ij} in its vicinity, with a weight

$$\omega_{km} = \sum_{n=k-2}^{k+2} \sum_{\langle ij \rangle \in n} \exp \left[-\frac{(\log_{10} J_m - \log_{10} J_{ij})^2}{2\sigma_k^2} \right] \quad (3.3.13)$$

where the parameter σ_k is chosen equal to five times the $\log_{10} J$ bin width. The first sum is over the 5 closest distance bins to m , the second sum is over all pairs in this bins. Finally, for each pair of sites of the mesoscopic morphology the appropriate distance bin k is determined and a J_k is randomly drawn according to the distribution of weights ω_{km} . Fig. 3.3.6 gives an example of a comparison between hole transfer integrals calculated with the quantum patch method and with the stochastic expansion method for the HOMO orbitals of α -NPD. If a morphology contains different types of molecules, the distance

dependent probability of transfer integrals is determined for each kind of pair in the system. Every pair then draws its transfer integral from the according distribution. This way of assigning transfer integrals then accounts also for different couplings between different types of molecules if the molecule type was not taken into account during the morphology generation.

3.3.4 Reorganization energy

Reorganization energies are calculated with Nelsens four point procedure described in chapter 2. The packing of molecules in the morphology results in a restriction of the conformational degrees of freedom. In particular dihedral rotations of groups of atoms, though energetically cheap, are restricted due to collisions with neighboring molecules. The reorganization energies used in this thesis are therefore calculated using a frozen dihedral approximation [94], which only allows conformational changes of linear degrees of freedom.

This way the difference between the molecule specific reorganization energies is not taken into account. In a more involved quantum chemical approach, reorganization energies for a limited number of molecules are calculated by confining the motion of individual molecules in DFT by the use of effective core potentials on the position of the atoms of neighboring molecules from the morphology. The distribution of reorganization energies can then be fitted. The resulting fit is then used to assign reorganization energies to all molecules in the system.

3.4 Kinetic Monte Carlo

In this section, the representation of the OSC device in the simulation and the algorithm to propagate its state in time is described. In 3.4.1 the algorithm to propagate particles in the organic semi conductor model is presented. In 3.4.2 I will point out some of the numerical challenges of kMC simulations of organic semi conductors. In 3.4.3 I will then present an algorithm to alleviate some of these problems.

3.4.1 Propagation of particles in the organic semiconductor

The amorphous material is represented by the sites which correspond to the center of mass positions of the molecules in the material. Possible sites are restricted to a rectangular simulation box with specified x,y and z size (typically 50-100nm per dimension). Depending on the simulation and device type, the topology of the sites obeys periodic boundary conditions in some or all dimensions. Every site has assigned specific ionization potential, electron affinity, 1st excitation energy, reorganization energy, dipole moments and transition dipole moments. Ionization potentials and electron affinities are thereby time-dependent quantities, while the remaining properties are considered constant in time. Charges and localised Frenkel-excitons are represented as point like entities occupying these sites. Electrons and holes can be created on sites within a few nm distance to virtual electrodes planes or by the dissociation of an exciton. Annihilation of charges can equally occur on sites close to an electrode or by electron hole recombination. Excitons are either created by charge recombination or on any empty site according to a defined irradiance and absorption probability. Excitons can be destroyed by radiative decay, dissociation or by energy transfers to other particles in the system or to the electrodes. Every particle can hop to other sites. A detailed description of possible processes and their corresponding rates can be found in 3.2.

Due to the weak coupling between the molecules, we consider the hopping as a Markov process, such that the state of the system at a given time is fully given by the position of all particles. Let $\Gamma^{irr} = \sum_{a=1}^N \omega_a^{irr}$ be the total exciton creation rate due to light absorption, where N is the number of sites in the simulation box, $\Gamma^{inj} = \sum_{a=1}^M \omega_a^{inj}$ the total charge injection rate, where $M < N$ is the number of molecules within a cutoff to the electrodes, and $\Gamma^{eject} = \sum_{i=1}^{n_c^M} \omega_i^{eject}$ the total charge ejection rate, where n_c^M is the number of charges within a cutoff to the electrodes. $\Gamma^{ct} = \sum_{i=1}^{n_c} \sum_{a=1}^{N_i^{ct\ targets}} \omega_{i,a}^{ct}$ is the total charge transfer rate, where n_c is the number of charges in the system and $N_i^{ct\ targets}$ the number of sites to which the i-th charge can hop. The total exciton transfer rate is given by $\Gamma_{eet} = \sum_j^{n_e} (\sum_{a=1}^{N_j^{ct\ targets}} \omega_{j,a}^{Dexter} + \sum_{a=1}^{N_j^{eet\ targets}} \omega_{j,a}^{Foerster})$, where n_e is the number of excitons and $N_j^{eet\ targets}$ the number of molecules considered for a Förster type energy transfer. The total rate for charge separations of excitons is given by $\Gamma^{ehs} = \sum_{j=1}^{n_e} \sum_{a=1}^{N_j^{ct\ targets}} (\omega_{j,a}^{ehs} + \omega_{j,a}^{hes})$, where the charge separation can either take place by an electron transfer to a neighboring molecule (ehs) or a hole transfer to a neighboring molecule (hes) (the number of states one exciton can dissociate to is 2 times the number of molecules to which a charge transfer is possible). $\Gamma_{\tau} = \sum_j^{n_e} \frac{1}{\tau_j}$ is the total exciton decay rate due to radiative decay. All rates

involving charges and exciton separation rates depend on the electrostatic potential. If a possible transfer process would move a particle on an occupied or otherwise specially marked site, the transfer rate is modified in accordance with possible interactions (e.g. electron hole recombination or exciton energy transfer to another particle). The total rate for scattering the system in a new state is then given by:

$$\Gamma_{total} = \Gamma^{irr} + \Gamma^{inj} + \Gamma^{eject} + \Gamma^{ct} + \Gamma^{eet} + \Gamma^{ehs} + \Gamma^{\tau} \quad (3.4.1)$$

The probability for the system to remain in its state after a time Δt is then given by $p(\Delta t) = e^{-\Gamma_{total}\Delta t}$. To discretely propagate the system in time a random number distributed like $p(t)$ is drawn. Let us make a list of the rates of all possible transitions ω_x and define the cumulative function of the rates as $\omega_x^{cum} = \sum_{y=1}^x \omega_y$. To determine the change of the system state, a random number $\omega_u \in (0, \omega_N^{cum}]$ is drawn, where ω_N^{cum} is the last element of the cumulative function and the process i corresponding to the rate for which $\omega_{i-1}^{cum} < \omega_u \leq \omega_i^{cum}$ holds (see 3.4.1), is then executed to obtain the new state at time $t + \Delta t$. All rates ω_x are then recalculated and the next iteration step is executed (for a flowchart of the basic algorithm, see 3.4.2. If all processes in the system are Poisson processes, this algorithm will yield the correct time scale for the time evolution of the system under the condition that all processes are independent.

To obtain steady state expectation values for various physical properties such as electric current, charge carrier mobility, charge distribution or the photo conversion efficiency of a device, the system is propagated until the electric current becomes constant. To track convergence, the cumulative drift velocity $v(t, t')$ of electrons and holes in the time interval $t' - t$ is defined as $v(t, t') = \frac{\sum_{i=1}^{n(t, t')} q_i \frac{\vec{F}}{F} \cdot \Delta \vec{R}_i}{t' - t}$, where $n(t, t')$ is the number of Monte-Carlo steps in the time interval $t' - t$ involving a translation of charge, q_i the sign of the charge translated in step i , R_i the displacement of the hopping charge in the i th step and \vec{F} an applied electric field. A calculation is considered converged if the velocities $v_1 = v(t_1, t_2)$ and $v_2 = v(t_2, t_{total})$ obey the condition $|1 - \frac{v_2}{v_1}| < c_{DC}$ and $v_2 \cdot (t_{total} - t_2) > d_{min}$, where c_{DC} is a convergence criterion, t_{total} the total simulation time, $t_2 = \frac{2}{3}t_{total}$, $t_1 = \frac{1}{3}t_{total}$ and d_{min} a minimum displacement of the charge in the system. The latter condition ensures that a calculation does not stop if all charges are stuck in traps for a long time, such that the velocities v_1 and v_2 could both be equal zero before a steady state is reached. Both convergence conditions are assessed every N_{iter} number of Monte-Carlo steps, where N is in practice in the order of 10^5 . c_{DC} has to be chosen as a compromise between accuracy and computational cost. In slowly equilibrating systems, the sign of the derivative of velocities in at least three time intervals is used to estimate whether the system is still equilibrating.

To efficiently draw the process i corresponding to the rate for which $\omega_{i-1}^{cum} < \omega_u < \omega_i^{cum}$ holds, a logarithmic scaling tree search can be employed. We define a lower interval boundary $I_{lower} = 0$, an upper interval $I_{upper} = N$ and an index $i_{middle} = \text{floor}((I_{lower} + I_{upper}/2))$, where floor rounds down to the next integer, and N is the total number of possible transitions. If $\omega_u > \omega_{i_{middle}}$, the new lower interval boundary is set to $I_{lower} = i_{middle}$, otherwise the upper interval boundary is set to $I_{upper} = i_{middle}$ and i_{middle} is recalculated as

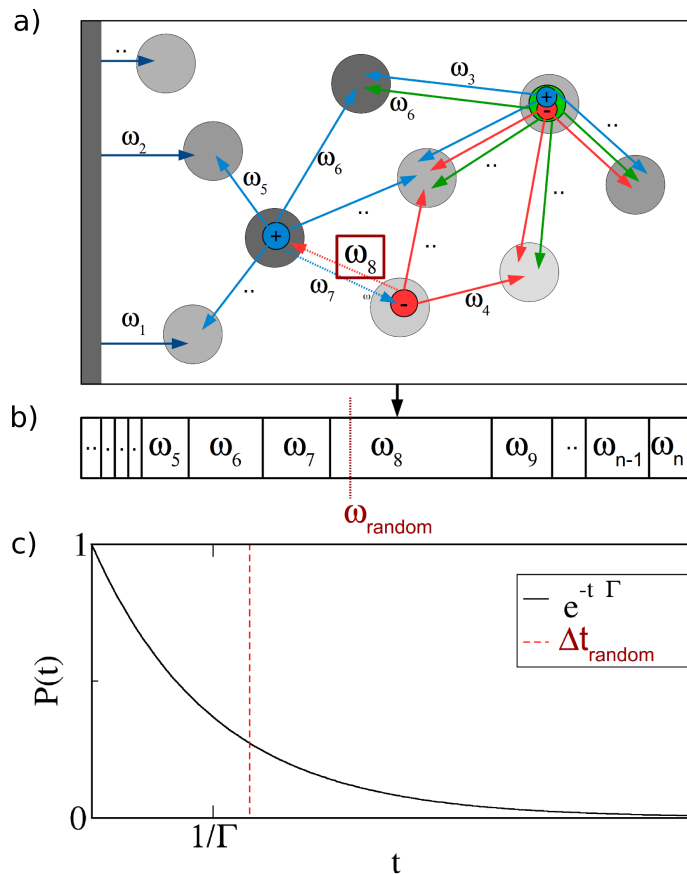


Figure 3.4.1: a) Sketch of a state of an OLED representation and possible transitions: Grey circles illustrate center of mass points of molecules, blue/red extra electrons/holes on a molecule, green strongly bound excitons. The dark blue lines on the left represent electron injection events, blue lines electron transfer, red lines hole transfer, green lines exciton transfer. The exciton can separate into an only coulomb bound electron hole pair by charge transfer of electron or hole to another molecule. b) The System is propagated by executing one of the transitions described in a). The transition is selected randomly. The probability to select a transition is proportional to its rate, ω_{random} represents a random number which would select event 8. The probability $p(t)$ of the system to stay in the same state after time t is shown in c). The time step of the kinetic Monte-Carlo algorithm is drawn according to $p(t)$, where the lifetime of the state is given by the inverse of the sum of the rates of all transitions. In the illustrated example the time step Δt_{random} is drawn.

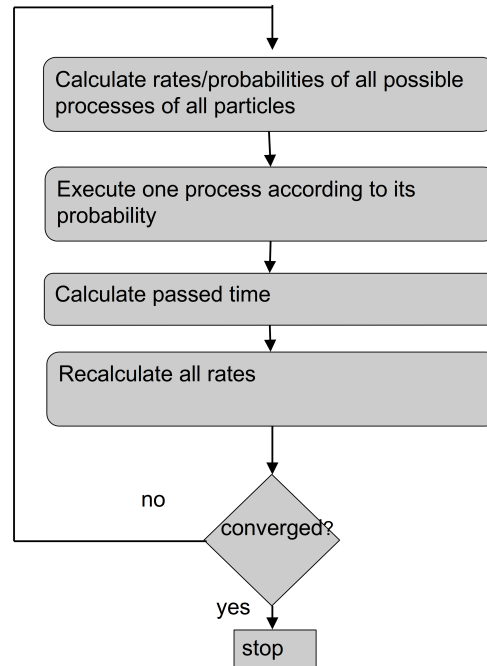


Figure 3.4.2: Flowchart of the basic kinetic Monte-Carlo algorithm. The event and time selection step is illustrated in more detail in fig. 3.4.1.

$i_{middle} = \text{floor}((I_{lower} + I_{upper}/2))$. This is repeated until $I_{upper} - I_{lower} < 2$. If this condition is met, I_{upper} is returned as the label of the selected process to be executed.

3.4.2 Computational challenges

In this section I will discuss computational challenges in performing kMC charge transport simulations.

Evaluation of rates To simulate the real dynamics of the system, all possible processes and their rates have to be reevaluated after each time step. To illustrate the computational cost of this, let us consider an electron and hole on neighboring molecules. According to 3.2, their recombination rate depends on the coulomb potential caused by other charges in the system. Over time, the potential difference between the molecules will have peaks and valleys, which will determine a recombination rate which will, due to its exponential dependence on the potential difference 3.2 be very different from a recombination rate obtained from an time-averaged potential. For a system with dimensions of order $100 \times 100 \times 100 \text{ nm}^3$, this means that $O(10^4)$ injection rates alone have to be recalculated every step. Adding the rates for an estimated charge concentration of 10^{-3} per molecule and about 20-30 possible hopping targets per charge, we see that we might need to evaluate $O(10^5)$ rates per Monte-Carlo step, most of these depending on the dynamic coulomb potential.

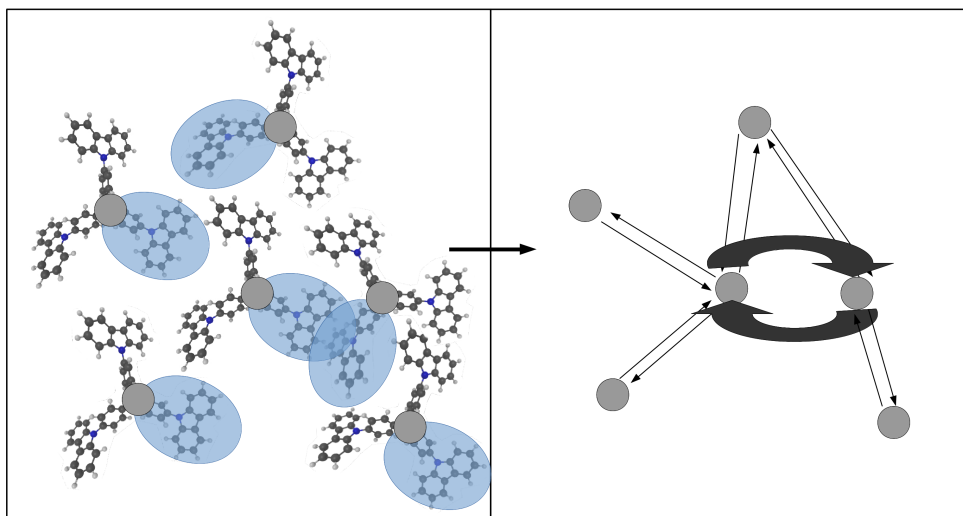


Figure 3.4.3: Numeric loops in the kinetic Monte-Carlo simulation of charge hopping. On the left the illustration of a cluster of six typical molecules used in OLEDs. Gray spheres lie at their center of mass, blue semi-transparent ellipses represent the HOMO of the individual molecules i.e. the state a hole would occupy. Localization of the hole states to one group of the molecules would in this example be caused by the rotation of the aromatic groups. The HOMO of the middle molecule has the biggest spatial overlap with the HOMO of the molecule to its right. On the right, the electronic coupling of the middle molecule to its neighbors. A strong coupling (relative to the other couplings), leads to high rate for hops back and forth between the molecules, such that a simulation may be stuck in a loop where charge hops back and forth for a long (simulation) time.

State rattling A strongly varying distribution of hopping rates in a disordered organic semi-conductor leads to "rattling" of charges between a small number of states, during which the computation is effectively trapped in a loop. Consider the cluster of TCTA molecules illustrated in 3.4.3. The HOMO orbitals of two of these molecules might be localized such, that they have a big spatial overlap, but a small spatial overlap with HOMOs of other molecules. The electronic coupling between these two HOMOs will then be orders of magnitude larger than the coupling that connects either of the molecules with the HOMOs of other molecules. In terms of a flux matrix

$$I = \begin{bmatrix} 0 & \omega_{12} & \omega_{13} & \dots & \omega_{1n} \\ \omega_{21} & 0 & \omega_{23} & \dots & \omega_{2n} \\ \vdots & \vdots & \vdots & \ddots & \vdots \end{bmatrix} \quad (3.4.2)$$

this means that there will be some blocks in the flux matrix which are nearly decoupled from the rest of the matrix, but have a strong coupling inside the block. As electronic coupling and HOMO energies are statistically distributed in the system, there will always be such blocks in the flux matrix if the system is big enough.

In the kinetic Monte-Carlo simulation, charge hopping in this closed subsystem will dominate while almost no time passes as the expectation value for a time step is inverse proportional to the sum of the total rates, which in this case may be dominated by huge rates of this "rattle" in the subsystem e.g. the hop between two

strongly coupled molecules. Energy disorder worsens this effect significantly, as it reduces the number of viable hopping targets. In practice, calculations will spend most of the time in such loops. In the following section I will present two approaches I developed to speed up kinetic Monte-Carlo simulations which are stuck in loops like this.

3.4.3 Kinetic Monte-Carlo state buffer

For calculations involving non-interacting particles it is possible to pre-calculate the rates of all possible transitions in the system and draw the new set of rates after each change of the system state from memory, thus reducing the kinetic Monte-Carlo algorithm to a memory access and the drawing of the new event. For a system of interacting particles, as is the case here, this is of course not possible as the number of possible system states is roughly $\binom{N}{K}$ where N is the number of system sites and K the non-conserved number of particles in the system.

The number of likely particle configurations is however much smaller. In equilibrium, likely configurations could be predicted by solving the Master-equation of the system (a non-trivial task by all means). As we are also interested in non-equilibrium this is not applicable to kinetic Monte-Carlo simulations in general however. If it would however be possible to track the many-particle configuration state of the system on the fly, a set of the N most likely states $S_\Phi(t)$ in the time-local environment of the current state $\Phi(t)$ in configuration space could be determined. If the system has computational loops as described above, the occupied configuration sub-space changes only slowly in time, meaning likely configurations will stay likely configurations for a long time. If during further propagation the system is in state $\Phi(t')$, which is a state in $S_\Phi(t)$, all system rates and the coulomb potential can be tabulated such that in the next occurrence of the state, the system update only involves a memory access to priorly calculated rates. If the system evolves slowly enough (e.g. a system with many rattles), rates for all likely states in $S_\Phi(t)$ can be tabulated, thus increasing computational time significantly. This algorithm will work the better, the "worse" the system propagates e.g. at high energy disorder. A flow-chart of a kinetic Monte-Carlo algorithm using this scheme is shown in 3.4.4.

Tracking of the system configuration states is however non-trivial. The system may have around 10000 particles, such that any state would be described by a 10000 dimensional vector $\vec{X}_\Phi(t)$, which identifies the position of every particle (only one coordinate per site is required as all molecules can be labeled). As the algorithm described above requires a continuous tracking of all system states, it is a) clearly unfeasible to track $\vec{X}_\Phi(t)$, and b) computationally very expensive to compare states to each other or create a probability distribution for the different $\vec{X}_\Phi(t)$. To bypass this problem, I introduce a contraction operator C which maps the state vector $\vec{X}_\Phi(t)$ on a scalar

$$\hat{X}_\Phi(t) = C(\vec{X}_\Phi(t)) \quad (3.4.3)$$

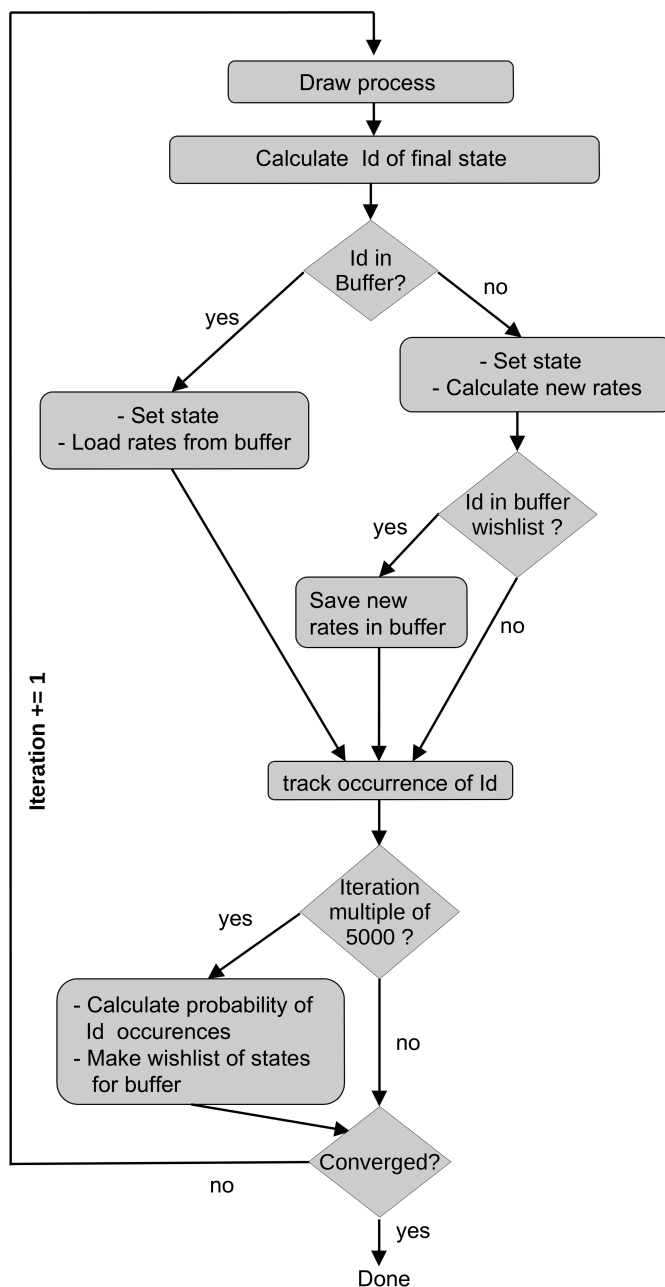


Figure 3.4.4: Flowchart of a kinetic Monte-Carlo algorithm using a buffer to memorize information about likely configurations of the system. After a Monte-Carlo move is selected, it is checked whether it has been performed before. If it has been performed before, all rates and the coulomb potential are updated from computer memory. During a calculation, it is tracked how often states occur. For the most likely states, rates and Coulomb potentials are stored in the computer memory.

where I define C by

$$C(\vec{X}_\Phi(t)) = \sum_{a=1}^{a=A} \sum_{i=1}^{i=n} c_a(q_i + 2) f(X_\Phi^i(t)) (X_\Phi^i(t))^a \quad (3.4.4)$$

where n is the number of particles in the current state, A the order of the expansion, c_a and expansion coefficient, q_i the charge of particle i , f a map $\mathbb{N} \rightarrow \mathbb{N}$. The purpose of $f(X_\Phi^i(t))$ is to decrease the chances of two states $\vec{X}_\Phi(t)$ being mapped on the same number $C(\vec{X}_\Phi(t))$. It may for example be $f(X_\Phi^i(t)) = X_\Phi^i(t) + 1000$. Although the map may not be unique for a finite A , the higher the order of the expansion the less likely it is for two different states to be mapped on the same scalar. In practice, the likelihood that two states \vec{X}_Φ from the same environment $S_\Phi(t)$ are mapped on the same scalar for $A=2$, is so small that it never occurred in my test calculations. If we however assume an erroneous identification of $\vec{X}_\Phi(t)$ with an already tracked state $\vec{X}_\Phi(t')$ every N Monte-Carlo steps, this would mean that every N steps the rates out of the current state would be wrong, however there would still only be transitions possible to the correct final states, as only numerical values for rates, but no process information is tabulated. In the next step, rates for all transitions are again obtained "from a white sheet", such that the impact of an erroneous identification of a state on the overall calculation is extremely small if $N \gg 1$ (In practice N seems to be bigger than the total number of simulation steps until convergence).

This scheme to track system states can be further accelerated significantly if we use the fact that per Monte Carlo step at most three particles (in case of electron - hole recombination) will change their position. Therefore that it is sufficient to calculate the change in $\hat{X}_\Phi(t)$. For a charge translation the sum over particles in 3.4.4 disappears and $d\hat{X}_\Phi(t)$ is given by:

$$d\hat{X}_\Phi(t) = \sum_{a=1}^{a=A} c_a(q_i + 2) [f(X_\Phi^i(t(n))) (X_\Phi^i(t(n)))^a - f(X_\Phi^i(t(n-1))) (X_\Phi^i(t(n-1)))^a] \quad (3.4.5)$$

where n is the current Monte-Carlo iteration and i the label of the translated particle. The additional computational cost of this state tracking scheme are insignificantly small compared to the logarithmic scaling Monte-Carlo selection algorithm which determines the next system transition as described earlier. This means that this scheme can be used in all kinetic Monte-Carlo simulations of the kind as performed in this thesis. A computational limitation of this scheme is the size of the set $S_\Phi(t)$ of likely states, as for all of these states, all rates and the local coulomb potential have to be saved. The computer memory needed to tabulate this data scales linearly with the number of particles. Given 10000 particles with an average of 20 target molecules in their hopping range, the rates for roughly 200000 events, corresponding to 1.6 Megabyte of memory, would need to be saved for every state. In order to keep the size of the set $S_\Phi(t)$ reduced, a list of likely states in the set $S_\Phi(t)$ for which the rates are to be tabulated is updated every M Monte-Carlo steps, based on the distribution of states visited in the last M Monte-Carlo steps. This ensures that $S_\Phi(t)$ always contains the most likely states in the current environment of configuration space, also with limited computer memory resources.

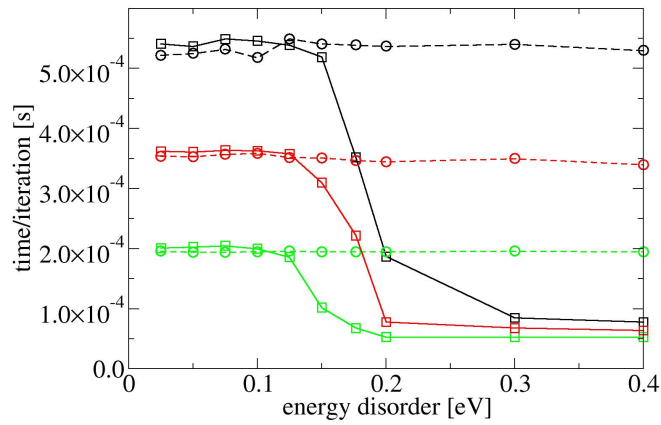


Figure 3.4.5: Calculation time per kMC step dependent on disorder of the electronic states for 10 charges (green), 50 charges (red) and 100 charges (black). Full lines and circles represent calculations with an algorithm integrating a state buffer, dashed lines and squares calculations without a state buffer.

Fig. 3.4.5 shows the increase in calculation speed gained through a mobility buffer dependent on disorder strength and electron concentration. For large disorder strength, computational time of one simulation step is reduced to a similar computational overhead for all electron concentrations. This means, that at very large disorder the increase in computational speed is the higher the more electrons are in the system. In Guest Host systems (see 5), the deep trap states in emitter molecules lead to a situation like this.

Chapter 4

Charge carrier transport in bulk systems

In this chapter I will validate the kinetic Monte-Carlo charge transport model introduced in chapter 3 by comparing field and temperature dependence of bulk-hole mobilities of the prototypical organic hole transport material N,N'-bis(1-naphthyl)-N,N'-diphenyl-1,1'-biphenyl-4,4'-diamine (α -NPD)(see, Fig. 4.0.1) with experimental values. I will further analyse percolation pathways of the charge carriers depending on the intrinsic material parameters. In the last part of this chapter I will compare bulk mobilities calculated with kinetic Monte Carlo with the Generalized effective medium model[[35]], a model which does not require explicit charge transport calculations.

4.1 Charge mobility in α -NPD

N,N'-bis(1-naphthyl)-N,N'-diphenyl-1,1'-biphenyl-4,4'-diamine (α -NPD) is a prototypical organic hole conduction material used in many OLEDs. Doped with hole donating molecules it serves as a hole injection layer [74], undoped it is used as hole-transport layer [34], and doped with dye molecules it is used to produce red light emitting layers [34].

To simulate charge transport in α -NPD, I use the multi-scale protocol described in Chapter 3.3 to create a periodic $60 \times 60 \times 60 \text{ nm}^3$ α -NPD morphology, transfer integrals between

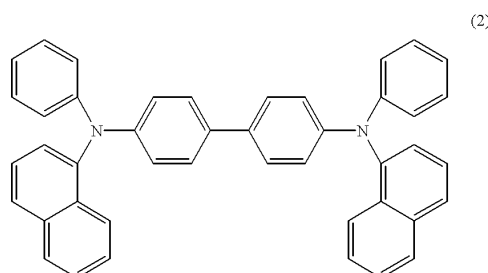


Figure 4.0.1: Schematic picture of the organic hole transport material *alpha*-NPD, investigated in this chapter.

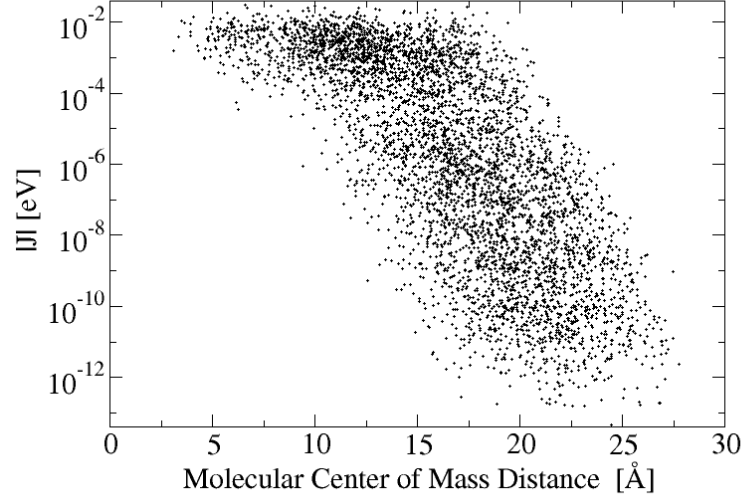


Figure 4.1.1: Distribution of hole transfer integrals of α -NPD against the center of mass distance of pairs of α -NPD molecules.

pairs and HOMO energies of the molecules. The resulting morphology has a packing density of $0.98 \text{ molecules}/\text{nm}^3$. Electronic structure calculations yield a standard deviation of the HOMO energy disorder of $\sigma=0.09 \text{ eV}$ and an average reorganization energy of $\lambda=0.2\text{eV}$. The calculated α -NPD hole transfer integrals are shown in Fig. 4.1.1. A bulk charge transport simulation is started by successively creating holes on sites i with the probability

$$p_i = \frac{1}{\exp(\frac{E_i - E_f}{k_B T}) + 1} \quad (4.1.1)$$

until the desired hole concentration is reached. E_i is the HOMO energy of the site i , E_f the lowest HOMO energy of unoccupied sites, T the temperature and k_B the Boltzmann constant. To determine the field dependent mobility I measure the cumulated drift of all holes over time. The mobility is then given by:

$$\mu = \frac{d}{t F V n} \quad (4.1.2)$$

where d is the cumulated drift of all holes as shown in Fig. 4.1.2, t time, F the applied field, V the volume of the simulation box and n the density of charge carriers.

Fig. 4.1.3 shows the simulated hole mobilities at hole concentrations of 2×10^{-5} , 2×10^{-4} , 2×10^{-3} holes per molecule, the typical concentration regime in OLEDs. The calculated mobility field dependence presented in Fig. 4.1.3 shows excellent agreement with experimental mobility measurements[97]. Calculated mobilities for hole concentrations of 2×10^{-4} , 2×10^{-3} differ by roughly 15%, where a higher hole concentration leads to a higher mobility due to the filling of trap states [52]. At low fields, the mobility decreases roughly by factor of 4 for a hole concentration of 2×10^{-5} . I furthermore cal-

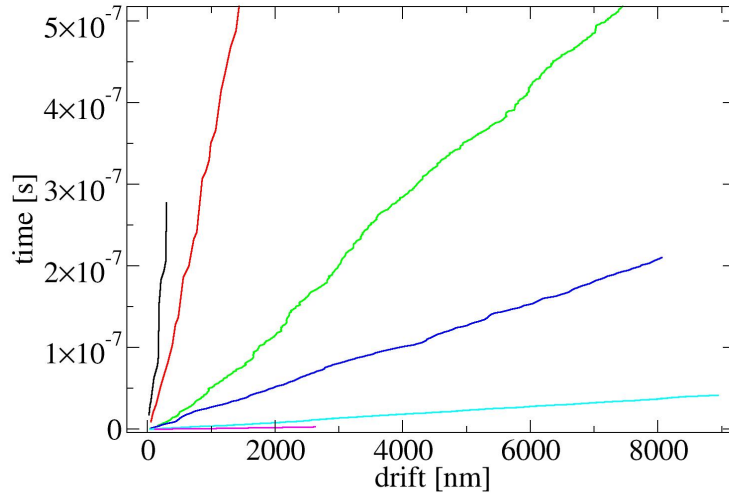


Figure 4.1.2: Cumulated drift of holes in field direction over time. Different colors correspond to different field strength: 0.005 V/nm (black), 0.01 V/nm (red), 0.015 V/nm (green), 0.0225 V/nm (blue), 0.031 V/nm (cyan), 0.04 V/nm (magenta).

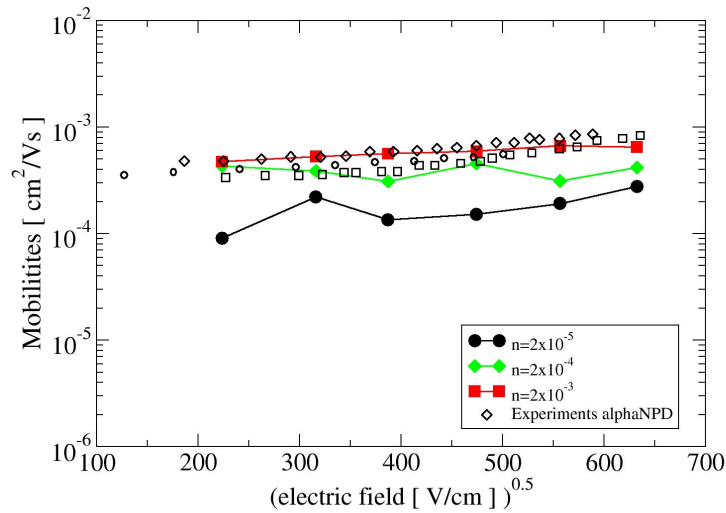


Figure 4.1.3: α -NPD bulk hole mobilities at various electric fields from experimental[97] time of flight measurements and from kMC simulations at different hole concentrations.

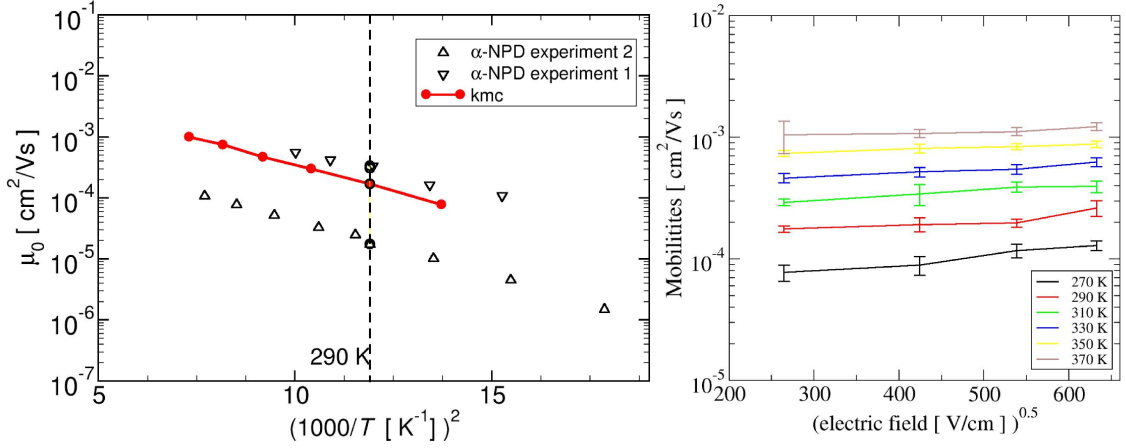


Figure 4.1.4: a) Temperature dependence of α -NPD bulk hole zero field-mobilities according to different experiments [98, 99, 100] and kMC calculations. b) Field and Temperature dependence of α -NPD bulk hole mobilities. Zero field mobilities shown in the left panel are extrapolated from these values.

culated the temperature dependence of α -NPD zero field hole mobilities, see Fig. 4.1.4. Zero field mobilities are determined by extrapolation of the mobility field dependence to zero field. The calculated mobilities are again in very good agreement with experimental measurements[98, 99, 100], both in terms of slope and absolute value. The logarithm of both measured and simulated mobility shows a linear dependence on T^{-2} .

In conclusion I have shown that both field and temperature dependence of α -NPD are predicted correctly in both slope and absolute value using the multi-scale model developed in the Wenzel group. I would like to emphasize that no fit parameters were used to calculate either morphology, electronic structure or charge transport. The excellent agreement of field and temperature dependence of the mobility, strongly suggests that the relevant physics is reflected in transport model, electronic structure and morphology calculations.

4.2 Current percolation in α -NPD

In this section I will analyze the hole current flow through the α -NPD bulk samples presented in the last section. To investigate the role of trapping during charge transport I calculated the fraction of time, which holes spent on a subset of molecules compared to the total simulation time. To do this I define the following:

$$t_s = \Gamma_t \sum_{j=1}^s t_j / t_{tot}, \quad (4.2.1)$$

where Γ_t orders all molecules by the total sojourn times t_j of holes spend on the molecules and t_{tot} is the total simulation time. The dependence of t_s on the energy disorder of the system is shown in Fig. 4.2.1 a). It can be seen that the higher the disorder the longer

the time holes spend on a smaller fraction of the system indicating increased trapping. In the case of energy disorder with standard deviation of $\sigma=5k_B$ and $\sigma=6k_B T$ about 95% of time holes stay on 0.1% of molecules. With decreasing disorder strength, the holes distribute more uniformly over the system.

For further analysis I define the net-current through a molecule i by

$$I_i = \sum_{j=1}^n \frac{|N_{ij} - N_{ji}|}{2} \quad (4.2.2)$$

where n is the number of molecules connected to molecule i and N_{ij} the integer count of charge carriers hopping from i to j . In order to quantify which fraction of the material contributes to the current flow I sort all sites by their contribution to the total current and define the current through the strongest conducting subset of s molecules as

$$I_s = \Gamma_c \sum_{i=1}^s \frac{I_i}{\sum_{i=1}^M I_i}, \quad (4.2.3)$$

where the net currents I_i through molecules i are ordered by the ordering operator Γ_c , such that the s molecules with the highest net current I_i contribute to I_s , M is the total number of Molecules in the system. Fig. 4.2.1 b) shows I_s in dependence on the number of contributing molecules s for disorder strength between $\sigma=1k_B$ and $\sigma=6k_B T$. A general trend of subsets of smaller size s contributing to more current can be seen with increased disorder. This is reflecting the increased percolative nature of the charge transport. A strict order of I_s with respect to disorder can however not be seen. This is due to the finite size of 200000 molecules per sample. The on-site energies in all samples are generated randomly following a Gaussian distribution of the defined width. As can be seen when looking at I_s for $\sigma=5k_B$ and $\sigma=6k_B T$, this randomness can create tighter percolation networks in samples of smaller disorder. Although I_s does not seem to be converged at this system size I would like to point out that the mobility is well converged and shows the expected order with respect to disorder (see *i.e.* Fig. 4.3.2).

As mobility should be less effected by the relative size of the percolation network than by the disorder in the network, I define the relative disorder of the x connections between molecules, which carry the largest net current as

$$\Delta E_x = \Gamma_I \frac{1}{\sqrt{x}} \sqrt{\sum_{i,j}^x \left[\sum_{i,j}^x \frac{\Delta E_{ij}}{x} \right] - \Delta E_{ij})^2 / \sigma_{\Delta E}}, \quad (4.2.4)$$

where Γ_I orders the sums over the x connections (i, j) with highest net current, $\Delta E_{i,j}$ is the difference of HOMO energies on molecules i and j , and $\sigma_{\Delta E}$ the standard deviation of all $\Delta E_{i,j}$.

The contribution of these x connections with the highest net current to the total current is given by

$$I_x = \frac{\Gamma_I \sum_{i,j}^x |N_{ij} - N_{ji}|}{\sum_{i,j} |N_{ij} - N_{ji}|}, \quad (4.2.5)$$

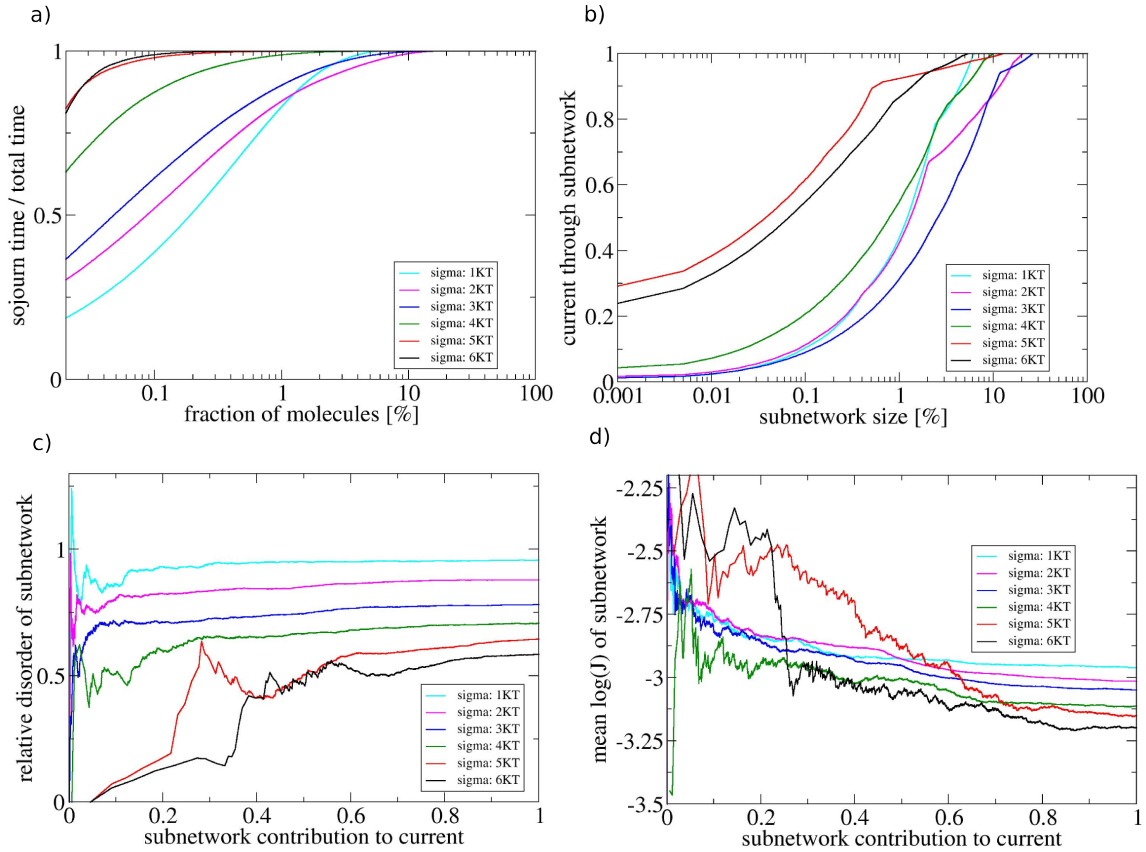


Figure 4.2.1: Measures of percolation transport depending on energy disorder. a) Fraction of the total simulation time (y-axis) which is spent on a fraction of the molecules of the system (x-axis) as defined in Eq.4.2.1. The x-axis is capped at 0.00002, which is the concentration of holes in the system. The higher the disorder, the longer the holes stay trapped on individual molecules. b) The fraction of the current (y-axis) as defined in Eq.4.2.3 which passes only through a fraction of the molecules (x-axis). The x-axis is capped where the network consists of only a single bond. From the low fraction of molecules that contribute to considerable current it is apparent, that the charge transport is very percolative. c) Energy disorder in the conducting network relative to the energy disorder of the entire morphology as defined in Eq.4.2.4 against the relative current through the network as defined in Eq.4.2.5. The number of contributing pairs is very small close to the y-axis. The higher the disorder of the network the system, the lower the relative disorder of the conducting subsystem. d) Decadic logarithm of the transfer integrals in the conducting network as defined in Eq.4.2.6 against the relative current through the network as defined in Eq.4.2.5. The larger the subsystems, the more the average transfer integrals decrease, where in networks of large disorder, the current goes through smaller transfer integrals.

where N_{ij} is the absolute count of charge carriers hopping from i to j . ΔE_x is plotted against the contribution of the subnetwork to the total current I_x in Fig. 4.2.1 c). The disorder ΔE_x at $I_x = 1$ is the disorder of the total network of connections which contribute to the current relative to the total disorder of the system. It can be seen that the higher the disorder the smaller the relative disorder in the current network becomes. This reflects that as HOMO energy differences rise on average with increased disorder, the current has to carefully select the bonds through which it flows with respect to energy differences. The price for this more refined selection is a decrease of the transfer integrals of the selected pairs. This can be seen in Fig. 4.2.1 d), where the average transfer integrals J_x used in the subnetwork (up to to the x largest pairs) are presented. J_x is defined for the same subnetwork as I_x and ΔE_x as

$$J_x = \Gamma_I \frac{1}{x} \sum_{i,j}^x \log_{10}(J_{ij}), \quad (4.2.6)$$

where J_{ij} is the transfer integral of the pair (i, j) .

In conclusion I analyzed the percolative behavior of hole conduction in an amorphous α -NPD morphology dependent on its HOMO energy disorder. As expected I found that the higher the disorder the less molecules contribute to the current. I also found that at low disorder the current chooses a network with, on average, larger transfer integrals than at high disorder, where good transfer integrals are 'sacrificed' to reduce energy differences between molecules.

4.3 α -NPD Mobility in the Generalized effective medium model

As explicit transport models like the presented kinetic Monte-Carlo model require an representation of the entire system, finite size effects are increasingly difficult to handle with increasing energy disorder. To avoid the problems of explicit material representations, Rodin *et al.* [35] derived a model to predict the upper bound of the charge carrier mobility based on microscopic input parameters.

In the model it is assumed that every molecule in the system can contribute to the charge transport. The model averages over all hopping rates in an amorphous morphology with Gaussian distributed HOMO/LUMO energies by weighting rates with the occupation probability of the involved molecular pair. Using Marcus hopping rates, an expression for the zero-field mobility is derived as[35]

$$\mu = \frac{\sqrt{\pi\beta}}{\hbar} \lambda^{\frac{3}{2}} \frac{e\beta}{n\sqrt{1 + \frac{\beta\sigma^2}{\lambda}}} \exp \left[-C(\beta\sigma)^2 - \beta\frac{\lambda}{4} \right] M \frac{\langle J^2 r^2 \rangle}{\lambda^2}. \quad (4.3.1)$$

where $\beta = (k_B T)^{-1}$ is the the inverse temperature, $n = 3$ the dimension, $\langle J^2 r^2 \rangle$ is the expectation value of the electronic coupling times center of mass distance of all pairs squared, λ the average reorganization energy, M the average number of neighbors considered per molecule and σ the standard deviation of the HOMO distribution. Under the

assumption that the hopping rates from all sites contribute to the overall mobility according to their occupation probabilities the parameter C is strictly $C=0.25$. As the transport in a strongly disordered system may follow a narrow percolation path, the mean medium assumption is not valid in this regime. To allow for this fact, C is introduced as parameter and the model is termed generalized effective medium model (GEMM). The parameter is introduced in the disorder exponent to allow a transition to the C -dependence found by Bässler of $\mu(F=0) = \mu_0 e^{-\frac{4}{9}\sigma^2}$.

In the following I assess the generalized effective medium model (GEMM) for the calculation of charge carrier mobilities in bulk disordered organic semiconductors. In the first step I test the GEMM model by comparing its results with experimental and kMC results for the hole conducting material N,N' -bis(1-naphthyl)- N,N' -diphenyl-1,1'-biphenyl-4,4'-diamine (α -NPD). I then investigate the disorder dependence of mobilities predicted by the GEMM by comparing mobilities for amorphous and idealized cubic systems with kMC calculations.

The microscopic parameters in eq.4.3.1 are calculated using the Quantum Patch[58] method as described in 2.3. The average number of neighbors is $M = 17.5$ resulting from a nearest atom cutoff between a given pair of molecules of 0.7nm, roughly twice the distance of α II-II stack.

The resulting temperature dependence of the α -NPD zero field mobilities is shown in Fig. 4.3.1, together with the experimental data[98, 99, 100], and the kMC data from the previous chapter. The mobility resulting from the GEMM is shown for three different C -factors: (a) the effective medium assumption with $C=0.25$, (b) the best fit to kMC with $C=0.33$, and (c) Bässler's value of 0.44 (Eq. 2.4.3). While the C -factor of the effective medium assumption already yields a very reasonable estimate, the C -factor of 0.44, which Bässler obtained for the limit of zero charge concentration in a simple cubic lattice with minimal coordination predicts a too steep temperature dependence. The kMC results predict a steeper temperature dependence of the mobility than the GEMM model, reflecting that the percolative nature of charge transport is not fully taken into account by the GEMM model. Although the GEMM model weights contributions from hopping rates between two molecules by the occupation probability of the involved molecules, it averages over the entire system.

In the previous chapter it was shown that the smaller the part of the system where the transport occurs, the higher the disorder. As the GEMM does not reflect this explicitly I will compare GEMM mobilities at different disorder strength with mobilities obtained from kMC calculations. Prior transport simulations on regular lattices have shown that the percolation transport can be captured by adjusting the C -factor depending on the details of the lattice coordination and energy correlation effects [52, 101, 102, 103]. As the coordination in the amorphous system is not well defined, I calculated GEMM mobilities with C -factors varying between 0.25 and 0.44. To assess the effect of the connectivity, I also calculated kMC and GEMM mobilities for simple cubic lattices with coordination of 6 and varying disorder. The kMC calculations on cubic lattices use Marcus rates as defined in Eq. 2.2.5, where the hopping matrix elements are parameterized as

$$J_{if}^2 = e^{-2\alpha R_{if}}, \quad (4.3.2)$$

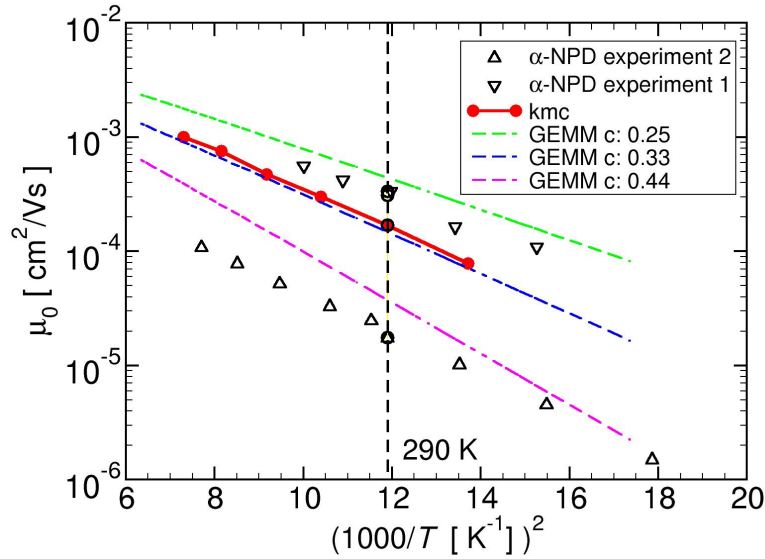


Figure 4.3.1: Temperature dependence of zero-field hole mobilities of α -NPD for the GEMM calculations with different C-factors (dashed lines), kMC-calculations and experimental data [98, 99, 100]. The upper limit corresponds to an effective medium assumption. The low limit was calculated by Bässler for the zero charge concentration limit and a neighbor coordination of 6 as in a simple cubic lattice.

where R_{if} is the distance of two sites in the lattice and $2\alpha = 10/a$ where $a=1\text{nm}$ is the lattice constant of the simple cubic lattice. The size of the cubic lattice is $60 \times 60 \times 60 \text{ nm}^3$. Charge concentration in all kMC calculation is set to 2×10^{-4} holes/molecule, a typical value for organic semiconductors, which yielded very good agreement between experimental and kMC α -NPD mobilities in the previous section 4.1.

Fig. 4.3.2 a) shows the hole mobilities for α -NPD with varying sigma, calculated with kMC and the GEMM model. With higher disorder, the dependence of the GEMM mobilities on the C-factor grows. For all disorder values between $\sigma=1k_B T$ and $\sigma=6k_B T$, a C-factor of around 0.3 yields the best agreement with kMC calculations. It is not clear whether variations in the C-factor are due to the noise of the kMC calculations and the resulting uncertainty of the extrapolation to the zero field mobilities or systematic.

It is surprising that larger disorder does not require a higher C-factor in the GEMM model to match kMC results. I assert this to two reasons. For one, these calculations are done at finite and constant charge carrier concentrations, resulting in the filling of outlying tail states in the kMC calculations. The tail states yield the biggest contribution to the Boltzmann weighted average in the GEMM model and would in the limit of zero carriers strongly reduce mobility, at finite charge densities however, a single hole neutralizes the trap out of the picture by filling it. The second reason for the small and not increasing C-factor is the high coordination of α -NPD compared with nearest neighbor simple cubic lattice systems investigated in other studies. Comparing the α -NPD mobility C-factor dependence with the C-factor dependence of the simple cubic lattice shown in Fig. 4.3.2 b), it can be seen that the GEMM indeed requires larger C-factors to match the kMC-

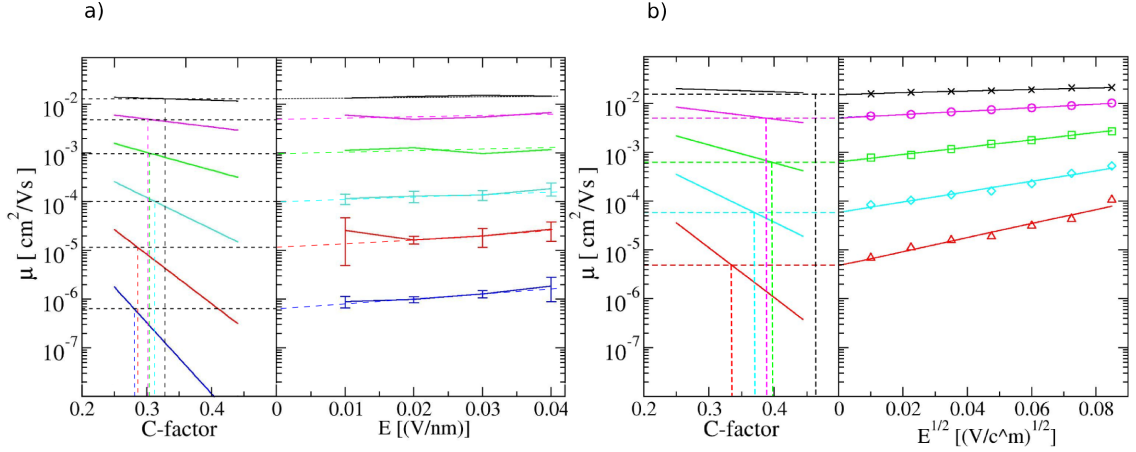


Figure 4.3.2: a) Left: Zero field mobilities of α -NPD in the GEMM for varying disorder strength $\beta\sigma$ from $1 k_B T$ to $6 k_B T$ and C-factor varying between $C = 0.25$ and 0.44 ; the dashed lines represent the Kinetic Monte Carlo (KMC) extrapolation to zero field mobility. Right: The corresponding kMC calculations. b) Same plot as in a) for a simple cubic lattice with transfer integrals as defined in 4.3.2, a coordination of 6 and disorder varying from $1 k_B T$ to $5 k_B T$.

mobilities of the cubic system with a coordination of 6 .

To investigate the influence of coordination on the GEMM model, I systematically increase the connectivity M of the cubic lattice by partitioning the system in the nearest-neighbor (further abbreviated as n-n), the second n-n, and the third n-n shells. For the first n-n (6 sites) shell a connectivity of 6 is given by the six equal transfer integrals $J_{if}^{1n} = e^{-\alpha R_{if}}$, whereas, at the same time, in the second n-n shell (sites 7 to 18) and the third n-n shell (sites 19 to 26) the transfer integrals are set to $J_{if}^{2n} = J_{if}^{3n} = 0$. To gradually increase the connectivity from the first n-n shell to the second $M = 6$ to $(6 < M \leq 18)$ without randomly introducing transfer integrals in the SC topology, we increase the transfer integrals in the second n-n shell according to $J_{if}^{2n} = J_{if}^{1n}(M - 6)/12$, keeping $J_{if}^{3n} = 0$ in the third. This effectively corresponds to M connections/hopping channels with a transfer integral of J_{if}^{1n} . The former equivalence is valid if the external electric field in the kMC simulations is applied along the z axis of the SC lattice such that the potential drop due to the field as well as the hopping distance in the field direction is identical for all 26 sites. Similarly, when further extending the connectivity to the third n-n shell ($18 < M \leq 26$) we additionally set all J_{if}^{3n} to $J_{if}^{3n} = J_{if}^{1n}(M - 18)/8$.

In Fig. 4.3.3 the ratio of GEMM and KMC mobilities for an SC lattice with HOMO disorder of $\sigma = 5k_B T$ is presented for progressively increasing connectivity to next-nearest and next-next-nearest neighbors. The increase of connectivity leads to a better agreement of the GEMM model with the kMC calculations at a lower C-factor, suggesting that the lower C-factor of the α -NPD calculations compared to the lattice system originates from a higher connectivity. This is physically intuitive as an increase of the number of connections in the lattice will increase the number of pairs with potentially lower energy difference, thus reducing the effect of energy disorder.

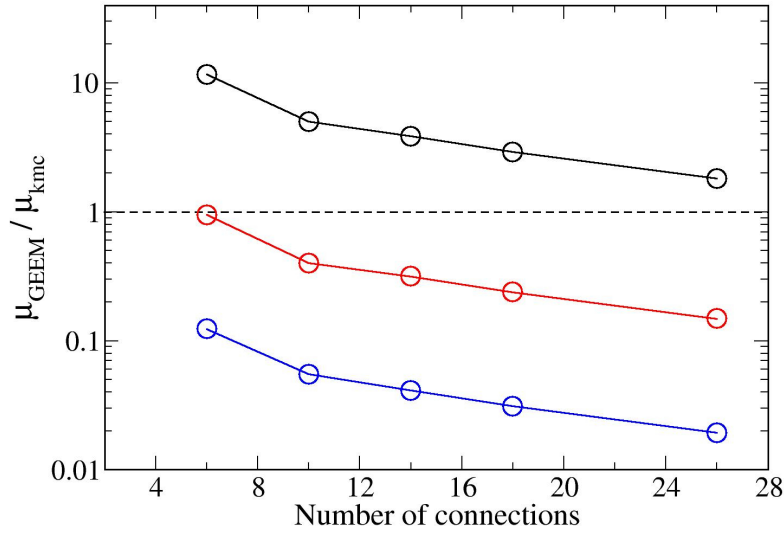


Figure 4.3.3: Ratio of zero-field mobilities obtained from GEMM and kMC for an simple cubic lattice with disorder strength of $\beta\sigma=5$ as function of the number of connections (for each hopping site) for three values of C [0.25 (black), 0.36 (red), and 0.44 (blue)]. As indicated by the dashed line, with an increased number of connections the effective medium estimate $C=0.25$ increasingly agrees with the KMC results. The opposite trend is observed for $C=0.36$ and 0.44 where the discrepancy increases. (Image source: [35])

In conclusion we have seen, that the GEMM model requires an adjustment of the C -factor to reproduce mobilities calculated with kMC as the energy disorder of the materials changes. Materials with a high connectivity require a lower C -factor as the effective energy disorder is reduced by an increase of potential hopping targets. The general order of mobility magnitude of α -NPD is however predicted well for all disorder strength between $1k_B T-6k_B T$.

Chapter 5

Charge transport in guest-host systems

In previous chapters, charge transport in disordered materials was described as a result of thermally assisted hopping between states which are localized on the individual molecules. Using this picture I reproduced experimental mobilities of the hole transport material α -NPD well.

It has however, not been established to what degree this view is sufficient to describe charge transport in all types of disordered organic semiconductors. Studies of charge transport in one dimensional molecular systems comprising a higher energy “bridge” state separating two states with lower energy, suggest that transport to a distant neighbor via the coherent process of “superexchange” might also be relevant in other types of systems [104, 105, 106]. In this picture the carrier resides virtually on the intermediate bridge state.

The formation of conduction and valence bands by superexchange mediated coupling between spatially separated acceptors(donors) bridged by the non-covalently linked donors(acceptors) has been predicted for organic donor-acceptor co-crystals, where it leads to a mirror symmetry of conduction and valence bands with remarkably small effective masses of electrons and holes. [107, 108, 109]. In the following chapter I demonstrate that superexchange coupling can also contribute significantly to the charge carrier mobility of disordered organic semiconductors with deep traps.

The possible role of superexchange is not a priori clear considering the energy disorder in and the usually small coupling between molecules in disordered organic semiconductors. For this study I focus on OSC materials which by design show a suppression of direct hopping rates, due to presence of badly connected trap molecules. I in particular investigate materials used in the emissive layer (EML) of phosphorescent OLEDs, and show that including transport via superexchange is highly relevant to quantitative analyses of their performance.

Light emission layers of state-of-the-art OLEDs consist of a mixture of a small concentration (typically 3-10 mol%) of phosphorescent emissive dye molecules (guests), embedded in a host matrix of a charge transport material. To reduce energy transfer of long lived triplet states from dyes to charges in the host material, energy levels of the constituents are chosen such that the guest molecules act as exciton trapping sites[110]. The smaller

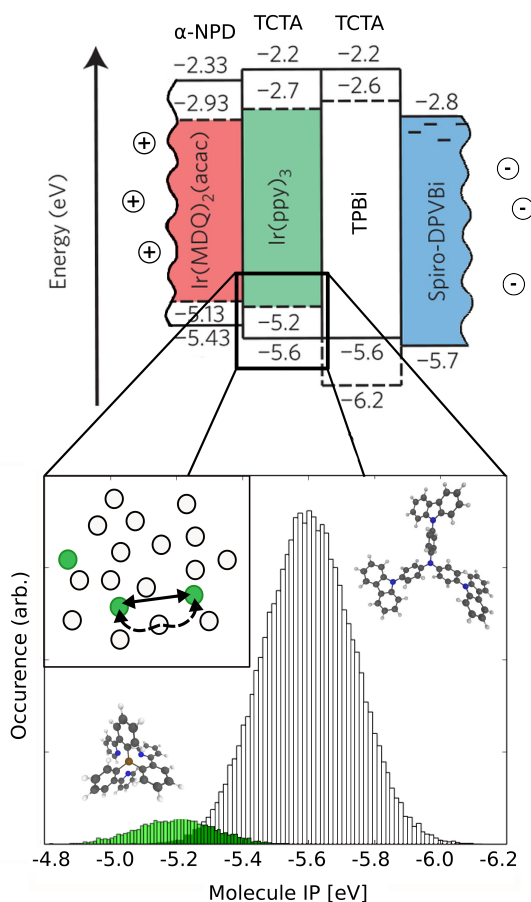


Figure 5.0.1: Top: Stack layout of a white OLED [34]: Red and green guest-host layers emit light of the respective color. Electrons enter from the right, holes from the left. Bottom: Distribution of the ionization potential of molecules in the green emission layer consisting of 8% Ir(ppy)₃ (green) in TCTA host matrix (white). The inset demonstrates the spatial separation of Ir(ppy)₃ molecules in the matrix.

HOMO-LUMO gap of the dye means, that they often also act as charge trapping sites. As charges are more likely to dwell on the trapping dye molecules, recombination of electron-hole pairs is more likely to happen on the dyes, which allows to engineer where excitons are created in the system [111].

This suppression of charge mobility is confirmed by experimental studies [112] and predicted in idealized transport models [113]. The strongest mobility suppression is seen for dye concentrations which are low enough, such that there are not enough guests to form a transport network, but so high that virtually all free charges are trapped. I find that molecular superexchange, which provides a second pathway for guest-guest transport, can strongly enhance carrier mobility at the dye concentrations in the regime described above.

If we consider the density of states of green emission layer of the OLED stack shown in fig. 5.0.1, it can indeed be seen that hole transport states of the green emitter $Ir(ppy)_3$ lie considerably lower in energy than the states of the host molecule TCTA.

In systems like this, where direct hopping rates are repressed due to charge trapping, higher order processes may become relevant.

Direct hopping out of a charge trap is suppressed by the energy penalty of the Marcus equation. It might however be possible to hop to another trap by bridging the distance between the traps with a transition through virtual states on molecules in between, as schematically depicted in fig. 5.0.2 a).

This process is again described as a thermally activated hop from the trap A to the trap B and its rate as such given by the Marcus rate equation.

$$\omega_{AC} = \frac{2\pi}{\hbar} |H_{AC}|^2 \frac{1}{\sqrt{4\pi\lambda_{AC}k_B T}} \exp\left(-\frac{(\lambda + \Delta E_{AC})^2}{4\lambda_{AC}k_B T}\right) \quad (5.0.1)$$

Where the electronic coupling between final state on molecule C and initial state on molecule A is can be calculated form 1st order perturbation theory. [114, 115]

$$H_{AC} \cong H_{AC,0} + \sum_{i=1}^N \frac{H_{AB_i,0} H_{B_i C,0}}{\Delta E_{AB_i C}} \quad (5.0.2)$$

with $H_{XY,0}$ the direct transfer integrals between molecules X and Y, and B_i intermediate molecules. ΔE_{ABC} is the vertical energy difference between the virtual state on molecule B_i and the transition state of the AC charge transfer (see fig. 5.0.2 b)). As the transition state geometry is not known, we can use the formalism of the Marcus theory to derive an expression for the energy difference ΔE_{ABC} . For this we separate ΔE_{ABC} in three contributions:

$$\Delta E_{ABC} = \Delta E_{\text{rel}} - \Delta E^* + \Delta E_2^* \quad (5.0.3)$$

The first contribution E_{rel} is the energy difference of the charged ground state of the initial and bridge molecule. The other contributions can be derived using the assumption that the conformational reorganization is harmonic. , it is possible to calculate the contributions ΔE^* and ΔE_2^* , resulting in the expression for ΔE_{ABC} :

$$\Delta E_{ABC} = E_{B,0} - \frac{E_{A,0} + E_{C,0}}{2} + \frac{\lambda_B}{2} \quad (5.0.4)$$

A derivation of this expression is shown in section 5.1 and can also be found in the PHD thesis of my roommate Pascal Friederich [116]. In principle, the super-exchange coupling from 5.0.2 is reduced by a factor of $J/\Delta E$ compared to a non-super-exchange coupling. Typical couplings are in the order of $1 \cdot 10^{-3}$ eV, whereas typical energy differences are in the order of 0.1 – 0.4eV, leading to a reduction in coupling of $1 \cdot 10^2$ and a reduction of the rate by a factor of $1 \cdot 10^4$.

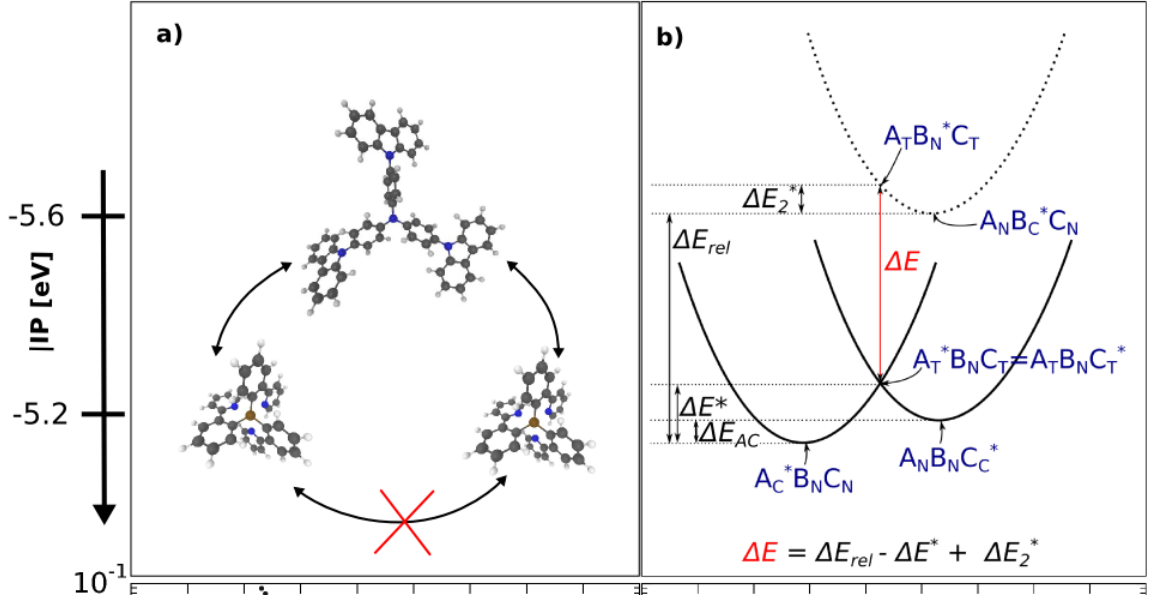


Figure 5.0.2: (a) Schematic illustration of hole transport between Ir(ppy)₃ molecules. The transfer integral of a direct guest-guest hop is negligible due to the large distance between the guest molecules, guest-host hops are suppressed by the energy difference in the exponent of the Marcus equation 5.0.1. (b) Guest-guest hop via a virtual host state in the Marcus picture: The reaction coordinate is on the x-axis, energy is on the y-axis. The three parabolas represent initial state (left), final state (right) and transition state (dotted, top). The reaction coordinate of the transition state is different, but is projected into the plane for illustration. A, B and C refer to the state of the host (B) and guest (A,C) molecules. The asterisk indicates the localization of the hole, subscripts indicate the geometry of the state, where N = neutral, C = charged, T = transition. At the cross section of left and right parabola final and initial state are resonant. The energy difference to the state in which B is charged determines the denominator for the superexchange transfer integral bridged by B.

To estimate the general relevance of detrapping due to superexchange-mediated hops, I consider a model system consisting of a bridge molecule B sandwiched between two molecules A and C with lower energy states (see fig. 5.0.3). Let us consider a charge on molecule A, which can leave the molecule either by hopping to molecule C or B. In this model, we assume the same reorganization energy $\lambda = 0.2\text{eV}$ for all molecules, no direct coupling of molecules A and C ($H_{AC,0} = 0$), equal transfer integrals $H_{AB,0} = H_{BC,0} =: H_{gh}$ and states of the same energy on molecule A and C $E_{A,0} = E_{C,0}$.

The ratio of the rate $\omega_{AC,sx}$ of an escape from molecule A by a superexchange-mediated hop from A to C and the rate $\omega_{AB,0}$ of an escape due to a direct hop to molecule B can be calculated as follows [36].

The superexchange coupling between the fully relaxed states on A and C is given by

$$H_{AC} \cong \frac{H_{AB,0}H_{BC,0}}{\Delta E_{ABC}} = \frac{|H_{hg}|^2}{\Delta E_{ABC}} \quad (5.0.5)$$

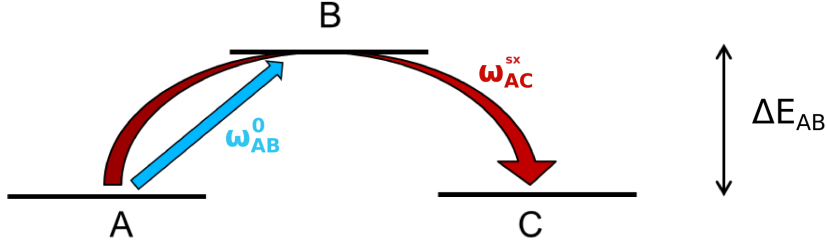


Figure 5.0.3: Model system of three molecules A, B and C. In this system a charge residing on A has two escape routes: a direct hop to molecule B and a hop to C through a virtual state on B. (Image source: SI in [36])

with ΔE_{ABC} taken from eq. 5.0.4

$$\Delta E_{ABC} = E_{B,0} - \frac{E_{A,0} + E_{C,0}}{2} + \frac{\lambda_B}{2} = \Delta E_{tr} + \frac{\lambda}{2} \quad (5.0.6)$$

The Marcus rate for a direct hop from molecule A to B is

$$\omega_{AC} = \frac{2\pi}{\hbar} |H_{AB}|^2 \frac{1}{\sqrt{4\pi\lambda k_B T}} \exp \left[-\frac{(\Delta E_{tr} + \lambda)^2}{4k_B T \lambda} \right] \quad (5.0.7)$$

analogously the rate for superexchange hops from A to C is obtained by inserting eq.5.0.6 in eq. 5.0.1

$$\omega_{AC,sx} = \frac{2\pi}{\hbar} \left(\frac{|H_{hg}|^2}{\Delta E_{tr} + \lambda/2} \right)^2 \frac{1}{\sqrt{4\pi\lambda k_B T}} \exp \left[-\frac{(\Delta E_{tr} + \lambda)^2}{4k_B T \lambda} \right] \quad (5.0.8)$$

the ratio of these rates ("escape rate ratio") is thus given by:

$$\frac{\omega_{AC,sx}}{\omega_{AB,0}} = \left(\frac{H_{hg}}{\Delta E_{tr} + \lambda/2} \right)^2 \exp \left[\frac{(2 + \Delta E_{tr}/\lambda) \Delta E_{tr}}{4k_B T} \right] \quad (5.0.9)$$

In fig. 5.0.4 this escape rate ratio is shown as a function of the direct transfer integral H_{hg} and the trap depth ΔE_{tr} . For typical coupling values in OSCs of $H_{hg} \approx 10^{-3}$ eV (compare section 4 and section 5.3), the figure shows a significant increase of the escape rate by a superexchange-mediated hop if trap depth ΔE_{tr} are deeper than 3 eV. In section 5.3 I present kMC calculations for realistic guest host systems, where it can indeed be seen, that superexchange mediated trap-trap hopping becomes a dominant transport mechanism around 0.3-0.4 eV average trap depth.

5.1 Energy denominator

Considering fig.5.0.2 and the expression from 5.0.3

$$\Delta E_{ABC} = \Delta E_{rel} - \Delta E^* + \Delta E_2^* \quad (5.1.1)$$

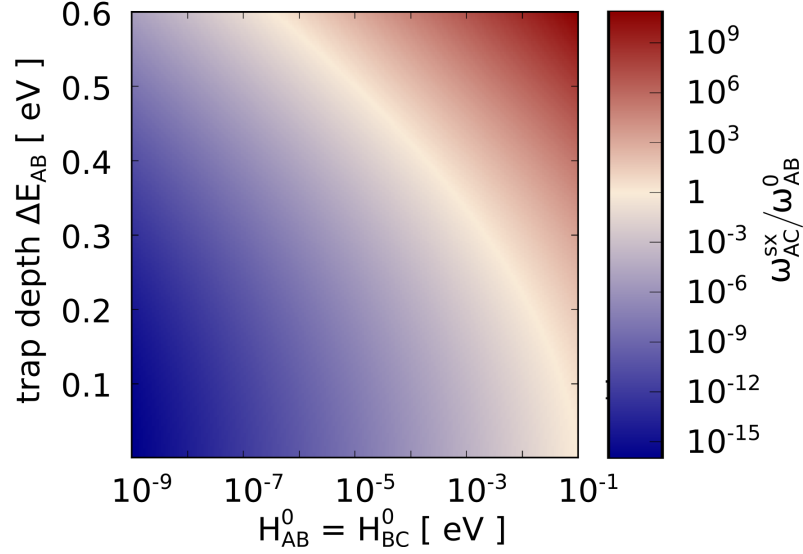


Figure 5.0.4: Ratio between the superexchange hop rate from a trap A to a resonant trap C through a virtual state on host molecule B and the hop rate from a trap A to B, as a function of the host-guest transfer integral H_{hg} and the trap depth ΔE_{tr} .

one has to calculate three components to derive ΔE_{ABC} . The first component is the energy difference between the charged ground state of the bridge molecule and the molecule on which the charge sits initially :

$$\Delta E_{rel} = E(A_N B_C * C_N) - E(A_N^* B_N C_N) = E_B - E_A \quad (5.1.2)$$

where A, B and C label the state of the three molecules. The lower indices describe the conformational state where N stands for the neutral conformation, C for the charged conformation and T for the conformation in the transition state. A star denotes whether a molecule is charged.

The transition state energy ΔE^* of Marcus theory can be calculated [48] under the assumption that the potential energy of a molecular conformation change along the discharging reaction coordinate can be approximated as a harmonic. The intersection of the discharging parabola of molecules A and C yields:

$$\Delta E^* = E(A_T^* B_N C_T) - E(A_C^* B_N C_N) = (E(A_T^* C_T) - E(A_C^* C_N)) = \frac{1}{4\lambda_{AC}} (\Delta E_{AC} + \lambda_{AC})^2 \quad (5.1.3)$$

For the estimation of ΔE_2^* , a single-molecule picture as shown in fig.5.1.1 is helpful. If we assume that the charged and uncharged potential energy surfaces of molecules A and C have the same curvature, we can split ΔE_2^* in two contributions:

$$\Delta E_2^* = E(A_T B_N^* C_T) - E(A_N B_C^* C_N) = E(A_T C_T) - E(A_N C_N) + \frac{\lambda_B}{2} \quad (5.1.4)$$

Where we use that $E(ABC) = E(A) + E(B) + E(C)$. The second term then follows from the definition of the reorganization energy from 2:

$$\frac{\lambda_B}{2} = E(B_N^*) - E(B_C^*) \quad (5.1.5)$$

We can now distribute $E(A_T C_T) - E(A_N C_N)$ in single molecule contributions and again use Marcus theory to obtain:

$$E(A_T) - E(A_N) = \frac{1}{2} \Delta E_{31}^* = \frac{1}{2} \frac{1}{4\lambda_{CA}} (\Delta E_{CA} + \lambda_{CA})^2 \quad (5.1.6)$$

$$E(C_T) - E(C_N) = \frac{1}{2} \Delta E_{13}^* = \frac{1}{2} \frac{1}{4\lambda_{AC}} (\Delta E_{AC} + \lambda_{AC})^2 \quad (5.1.7)$$

using equivalent expression to eq. 5.1.3 to combining the results yields:

$$\Delta E_{ABC} = E_{B,0} - \frac{E_{A,0} + E_{C,0}}{2} + \frac{\lambda_B}{2} \quad (5.1.8)$$

This expression is very intuitive as it is the energy difference between the energy of the charged bridge molecule and the mean energy of final and initial molecule.

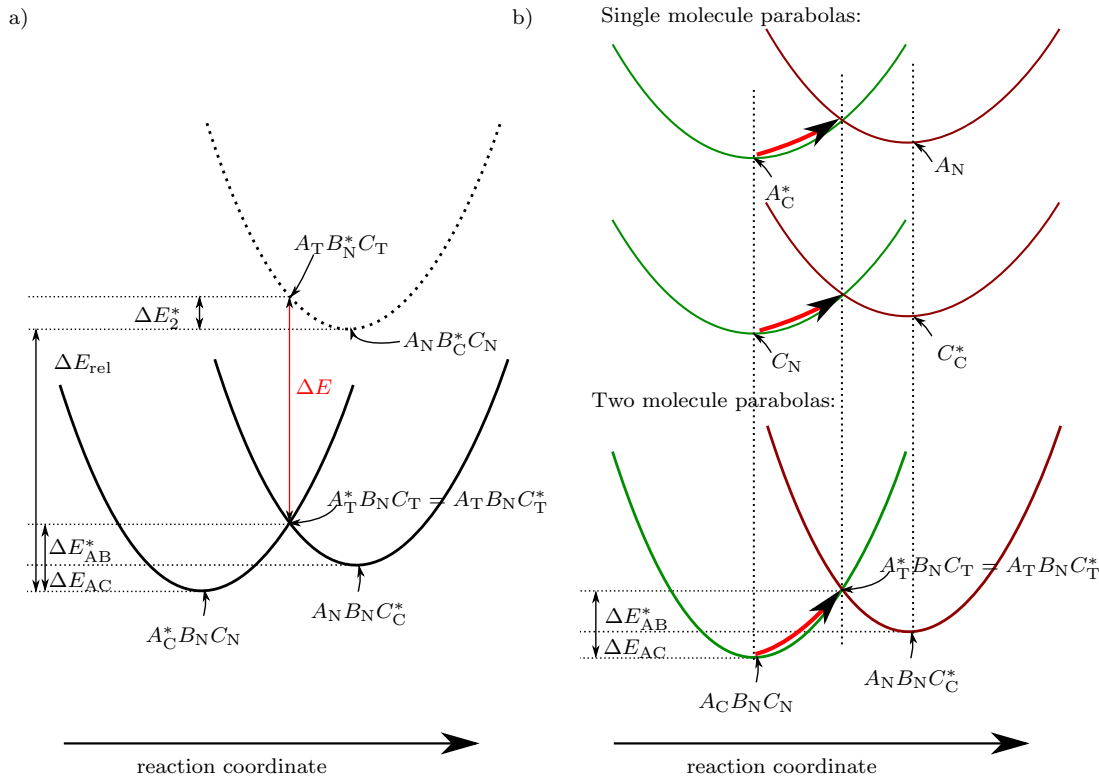


Figure 5.1.1: a) Marcus parabola illustrating contributions to ΔE_{ABC} . b) Deconstruction of the two-molecule parabola of the charge transfer process from molecule A to molecule C to two one-molecule parabolas. B remains in a neutral geometry. (Image source: [116])

5.2 Calculation of superexchange coupling in mesoscopic morphologies

To perform kinetic Monte-Carlo calculations, superexchange transfer integrals given by eq. 5.0.2 have to be calculated for connections between $O(10^6)$ molecules.

Direct transfer integrals and the on-site energies are calculated using the stochastic method described in chapter 3.3.

As it is impossible to calculate all $O(10^{18})$ superexchange transfer integrals in the system, I employ the following scheme to obtain all significant superexchange transfer integrals connecting a site i to other sites. First, the N largest direct transfer integrals J_{ji} connecting site i to other sites j are determined. For every site j the N largest direct transfer integrals J_{kj} connecting every site j to other sites k are chosen. For all N^2 pairs (i, k) the superexchange transfer integral is then calculated according to eq. 5.0.2. N is chosen such that all non-negligible direct transfer integrals are included in the calculation of the superexchange transfer integrals. This scheme reduces the number of pairs from $O(10^{18})$ to $O(10^6 \cdot N^2)$, where N is between 10-20.

5.3 Superexchange in guest-host systems

In this section I quantify the hole transport in two prototypical host-guest systems frequently used in OLEDs: $\alpha - NPD : Ir(MDQ)_2(acac)$ (α -N,N'-di(1-naphthyl)-N,N'-diphenyl-(1,1'-biphenyl)-4,4'-di-amine) with the red-emitting dye bis(2-methylbenzo[f,h]quinoxaline)(acetylacetonate) iridium(III)), and $TCTA : Ir(ppy)_3$ (tris(4-carbazoyl-9-ylphenyl) amine) with the green-emitting dye tris[2-phenylpyridinato-C2,N] iridium(III)]. These materials are used as the red- and green-emitting layers in OLEDs [34], (see fig. 5.3.1 for the chemical structure of the molecules).

Atomistic morphologies of the host-guest systems containing 1000 molecules per morphology and a guest concentration of 8 mol% have been generated for both $\alpha - NPD : Ir(MDQ)_2(acac)$ and $TCTA : Ir(ppy)_3$ using the Monte Carlo protocol described in chp. 2.

I find a mass density of about 0.87 g/cm^3 for both systems. The pair distribution function of $\alpha - NPD : Ir(MDQ)_2(acac)$ and $TCTA : Ir(ppy)_3$ for 8 mol% guest concentration are shown in 5.3.2. For $\alpha - NPD : Ir(MDQ)_2(acac)$ (left) two peaks at 0.5 nm and 1.25 nm can be seen, reflecting stacking of the $\alpha - NPD$ host molecules along the long and short axes. The pair distribution function of $TCTA : Ir(ppy)_3$ (right) does not show peaks, reflecting the isotropy of the host material TCTA.

Molecular ionization potentials, hole transfer integrals and reorganization energies are calculated using the quantum patch method, see chapter 2.

The resulting distributions of ionization potentials of the two materials are a superpositions of the Gaussian distributions of the ionization potentials of the transport and emitter molecules, as shown for the case of a guest concentration of 8 mol% in fig. 5.3.3.

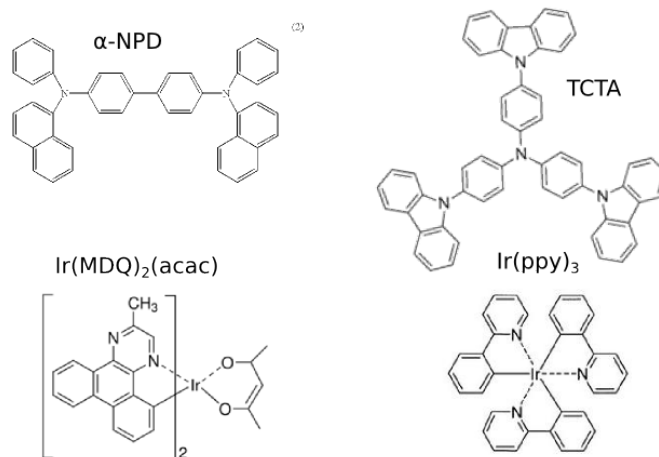


Figure 5.3.1: Chemical structure of the components of the red emission layer α - *NPD* : *Ir(MDQ)₂(acac)* and the green emission layer *TCTA* : *Ir(ppy)₃*. The Ir-complexes are phosphorescent emitters of the respective material, the pure organic molecules act as charge transport material and spacer between emitters.

The Quantum Patch method yields a standard deviation of $\sigma = 0.131$ eV for α - *NPD*, $\sigma = 0.072$ eV for *Ir(MDQ)₂(acac)*, $\sigma = 0.136$ eV for *TCTA* and $\sigma = 0.118$ eV for *Ir(ppy)₃*. For both emission layers, the offset between the two Gaussians is adjusted to reproduce average host and guest ionization potentials of 0.3 eV (0.4 eV) for the α - *NPD* : *Ir(MDQ)₂(acac)* (*TCTA* : *Ir(ppy)₃*) system, as determined from ultraviolet photoelectron spectroscopy measurements [34].

The transfer integrals for direct and superexchange mediated hole hops from emitters to surrounding molecules are presented in fig. 5.3.4. At small distances between emitter and target molecules, the direct transfer-integrals are dominant. However, for distances above approximately 2 nm the superexchange transfer integrals are orders of magnitude larger than the direct transfer integrals.

The stochastic methods described in chp.3.3 were employed to generate morphologies, transfer-integrals and ionisation potentials for $67 \times 67 \times 67$ nm³ sized bulk samples of the materials.

Hole mobilities of these samples were then calculated by kinetic Monte-Carlo transport simulations, assuming periodic boundary conditions and a constant hole density of 2×10^{-4} holes/molecule). Simulations are performed with and without including superexchange transfer integrals at an applied field of 0.03 V/nm, corresponding to 3V in a 100 nm device.

The hole mobilities (see fig. 5.3.5) show the characteristic mobility minimum at the cross-over between the low concentration regime in which the guest states act as trap sites and the high-concentration regime in which the transport is due to direct emitter-emitter transport. The mobility reduction with increased emitter concentration depends on the trap depth on the emitter, and is much larger for the *TCTA* : *Ir(ppy)₃* system (0.4 eV trap depth) than for the α - *NPD* : *Ir(MDQ)₂(acac)* system (0.3 eV trap depth).

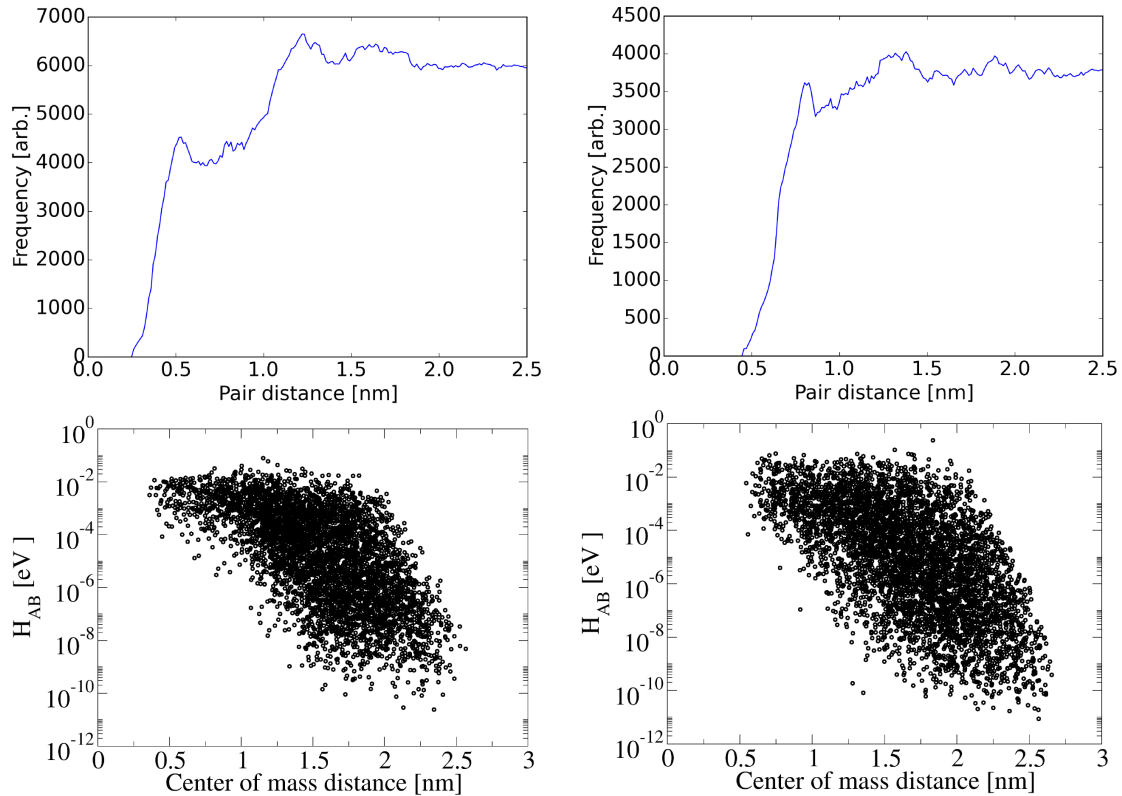


Figure 5.3.2: Top: Pair distribution functions of the morphologies with 8% guest concentration, generated by simulation of vapor deposition. Left: $\alpha - NPD : Ir(MDQ)_2(acac)$, right: $TCTA : Ir(ppy)_3$.

Bottom: Distribution of transfer integrals, as calculated with the quantum patch method[1], Left: $\alpha - NPD : Ir(MDQ)_2(acac)$, right: $TCTA : Ir(ppy)_3$. The anisotropy of $\alpha - NPD$ can be seen both in the pair distribution function and the transfer integrals. (image source: SI in [36])

By including superexchange transfer integrals, hole mobility at room Temperature is increased by up to an order of magnitude in $TCTA:Ir(ppy)_3$ and by a factor of two in $\alpha - NPD : Ir(MDQ)_2(acac)$.

With increasing temperature the mobility enhancing effect due to superexchange decreases, due to the lowering of reduced hopping barriers.

The relevance of superexchange with respect to the choice of the guest concentration is illustrated in Fig. 5.3.5c), which presents the ratio of emitter concentrations of calculations with and without superexchange at which the mobilities are equal. For low concentrations, close to the mobility minimum, up to five times less emitters are required to achieve the same mobility in the presence of superexchange.

In fig. 5.3.5d) the concentration of the guest molecules which minimizes the mobility is presented as a function of temperature. As superexchange coupling improves emitter to emitter hopping, the mobility minima occur at lower emitter concentrations. For $TCTA:Ir(ppy)_3$ the mobility shifts from 9% emitter concentration to 6% at room temperature. It can further be seen, that the temperature dependence of the shift of the mobility

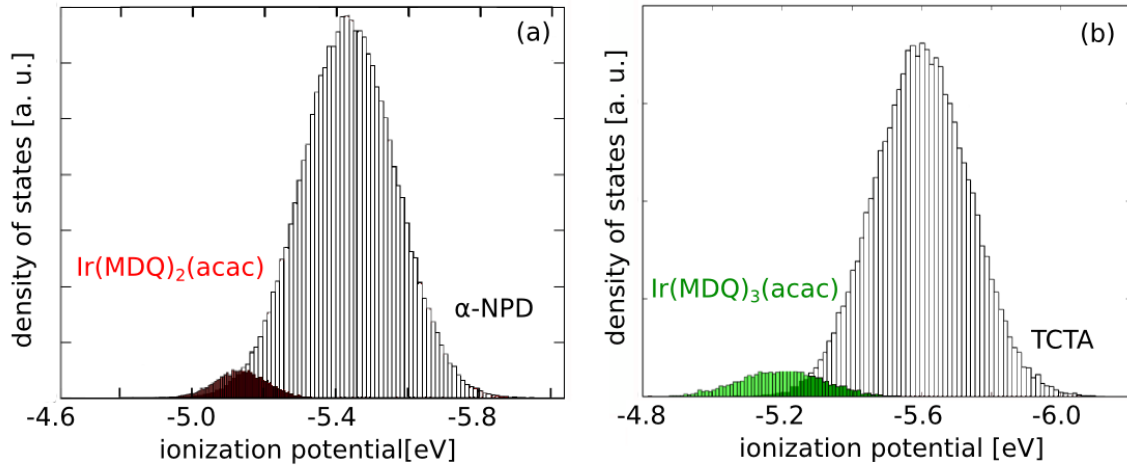


Figure 5.3.3: Distribution of host (white) and emitter (colored) ionization potentials of (a) α -NPD : $\text{Ir}(\text{MDQ})_2(\text{acac})$ (red) and (b) TCTA : $\text{Ir}(\text{ppy})_3$ (green) for emitter concentrations of 8 mol%. (Image source: Si in [36])

minimum is weaker if superexchange hops are allowed, as the improved connectivity of molecules alleviates for the increase in reduced disorder.

To investigate the influence of hole concentration on the role of superexchange in the hole transport, I repeated the room Temperature calculations for an increased hole concentration of 10^{-3} holes per molecule (5 times higher hole concentration). It can be seen in fig.5.3.6, that the increase in carrier density changes the hole mobility by 2 orders of magnitude for TCTA : $\text{Ir}(\text{ppy})_3$ and by a factor of two for α -NPD : $\text{Ir}(\text{MDQ})_2(\text{acac})$. This increase in mobility due to the filling of trap states, which act as bottlenecks in the transport, is well studied for pure disordered materials[52] (it is more severe in the case of TCTA : $\text{Ir}(\text{ppy})_3$). The deeper the trap states in the material the stronger is the charge carrier concentration dependence of the mobility.

It can further be seen in fig.5.3.6, that the increase of hole mobility due to superexchange is independent of the charge carrier concentration for both emissive layers. This hints to the strong percolative nature of the charge transport in these systems. By removing the deepest traps through trap filling, another trap takes over as critical resistor, whose connection to the percolation network is still equally improved by the superexchange mechanism.

Given the exponential dependence of the hopping rate on energy differences, it may seem surprising that superexchange does not have an even stronger effect on the mobility. Bässler [64] already noted that the spread of transfer integral values, has relevant impact on the transport through disordered systems, yet off-diagonal disorder is often not considered in mesoscopic transport models.

To gain more insight into the transport process we calculated the transport energy $T(E)$ at different guest concentration for the TCTA : $\text{Ir}(\text{ppy})_3$ system, i.e. the distribution of ionization potentials of sites which are used for the hole transport.

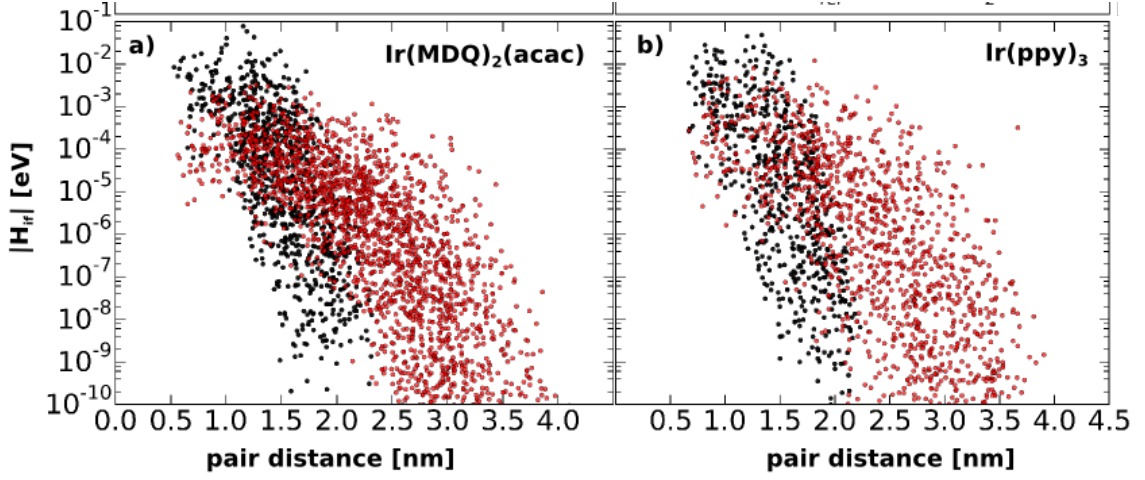


Figure 5.3.4: Direct (black filled circles) and superexchange (red hollow circles) transfer integrals between guest molecules and surrounding molecules (guest and host) as a function of their center of mass distance for (a) $\text{Ir}(\text{MDQ})_2(\text{acac})$ molecules in an $\alpha - \text{NPD}$ host and (b) $\text{TCTA} : \text{Ir}(\text{ppy})_3$ molecules in a TCTA host, for a guest concentration of 8 mol%. (Image source: [36])

For the 85:15 $\text{TCTA} : \text{Ir}(\text{ppy})_3$ system we find a Gaussian distribution centered around 0.75 eV away from the mean host ionization potential (see fig. 5.3.7) and a standard deviation of 0.05 eV. The mean of the transport energy is shifted towards the host ionization potentials with decreasing guest concentration, as there are less guests at lower energies which can be occupied.

Comparing the distance of the transport energy centered around 0.75 eV to the standard deviation of the TCTA ionization potentials ($\sigma = 0.136\text{eV}$), it is clear that charge carriers will most of the time be trapped on emitter-molecules when they travel through the material. A critical quantity to describe the nature of the transport mechanism is then the ratio of guest-host to guest-guest hops, as this describes whether there is a good percolation network between the emitters or whether a hole has to hop to a TCTA molecule before it falls to the next emitter.

To calculate this rate, I start by calculating the probability of a hole which is localized on an emitter to hop to another emitter, depending on the ionization potential of the initial emitter molecule, for all emitter molecules in a 05:95 $\text{TCTA} : \text{Ir}(\text{ppy})_3$ system at 275 Kelvin.

The probability for a hole on a emitter i to hop on another emitter is calculated as

$$P_i^{\text{emitter-emitter}} = \frac{\sum_j \omega_{ij}}{\sum_k \omega_{ik}} =: P_i^{\text{guest-guest}} \quad (5.3.1)$$

where j are $\text{Ir}(\text{ppy})_3$ molecules coupled to molecule i and k TCTA molecules coupled to molecule i , where the rates are assessed for a hole concentration $\rightarrow 0$.

$P_i^{\text{emitter-emitter}}$ and average energy dependent emitter-emitter hopping probabilities $p(E)^{\text{guest-guest}}$ are shown in fig. 5.3.8. In order to decouple the spread of electronic couplings H_{AB} from the exponential energy penalty contributing to the Marcus rates for

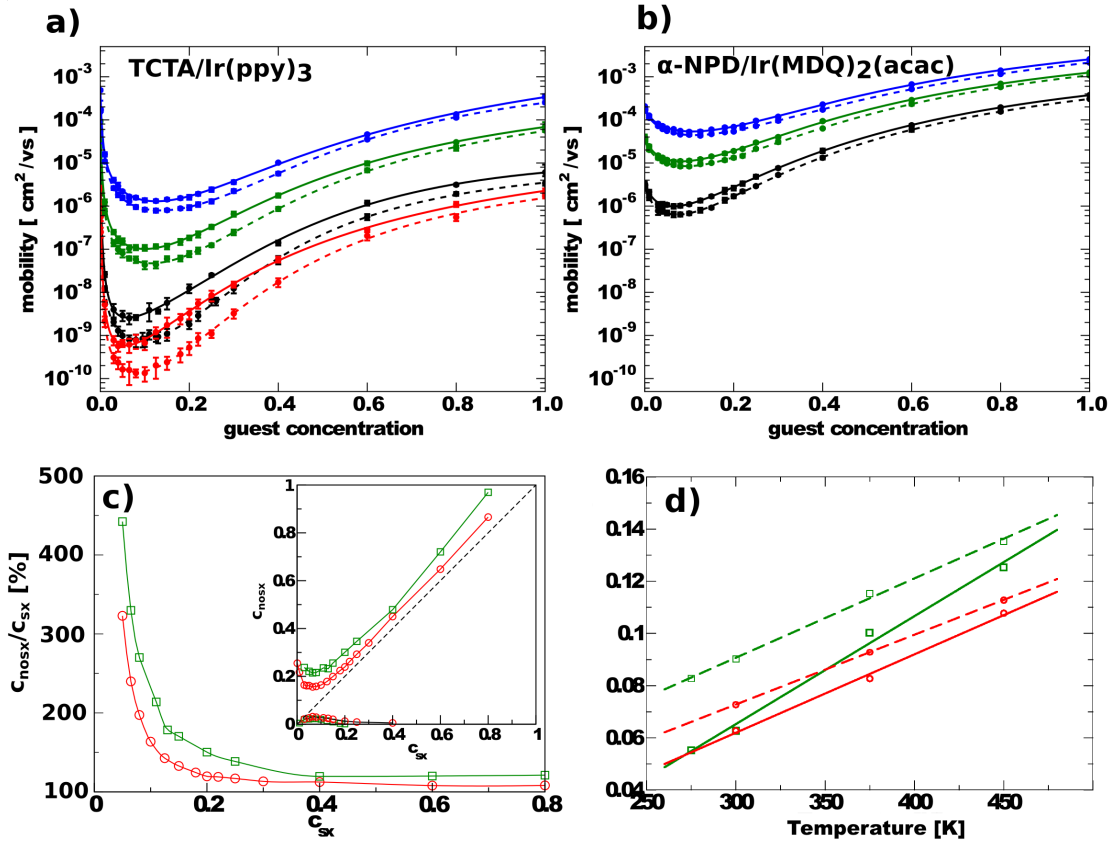


Figure 5.3.5: Temperature and Guest concentration dependence of the hole mobility of (a) $TCTA : Ir(ppy)_3$ and (b) $\alpha - NPD : Ir(MDQ)_2(acac)$ bulk systems at a field of 0.03 V/nm and a hole concentration of 2.0×10^{-4} holes/molecule. Dashed lines: only direct hops in the transport model. Solid lines: direct and superexchange hops in the transport model. The different colors indicate results for different Temperatures 275 K (red), 300K (black), 375 K (green) and 450K (blue). (c) Ratio between the emitter concentrations of the cases with direct and direct+superexchange hops at which the mobility is equal (green: $TCTA : Ir(ppy)_3$, red: $\alpha - NPD : Ir(MDQ)_2(acac)$) at 300K. The direct vs. direct+superexchange concentrations that yield the same mobility are presented in the inset. (d) Guest-concentrations at which the hole-mobility is minimal as a function of temperature.

further analysis of $P_i^{emitter-emitter}$, I compare two models, one with constant H_{AB} , fig.5.3.8 right panels, and one with real spread of H_{AB} , left panels, which cover a range of 10 orders of magnitude (compare fig. 5.3.4). Both models have the same mean value of H_{AB} and use the energy dependence of the Marcus rate.

In all cases we see that, the higher the ionization potentials at the starting site, the higher the emitter-emitter hopping probabilities, as the ionization potentials move farther away from the TCTA ionization potentials.

The top panels show the rates including only direct hops, whereas the lower panels show the rates including superexchange contributions. Both models account for the exponential dampening caused by energy disorder via the Marcus rate equation.

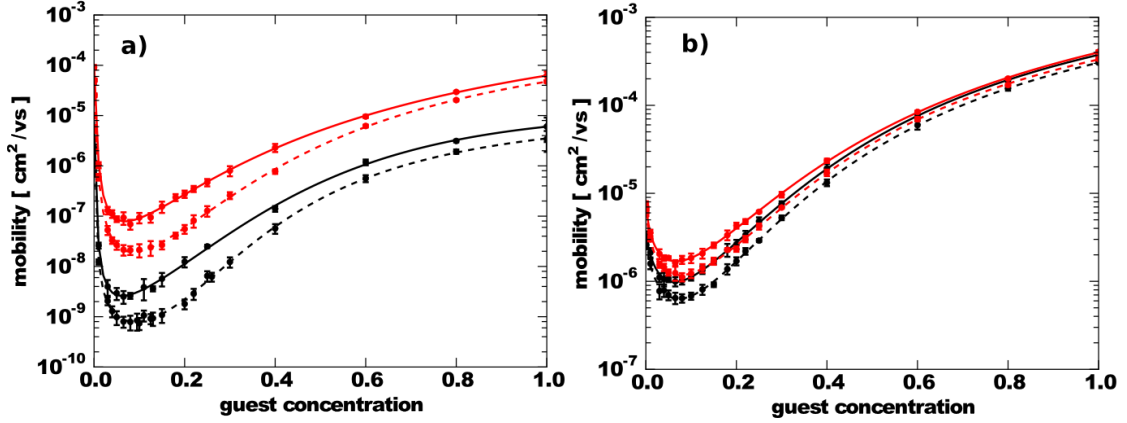


Figure 5.3.6: Guest and hole concentration dependence of the hole mobility of $TCTA : Ir(ppy)_3$ (a) and $\alpha - NPD : Ir(MDQ)_2(acac)$ (b) bulk systems at a given Temperature of 300 K and a field of 0.03 V/nm. Dashed lines show mobilities from calculations neglecting second order couplings in the Marcus rates, full lines show mobilities taking second order hops into account. (Image source: SI in [36])

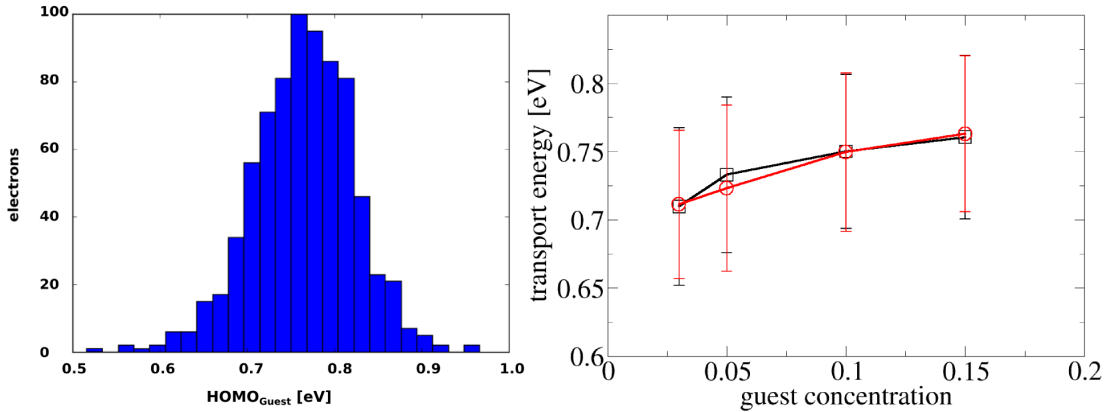


Figure 5.3.7: Left: Transport energy $T(E)$ of the 15% doped $TCTA/Ir(ppy)_3$ system at 275 K. Right: Mean and standard deviation of transport energy depending on the guest concentration. There is no difference in transport energies of the KMC calculations with (red) and without (black) superexchange. (Image source: SI in [36])

In the lowest row of fig.5.3.8, the dependence of the average $Ir(ppy)_3-Ir(ppy)_3$ hopping probabilities on the $Ir(ppy)_3$ concentration is shown including and excluding superexchange.

In order to finally obtain the contribution of emitter-emitter hops to transport, I integrate the emitter-emitter hopping probabilities $p(E)^{guest-guest}$ with the probability that a given emitter is occupied $T(E)$, as obtained from the kMC calculations (shown in 5.3.7).

$$P_{guest-guest} = \int dE p(E)^{guest-guest} T(E) \quad (5.3.2)$$

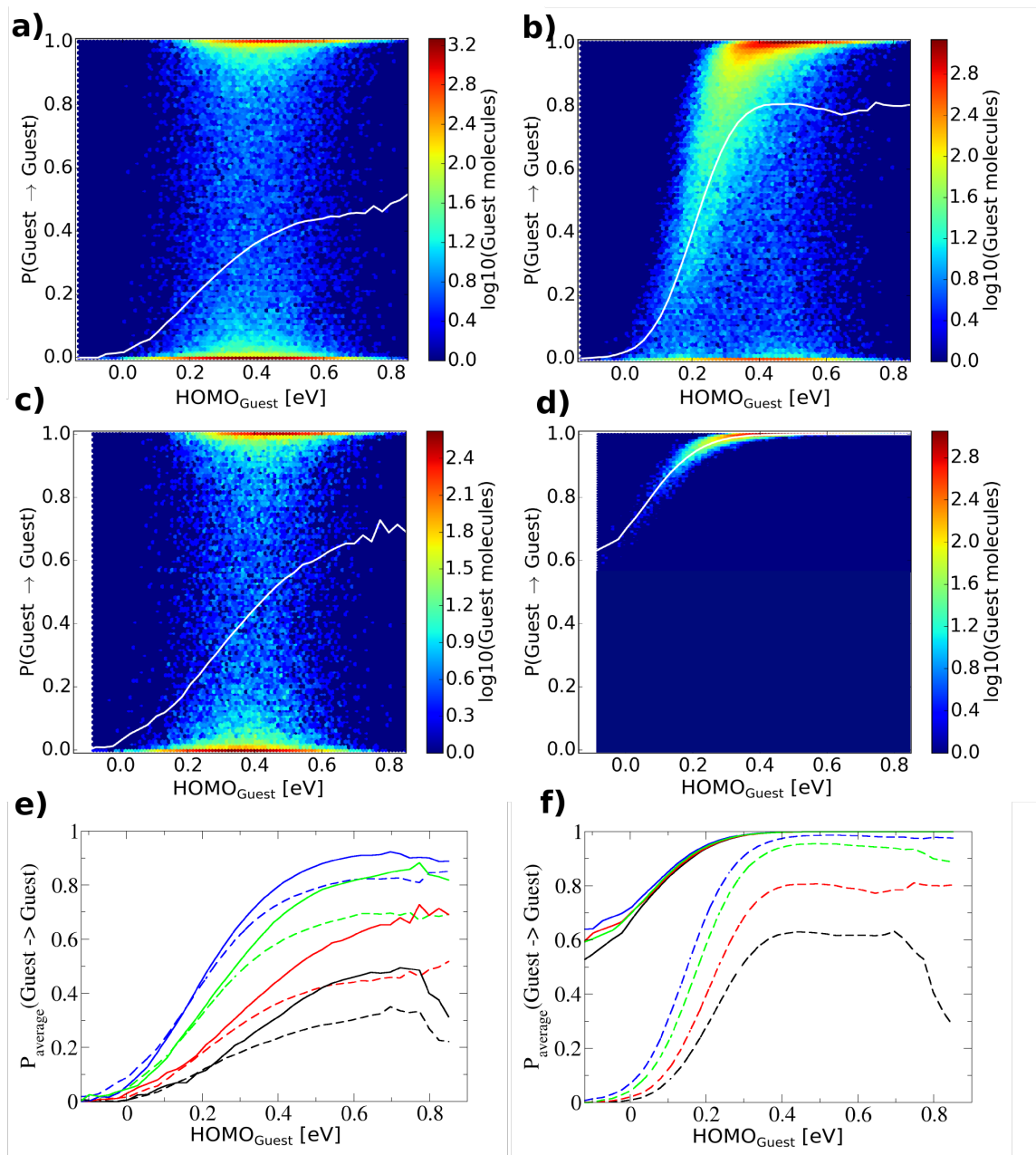


Figure 5.3.8: Probability for a hole localized on a guest(emitter) site to jump to another guest site in a TCTA/Ir(ppy)₃ 95:05 host-guest system at 275K. The x-axis is the ionization potential of the emitter molecules relative to the average TCTA ionization potential. The white lines show the average probability for guest-guest hopping at the given emitter ionization potential. a) Guest-guest probabilities with full Marcus rates, direct hopping only. b) Guest-guest hopping probabilities with Marcus rates which all use the same average transfer integral, direct hopping only. c) the same as in a) but with inclusion of superexchange, d) the same as in b) but with inclusion of superexchange.

The difference between c) and d) indicates that the disorder of the transfer integrals diminishes the impact of superexchange on guest-guest hopping probability of the system.

e) and f) show the average probability for guest-guest hopping for host:guest ratios of 97:03 (black), 95:05 (red), 90:10 (green) and 85:15 (blue) including superexchange (full lines) and excluding superexchange (dashed lines). In e) the probabilities are shown for the realistic spread of transfer integrals, in f) for the averaged transfer integrals. (Image source: SI in [36])

The resulting probabilities shown in fig. 5.3.9 illustrate that the inclusion of the superexchange processes results in a strong increase of guest-guest hopping probabilities for the model with constant transfer-integrals (essentially to 100% even at low guest concentrations), but a more moderate impact in the presence of off-diagonal disorder.

This difference results from the fact that the number of accessible host molecules rises faster with the hopping radius than the number of accessible guest molecules. Since the hopping matrix elements to either guest or host molecules are distributed over many orders of magnitude, the probability for a strongly connected host molecule is larger in the model with the spread transfer integrals.

In many mesoscopic transport models the spread of transfer-integrals is not considered. In these models, the importance of superexchange would be overestimated considerably.

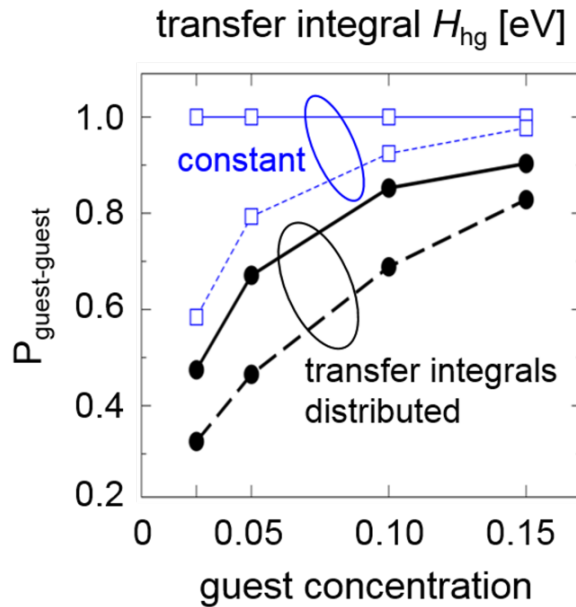


Figure 5.3.9: Guest concentration dependence of the probability of guest-guest hopping for equilibrated holes in $TCTA : Ir(ppy)_3$ at 275 K with a hole concentration of 2.0×10^{-4} per molecule, in a model employing the calculated distribution of the transfer integrals (black discs) and using constant transfer integrals with the same average as the quantum chemically calculated transfer integrals (blue squares). Dashed lines show the guest-guest hopping probabilities neglecting superexchange contributions to the transfer integrals, full lines include superexchange. (Image source: [36])

Summary In this chapter hole transport in OSC materials consisting of mixed species of molecules has been investigated. As the minority component in such systems can act as a deep charge trap, I have investigated the second order effect of intermolecular superexchange as a possible detrapping mechanism [36].

A charge hopping from a molecule A to a molecule C thereby hops through a virtual state on an intermediate molecule B. In the context of Marcus theory, a formalism to describe this as an activated process was introduced.

Applying this formalism to calculate hole transport in typical emission layers present

in OLEDs, I have shown, that superexchange can boost mobilities by up to an order of magnitude at room Temperature. Improved emitter-emitter percolation due to superexchange can shift the mobility minimum to considerably lower guest concentrations when compared to models which consider only direct hops between molecules.

The relevance of superexchange crucially depends on the energy difference between the average on-site hole energy of guest and host molecules: it plays an increasingly important role in host-guest systems for which this energy difference is large.

The quantitative impact of superexchange is strongly affected by the disorder of transfer integrals and therefore cannot be properly described with lattice models that neglect the distance dependence and distribution of the hopping matrix elements.

Superexchange may play an important role in other types of systems, such as mixed-matrix type host materials in small-molecule OLEDs [117] and in polymer OLEDs in which matrix materials co-polymerize with hole-transporting units which act as traps [118]. The effect can also play an important role in exciton transport [119]: the emitter molecules of the systems investigated in this Letter have triplet energies that are approximately 0.3 – 0.4 eV smaller than the host triplet energies. Guest to host exciton hopping is therefore heavily suppressed, and a superexchange mechanism could contribute to enhanced Dexter-type [120] guest-to-guest exciton transport. This would however only be relevant if Förster transfers are suppressed in the absence of spin-orbit coupling. The superexchange mechanism might also be relevant for charge transport in low donor concentration organic photovoltaics. For some small molecule based materials maximum power conversion efficiency is reached at a donor concentration of 5% [121, 122]. At this concentration a further decrease of donor concentration further increases open circuit voltages but abruptly reduces short circuit currents as charge transport is no more possible. The efficiency of charge transfer down to 5% donor concentration is however surprising and may be explained by superexchange mediated hopping between donors.

Chapter 6

Metal organic-semiconductor metal devices

In this chapter I will study a device made by sandwiching the hole conducting organic material $\alpha - NPD$ between two gold electrodes. As both the morphological simulation of an metal organic interface as well as electronic structure calculations are highly involved I will introduce a rough model to estimate metal-organic coupling to obtain quantitative injection rates. Using this model and the injection rate proposed in Chapter 3.2, I will then calculate IV-characteristics of the sandwiched device and investigate the enhancement of hole injection by hole transfer to the organic material through virtual states of $\alpha - NPD$ bridge molecules close to the metal organic interface.

6.1 Charge injection in disordered organic materials

In organic electronic devices, charge injection is a crucial process for the device performance as it strongly influences charge carrier balance, turn on voltage and the resistance of the device. As described in chapter 3, in my simulations the metal is not modeled explicitly but by allowing charge creation and annihilation on $\alpha - NPD$ molecules at the edge of the organic layer. Charge creation and annihilation rates emulate charge injection from a flat metallic electrode. The electrostatic potential throughout the $\alpha - NPD$ layer obeys the classical boundary conditions imposed by the electrodes, i.e. screening of all charges at the virtual metal surface as described in 3.3.2. An injection barrier for the charge creation on the interface sites reflects the difference of the Fermi level in the metal and the ionization potential / electron affinity on the molecules. Hybridization between metal and $\alpha - NPD$ is neglected and the renormalization of states on the $\alpha - NPD$ molecules close to the electrode is taken as purely classical, see 3.2.2. Injection rates are calculated as modified Miller-Abrahams rates 3.2.2. A rough approximation of the metal organic transfer integrals based on the organic-organic transfer integrals is given below. If the differences between Fermi level in the metal and ionization potential/electron affinity on the molecules is small, the charge transport happens in the space charge limited regime (SCLC) where the conductivity of the device is mostly determined by the mobility of the organic material [62]. In this case there is an equilibrium accumulation of charge

near the electrodes due to the increased coulomb screening (i.e. attraction from mirror charges). At low applied fields, this equilibrium distribution is independent of the coupling between electrode and metal, such that measured IV-characteristics do not depend on an exact coupling model if the coupling is chosen large enough that the space charge region at the interface is not depleted due to diffusion into the device.

The Au- α -NPD-Au system studied here has however an offset of roughly 1 eV between gold Fermi level and α -NPD ionization potential [74]. In this case the current is injection limited (ILC), as injection rates are suppressed by a Boltzmann factor roughly 40 times room temperature. The disorder of molecular ionization potentials means a lowered injection barrier into tail-states of the Gaussian distribution of states, see fig. 6.1.1 b). Applying an electric field reduces the injection barrier the stronger, the further a hole is injected into the sample, such that doubling the applied voltage can increase the current by three orders of magnitude [74].

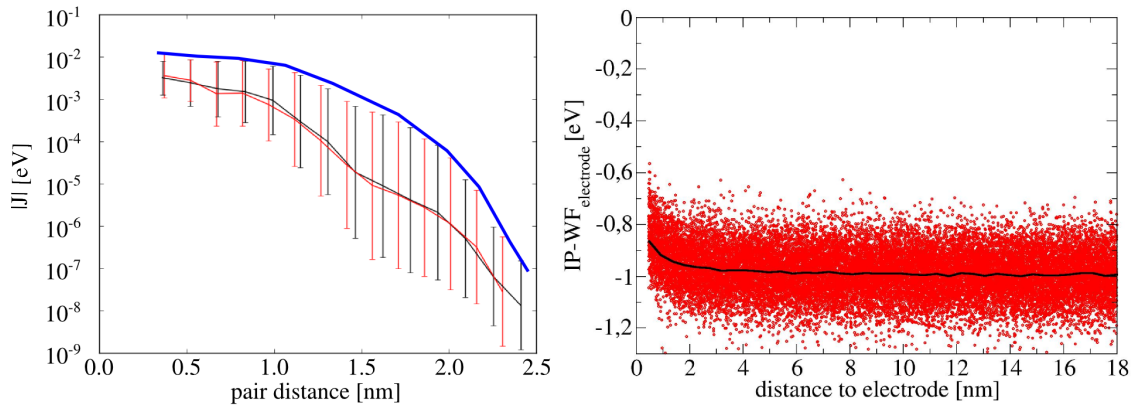


Figure 6.1.1: a) Distance dependent average of α -NPD transfer integrals and standard deviation. The transfer integral of α -NPD molecules to the metal electrode is estimated by the average α -NPD - α -NPD coupling + 1 standard deviation (blue line), as wavefunction overlap can be expected for any orientation. b) Distribution of α -NPD ionization potentials near an electrode with 5 eV workfunction (value of Au). Electrostatic screening lowers the ionization potential.

In the ILC regime, the injection model strongly influences the simulated charge transport. In order to obtain a realistic current voltage dependence, the distance dependence of the metal organic transfer integrals has to be modeled correctly. Though absolute values of the current-voltage characteristic depend on correct absolute values of the transfer integrals, the validity of the injection model can be judged by comparing relative current voltage dependence of experiment and simulation. I construct an educated guess of the direct metal organic transfer integrals based on the assumption that the transfer-integrals are mostly determined by the overlap of the molecular HOMO with metal surface states. I assume this overlap to be largely determined by the geometry of α -NPD, such that it will have a similar dependence on the distance between electrode and molecular center of mass, as the center of mass distances of pairs of α -NPD-molecules. The distribution

of transfer integrals between α -NPD-molecules at a given center of mass distance (see fig. 3.3.6) is mainly due to different orientation of the molecules. If the long axes of a pair of molecules is aligned with the center of mass distance vector, the distance of close carbon atoms (i.e. π -states) is clearly smaller than if both long axes are aligned perpendicular to the distance vector. In case of the metal-organic coupling the distance dependent distribution of transfer integrals can be expected to be narrower, as only one molecule is rotated and will at any rotation face some surface states on the metal. I thus assume the same slope of the average distance dependence for the metal organic coupling as for the organic organic coupling, but assume the average value of the metal organic coupling to be larger due to the geometric considerations mentioned above. As distance dependent offset I take one standard deviation of the organic organic transfer integrals for a given distance (blue line in fig. 6.1.1 a).

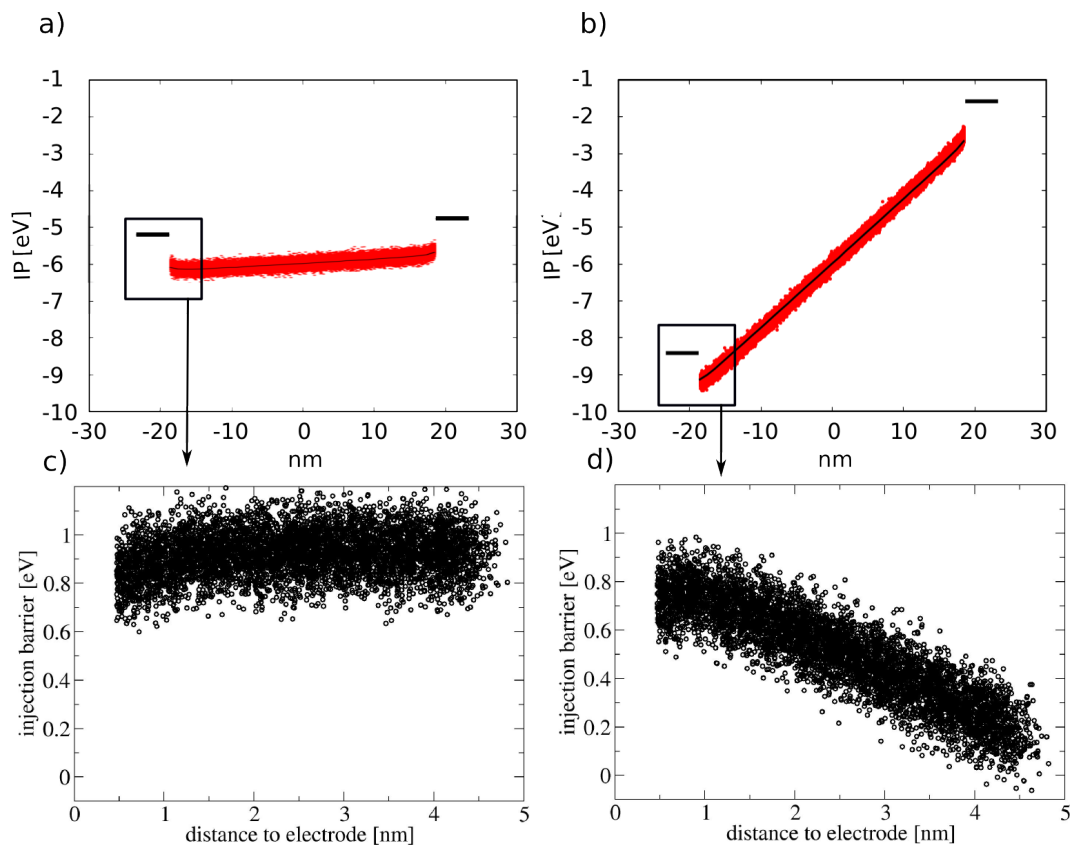


Figure 6.1.2: a) and b): Ionization potential of α -NPD molecules between the boundary conditions of two metallic leads, with an applied electric field of 0.01 V/nm (a) and 0.18 V/nm (b). c) and d) show the resulting distant dependent injection barriers. At the low field the best injection sites are close to the electrode where electrostatic screening is strongest. For the high field injection far into the material will reduce the injection barrier significantly.

For every molecule close to an electrode I then assign the metal organic transfer integrals according to this distance dependent function $J_{inj}(x)$.

$$J_{inj}(x) = J_{A,B}^-(x) + \sqrt{\frac{1}{N_x} \sum_{A,B:r_{A,B}>x-\Delta x}^{r_{A,B}<x+\Delta x} (J_{A,B}^-(x) - J_{A,B})^2} \quad (6.1.1)$$

where x is the distance to the electrode, $r_{A,B}$ the center of mass distance of pairs of $\alpha - NPD$ molecules (A,B), $2\Delta x$ the sampling interval for the distance dependence, $J_{A,B}$ the transfer integral of the $\alpha - NPD$ pair (A,B), $J_{A,B}^-(x)$ the average of transfer integrals in the sampling interval around x and N_x the number of $\alpha - NPD$ pairs in the sampling interval.

Additionally to this direct coupling, I consider second order transfer integrals to molecules further into the morphology. Charge can then directly hop on states a few nm away from the interface by transitions through virtual states of organic molecules at the interface (compare chapter 5). The second order coupling to a molecule B is given by:

$$J_{inj,B}^{sx} = \sum_{i=1}^N \frac{J_{inj}(x[A_i])J_{A_i,B}}{\Delta E_{A_iB}} \quad (6.1.2)$$

where A_i are molecules close to the electrode and molecule B and

$$\Delta E_{A_iB} = E_A - \frac{\phi + E_B}{2} + \frac{\lambda_A}{2} \quad (6.1.3)$$

where ϕ is the workfunction of the electrode, E_B and E_A the ionization potentials of the molecules, λ_A the reorganization energy of molecule A. The derivation of the denominator is analogous to eq. 5.0.4, with the difference that the Marcus parabolas represent the total energy of electrode + molecule B once when molecule B is charged and once when the charge is in the electrode. The reaction coordinate only reflects conformational changes of molecule B.

As the direct transfer integrals $J_{A_i,B}$ are obtained as described in section 3.3.3, the relative phase between the transfer matrix elements between two pairs of molecules is not known. This means the interference between path through different molecules A_i in eq.6.1.2 is not taken into account and constructive interference is taken as an upper limit of the transfer integrals. The large spread of the transfer integrals of the organic-organic molecules $J_{A_i,B}$ (compare fig. 3.3.6), makes this a reasonable approach, as one coupling is likely to give the major contribution to the sum.

Direct and direct + superexchange transfer integrals are shown in fig. 6.1.3 a). For electrode α -NPD distances of less than 2 nm the direct coupling is giving the main contribution to the transfer integrals, at larger distances the superexchange coupling significantly increases the coupling to the electrode. The resulting effect on injection rates strongly depends on the distance dependence of the injection barrier to the electrode i.e. the applied electric field. Fig. 6.1.2 shows the energy levels of the modeled device for an electric field of 0.01 v/nm and 0.18 V/nm. In the case of the weak field, the injection barrier is increasing with increasing distance to the electrode, as the lowering of energy

levels close to the electrode due to the image charge effect is stronger than the effect of the applied field. For the strong field, the injection barrier is decreased by 0.6 eV at 4 nm distance, with some of the disordered states even showing a complete negation of the injection barrier.

Field dependent injection rates taking superexchange into account and only by direct injection are plotted in fig. 6.1.3 b-d). At strong field the combination of reduced injection barriers and appreciable transfer integrals strongly enhances injections rates. At low field, the highest injection rates are in molecules close to the electrode as the injection barriers are lowest.

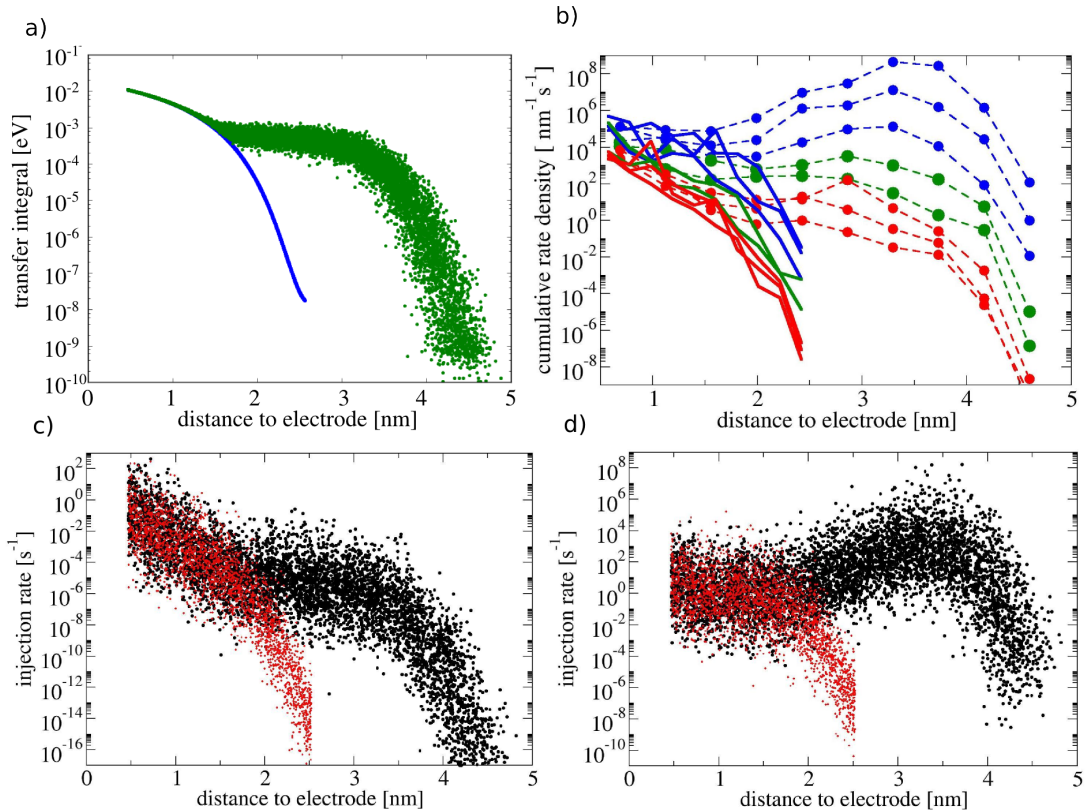


Figure 6.1.3: a) In blue, direct metal-organic transfer integrals dependent on the distance of the molecule to the electrode. In green superexchange transfer integrals through virtual states on molecules close to the electrode. The superexchange significantly increases injection range. b) Sum of injection rates to molecules in the simulated sample in given distance intervals. Shown are values for 8 different fields (blue 0.18 v/nm, 0.15 V/nm, 0.12 V/nm), green (0.09 V/nm, 0.06 V/nm) and red (0.01 V/nm, 0.02 V/nm, 0.04 V/nm) with superexchange (dashed lines and circles) and without superexchange(full lines). In the blue group superexchange rates are orders of magnitude higher than rates without superexchange. In the green group the highest injection rates are still at short distances both with and without superexchange, but the long range superexchange contributions are not negligible to the total injection rate i.e. integration over all distances. In the red group short range contribution dominate the total injection rate with and without superexchange. These three groups are reflected in IV-measurements in presented in fig.6.2.1.c) and d): Distribution of injection rates with (black) and without(red) superexchange at a fields of 0.01 v/nm (c) and 0.18 V/nm (d). The increased injection rates in d) are due to the lowering of the injection barriers shown in fig. 6.1.2.

6.2 Current voltage characteristics of α -NPD

Resulting current voltage characteristics of kMC calculations and data from experimental measurements[74] are shown in fig. 6.2.1. The kMC calculations were done on a $37 \times 37 \times 37 \text{ nm}^3$ α -NPD morphology generated as described in chapter 3.3.1. Electrodes were attached at 0.5nm distance from the closest α -NPD center of mass, about 0.1 nm closer than the shortest center of mass distance between pairs of α -NPD molecules in the simulated morphology. The difference between α -NPD ionization potential and Au fermi level is taken as 1.0 eV.

At low and intermediate fields, the calculated IV-characteristics show a very good agreement with the experimental measurements. At the highest field the calculations including superexchange are a factor 50 higher than experimental measurements, the calculations without superexchange a factor 500 below experimental measurements. It seems apparent, that an injection mechanism not allowing for injection far into the system can not explain the high field behavior. The overestimation of the current at high field might be due to the overestimation of superexchange transfer integrals caused by the neglect of destructive interference in eq. 6.1.2. A simple approach to test this hypothesis would be the repeat of the calculations assuming random phases.

An analysis of the percolation behavior at different fields is shown in 6.2.1 b)-f). At low applied field strength the current flows through a smaller subset of molecules. While at 0.01 V/nm 99 % of the net current as defined in 4.2.3 pass through 6% of the system. At the three highest fields the size of the current carrying system does not increase further above 65%. This corresponds well with the distance dependence of the injection rates at these fields shown in fig. 6.1.3, where the highest injection rates are far into the system. Due to the lowered injection barriers the number of potential injection sites increases, as injection is not only possible in tail states anymore.

In conclusion, I have shown that charge injection and transport in injection limited organic semi-conductor devices can be quantitatively modeled by kMC calculations. An estimation of the metal organic coupling from the distribution of organic-organic transfer-integrals yields current voltage characteristic in good agreement with experimental measurements at low to intermediate fields. At high applied voltages currents are strongly enhanced by allowing charge injection through virtual states on organic molecules close to the electrodes. The interference of different injection path should be investigated in future studies.

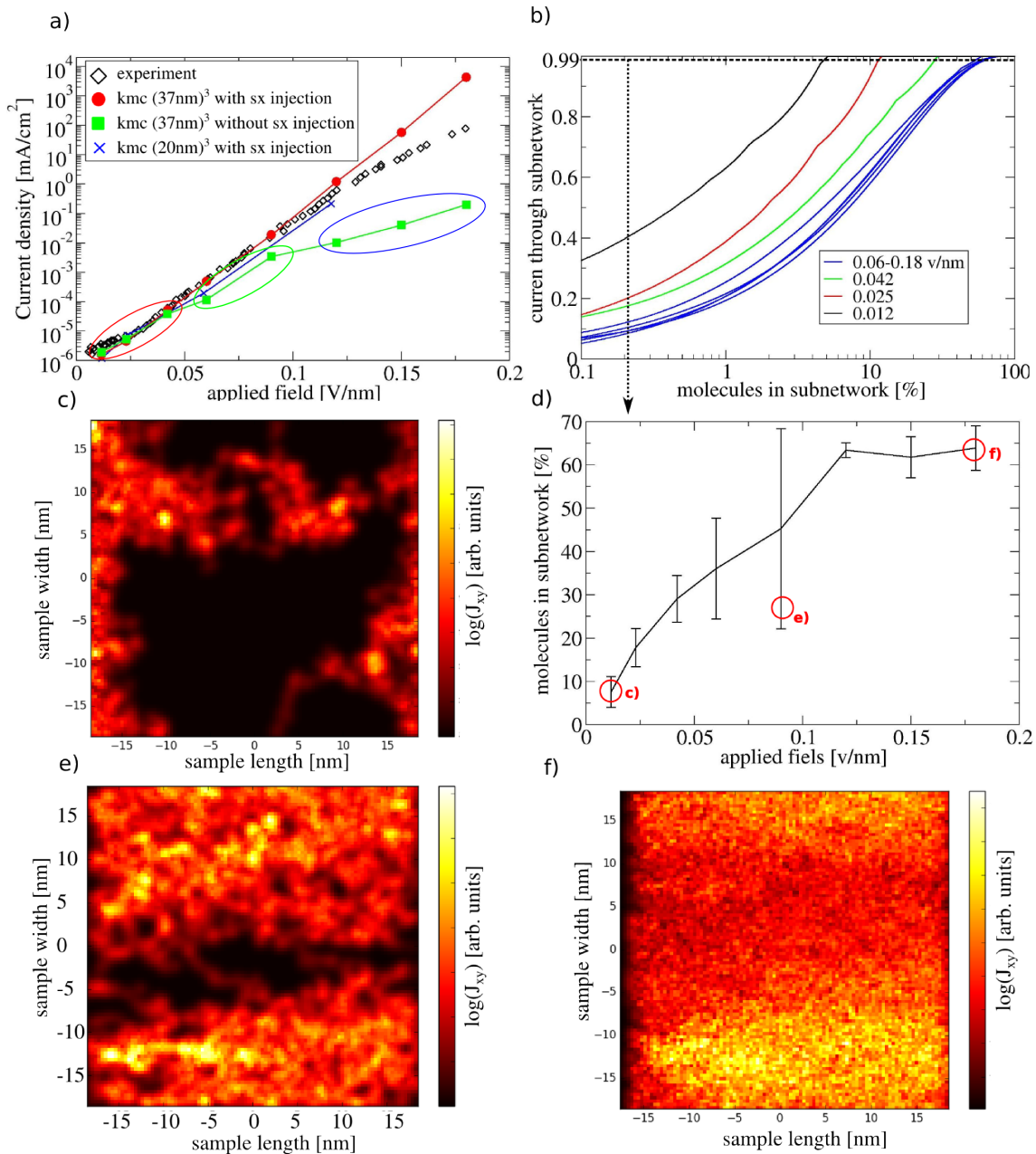


Figure 6.2.1: a) current voltage characteristics of α -NPD sandwiched between two Au electrodes. Experimental values [74] are shown as diamonds, values obtained by kMC simulations including an upper estimate on superexchange coupling between electrode and α -NPD are shown as blue crosses (small system) and red dots (big system) and including only direct coupling as green squares. b) Fraction of the molecules contributing to the total current depending on the field strength. The lower the fields the less molecules contribute to the conducting network. At the three highest fields, the size of the used subsystem saturates, as the number of injection sites rises strongly (compare injection rates fig. 6.1.3). c) Projection of the current as defined in eq. 4.2.3 at a field of $0.01 \text{ V}/\text{nm}$ on the xy plane. Electrodes are right and left. The current only flows through a small part of the system. d) Fraction of molecules which carry 99% of the current depending on the applied field. The error bars reflect calculations on different instances of randomly generated α -NPD systems. e) Current density at $0.09 \text{ V}/\text{nm}$ in the configuration which presented an statistical outlier in percolation behavior at this field. f) Current density at $0.18 \text{ V}/\text{nm}$: The current goes uniform through the system.

Chapter 7

Summary and outlook

Summary Organic semi-conductors are a class of materials used in a multitude of applications such as organic photovoltaics (OPV), organic transistors or organic light emitting diodes (OLEDs). The performance of organic electronic devices is largely determined by their meso scale charge transport properties. One example for this is the charge carrier balance in OLEDs, which determines where and at what rate excitons are created and how they interact with each other and with free charge carriers. As device aging and high voltage luminescence efficiency strongly depend on these interactions, understanding and predicting charge transport, creation, annihilation and interaction is very important to improve modern OLEDs.

To this purpose I introduced a transport model, which explicitly models the propagation and interaction of charges and excitons in organic bulk materials or devices and permits unprecedented insights into the underlying transport processes.

As the simulation of realistic devices and representative sampling of charge percolation paths in bulk materials requires morphologies of organic materials orders of magnitude larger than obtainable from atomistic, even less electronic, simulations, Chapter 3.3 introduced a method to construct mesoscale representations of amorphous organic semi-conductors using a stochastic extrapolation scheme based on atomistic morphologies and electronic structure calculations.

To overcome prohibitive run-times of the charge propagation simulations, I developed highly efficient routines for the calculation of coulomb calculations and an algorithm to accelerate the phase space sampling of kinetic Monte-Carlo protocols. An kinetic Monte-Carlo algorithm requires an update of all transition rates after every iteration. As all charge transfer rates are influenced by the time dependent Coulomb potential, a computationally efficient method to calculate the Ewald sum over charges and image charge copies was introduced in Chapter 3.3.2. In Chapter 3.4 an algorithm to accelerate the sampling of the Markov-chain of system states was presented. A dynamic rate buffer thereby tracks states which are likely to occur and saves coulomb potential and rates of the states for tabulation. In systems with deep traps the protocol was demonstrated to accelerate calculations the more, the higher the number of electrons in the system.

Using this model I reproduced experimental field and temperature dependence of the hole mobility of a typical organic hole conductor in Chapter 4. An analysis of the transport

path showed that in systems of low energy disorder current filaments go through links with large transfer integrals. With increasing energy disorder the transfer integrals in the current filaments decrease while the current seeks to minimize energy disorder in the filament. At low energy disorder transport is determined by transfer integrals, at high disorder by the energy differences between the states on the molecules.

In Chapter 4.3 I tested the generalized effective medium model [35] of charge transport in disordered media against mobilities from kMC calculations. The calculations showed, that the generalized effective medium model predicts the correct order of mobility magnitude for all tested energy disorder strength of the amorphous semiconductor.

I extended currently existing transport models by formulating a hopping rate expression for hops through virtual states on intermediate molecules and developed an efficient calculation scheme for these 2nd order transition rates in mesoscale systems. I then showed that these second order processes increase hole mobilities by an order of magnitude in OLED host-guest systems. Many OLEDs use host-guest systems of transport and dye molecules as emissive layers. Emitter concentration in these system is often between 5%-15%. The light emitting dyes act as charge and exciton traps. Due to the low emitter concentration it is unclear how charge transport in a host-guest system works. In Chapter 5 I calculated bulk hole transport in a quintessential red and green emissive layer and showed that transfer integrals between dyes bridged by virtual states on host molecules lead to an increase of mobility by up to an order of magnitude for the green emitter. The impact of the second order coupling thereby strongly depends on the trap depth on the dye, where a dominant contribution of the second order over the first order transfer integral can be expected for trap depth > 0.4 eV. I further showed that lattice models which are commonly used in organic semiconductor transport simulations, do not reflect the character of hole transport through the network of dyes correctly.

In Chapter 6 I model transport through the hole-conducting material α -NPD attached to 2 gold leads. An estimation of metal organic transfer integrals from the organic-organic transfer integrals and a thumb rule injection rate expression 3.2.2 results in a good agreement of the IV-characteristics with experimental measurements. At high fields charge injection rates were seen to be vastly increased by transfer integrals between metal and α -NPD molecules 3-4 nm into the device which were bridged by virtual states on α -NPD molecules close to the metal organic interface.

Applications of the transport model outside this thesis The transport model and the algorithms introduced in this thesis are used in the EU Horizon 2020 project EXTMOS to calculate full OLED devices.

The developed software is furthermore used by industrial partners to calculate charge transport properties of organic-materials.

In cooperation with TU Eindhoven, the generation scheme for meso-scale representations of amorphous semiconductors presented in this thesis was used in transport studies based on Master-equation approaches [38, 39, 40].

Outlook In many modern OLEDs, injection barriers for electrons and holes are reduced by introducing charge injection layers. These injection layers consist of transport materials doped with charge donating molecules. Close to the electrodes, donated charges are extracted from the system leading to a charge depletion zone which lowers injection barriers on molecules behind the depletion zone significantly. In future work I will simulate charge doping and investigate the effect of doping on injection efficiency in the kMC hopping model.

An extension of the transport model which incorporates multiple states of charged molecules will be implemented to investigate the role of "hot" charges for electron-hole separation in organic photovoltaic devices.

Bibliography

- [1] R McNeill et al. “Electronic Conduction in Polymers. I. The Chemical Structure of Polypyrrole”. en. In: *Australian Journal of Chemistry* 16.6 (1963), p. 1056. ISSN: 0004-9425.
- [2] C. W. Tang and S. A. VanSlyke. “Organic electroluminescent diodes”. en. In: *Applied Physics Letters* 51.12 (Sept. 1987), pp. 913–915. ISSN: 0003-6951, 1077-3118.
- [3] David Kearns and Melvin Calvin. “Photovoltaic Effect and Photoconductivity in Laminated Organic Systems”. en. In: *The Journal of Chemical Physics* 29.4 (Oct. 1958), pp. 950–951. ISSN: 0021-9606, 1089-7690.
- [4] J. McGinness, P. Corry, and P Proctor. “Amorphous semiconductor switching in melanins”. In: *Science* 183 (1974), p. 853.
- [5] P. Goerrn et al. “Towards See-Through Displays: Fully Transparent Thin-Film Transistors Driving Transparent Organic Light-Emitting Diodes”. en. In: *Advanced Materials* 18.6 (2006), pp. 738–741. ISSN: 0935-9648, 1521-4095.
- [6] Tae-Hee Han et al. “Extremely efficient flexible organic light-emitting diodes with modified graphene anode”. In: *Nature Photonics* 6.2 (Jan. 2012), pp. 105–110. ISSN: 1749-4885, 1749-4893.
- [7] D. Y. Kondakov, W. C. Lenhart, and W. F. Nichols. “Operational degradation of organic light-emitting diodes: Mechanism and identification of chemical products”. en. In: *Journal of Applied Physics* 101.2 (Jan. 2007), p. 024512. ISSN: 0021-8979, 1089-7550.
- [8] Hany Aziz and Zoran D. Popovic. “Degradation Phenomena in Small-Molecule Organic Light-Emitting Devices”. en. In: *Chemistry of Materials* 16.23 (Nov. 2004), pp. 4522–4532. ISSN: 0897-4756, 1520-5002.
- [9] Vincenzo Fiore et al. “An Integrated 13.56-MHz RFID Tag in a Printed Organic Complementary TFT Technology on Flexible Substrate”. In: *IEEE Transactions on Circuits and Systems I: Regular Papers* 62.6 (2015), pp. 1668–1677. ISSN: 1549-8328, 1558-0806.
- [10] H. E. A. Huitema et al. “Plastic transistors in active-matrix displays”. In: *Nature* 414.6864 (Dec. 2001), pp. 599–599. ISSN: 00280836.
- [11] Gerwin H. Gelinck et al. “Flexible active-matrix displays and shift registers based on solution-processed organic transistors”. In: *Nature Materials* 3.2 (Feb. 2004), pp. 106–110. ISSN: 1476-1122, 1476-4660.

- [12] P. Andersson et al. “Active Matrix Displays Based on All-Organic Electrochemical Smart Pixels Printed on Paper”. In: *Advanced Materials* 14.20 (Oct. 2002), pp. 1460–1464. ISSN: 09359648, 15214095.
- [13] Hitesh Khandelwal, Albertus P. H. J. Schenning, and Michael G. Debije. “Infrared Regulating Smart Window Based on Organic Materials”. en. In: *Advanced Energy Materials* (Mar. 2017), p. 1602209. ISSN: 16146832.
- [14] Bernard Kippelen and Jean-Luc Bredas. “Organic photovoltaics”. en. In: *Energy & Environmental Science* 2.3 (2009), p. 251. ISSN: 1754-5692, 1754-5706.
- [15] *Heliatek – The future is light - Heliatek sets new Organic Photovoltaic world record efficiency of 13.2%*.
- [16] H Klauk. *Organic Electronics: Materials, Manufacturing and Applications*. Weinheim: Wiley-VCH, 2006. ISBN: 9783527312641.
- [17] Sang-Il Shin et al. “Solution-processed 6,13-bis(triisopropylsilylethynyl) (TIPS) pentacene thin-film transistors with a polymer dielectric on a flexible substrate”. In: *Semiconductor Science and Technology* 23.8 (Aug. 2008), p. 085009. ISSN: 0268-1242, 1361-6641.
- [18] Jaewook Jung et al. “Highly Efficient Inkjet-Printed Organic Photovoltaic Cells”. en. In: *Japanese Journal of Applied Physics* 49.5 (2010), 05EB03. ISSN: 0021-4922, 1347-4065.
- [19] Lintao Hou et al. “Lateral Phase Separation Gradients in Spin-Coated Thin Films of High-Performance Polymer:Fullerene Photovoltaic Blends”. en. In: *Advanced Functional Materials* 21.16 (2011), pp. 3169–3175. ISSN: 1616301X.
- [20] Zhitao Zhang et al. “A Lightweight Polymer Solar Cell Textile that Functions when Illuminated from Either side”. en. In: *Angewandte Chemie International Edition* 53.43 (2014), pp. 11571–11574. ISSN: 14337851.
- [21] N. C. Giebink and S. R. Forrest. “Quantum efficiency roll-off at high brightness in fluorescent and phosphorescent organic light emitting diodes”. en. In: *Physical Review B* 77.23 (June 2008). ISSN: 1098-0121, 1550-235X.
- [22] Caroline Murawski, Karl Leo, and Malte C. Gather. “Efficiency Roll-Off in Organic Light-Emitting Diodes”. en. In: *Advanced Materials* 25.47 (Dec. 2013), pp. 6801–6827. ISSN: 09359648.
- [23] Li-Li Wen et al. “Low efficiency roll-off and high performance OLEDs employing alkyl group modified iridium(III) complexes as emitters”. en. In: *RSC Adv.* 6.112 (2016), pp. 111556–111563. ISSN: 2046-2069.
- [24] Stephan Winter et al. “Photoluminescence degradation of blue OLED emitters”. In: ed. by Paul L. Heremans, Michele Muccini, and Eric A. Meulenkaamp. Apr. 2008, 69992N.

- [25] D. Y. Kondakov et al. “Nonradiative recombination centers and electrical aging of organic light-emitting diodes: Direct connection between accumulation of trapped charge and luminance loss”. en. In: *Journal of Applied Physics* 93.2 (Jan. 2003), pp. 1108–1119. ISSN: 0021-8979, 1089-7550.
- [26] Malte C. Gather, Anne Köhnen, and Klaus Meerholz. “White Organic Light-Emitting Diodes”. en. In: *Advanced Materials* 23.2 (Jan. 2011), pp. 233–248. ISSN: 09359648.
- [27] Shi-Jian Su et al. “Highly Efficient Organic Blue-and White-Light-Emitting Devices Having a Carrier- and Exciton-Confining Structure for Reduced Efficiency Roll-Off”. en. In: *Advanced Materials* (Oct. 2008), NA–NA. ISSN: 09359648, 15214095.
- [28] M. Mesta et al. “Kinetic Monte Carlo modeling of the efficiency roll-off in a multilayer white organic light-emitting device”. en. In: *Applied Physics Letters* 108.13 (Mar. 2016), p. 133301. ISSN: 0003-6951, 1077-3118.
- [29] L. Zhang et al. “Clarifying the mechanism of triplet–triplet annihilation in phosphorescent organic host–guest systems: A combined experimental and simulation study”. en. In: *Chemical Physics Letters* 652 (May 2016), pp. 142–147. ISSN: 00092614.
- [30] Reinder Coehoorn et al. “Kinetic Monte Carlo Study of the Sensitivity of OLED Efficiency and Lifetime to Materials Parameters”. en. In: *Advanced Functional Materials* 25.13 (Apr. 2015), pp. 2024–2037. ISSN: 1616301X.
- [31] M Ben Khalifa, D Vaufrey, and J Tardy. “Opposing influence of hole blocking layer and a doped transport layer on the performance of heterostructure OLEDs”. en. In: *Organic Electronics* 5.4 (2004), pp. 187–198. ISSN: 15661199.
- [32] Daniel Ping-Kuen Tsang, Toshinori Matsushima, and Chihaya Adachi. “Operational stability enhancement in organic light-emitting diodes with ultrathin Liq interlayers”. en. In: *Scientific Reports* 6.1 (Apr. 2016). ISSN: 2045-2322.
- [33] Sung Hoon Choi et al. “Improved Efficiency and Lifetime of Organic Light-Emitting Diode with Lithium-Quinolate-Doped Electron Transport Layer”. en. In: *Japanese Journal of Applied Physics* 48.6 (June 2009), p. 062101. ISSN: 0021-4922, 1347-4065.
- [34] Murat Mesta et al. “Molecular-scale simulation of electroluminescence in a multilayer white organic light-emitting diode”. In: *Nature Materials* 12.7 (2013), pp. 652–658. ISSN: 1476-1122, 1476-4660.
- [35] Vadim Rodin et al. “A generalized effective medium model for the carrier mobility in amorphous organic semiconductors”. In: *Physical Review B* 91.15 (2015).
- [36] Franz Symalla et al. “Charge Transport by Superexchange in Molecular Host-Guest Systems”. In: *Physical Review Letters* 117 (2016), p. 276803.
- [37] Tobias Neumann et al. “Superexchange Charge Transport in Loaded Metal Organic Frameworks”. In: *ACS nano* 10.7 (2016), pp. 7085–7093.

- [38] Andrea Masse et al. “Ab initio charge-carrier mobility model for amorphous molecular semiconductors”. In: *Physical Review B* 93.19 (2016), p. 195209.
- [39] Andrea Masse et al. “Effects of energy correlations and superexchange on charge transport and exciton formation in amorphous molecular semiconductors: An ab initio study”. In: *accepted in Physical Review B* (2017).
- [40] Feilong Liu et al. “Ab initio modeling of steady-state and time-dependent charge transport in hole-only alpha-NPD devices”. In: *Applied Physics Letters* 109.24 (2016), p. 1243301.
- [41] J. Wang et al. “Heterojunction Ambipolar Organic Transistors Fabricated by a Two-Step Vacuum-Deposition Process”. en. In: *Advanced Functional Materials* 16.6 (Apr. 2006), pp. 824–830. ISSN: 1616-301X, 1616-3028.
- [42] Jianguo Mei and Zhenan Bao. “Side Chain Engineering in Solution-Processable Conjugated Polymers”. en. In: *Chemistry of Materials* 26.1 (Jan. 2014), pp. 604–615. ISSN: 0897-4756, 1520-5002.
- [43] Ferdinand C. Grozema et al. “Intramolecular Charge Transport along Isolated Chains of Conjugated Polymers: Effect of Torsional Disorder and Polymerization Defects”. en. In: *The Journal of Physical Chemistry B* 106.32 (Aug. 2002), pp. 7791–7795. ISSN: 1520-6106, 1520-5207.
- [44] Rodrigo Noriega et al. “A general relationship between disorder, aggregation and charge transport in conjugated polymers”. In: *Nature Materials* 12.11 (Aug. 2013), pp. 1038–1044. ISSN: 1476-1122, 1476-4660.
- [45] Veaceslav Coropceanu et al. “Charge Transport in Organic Semiconductors”. en. In: *Chemical Reviews* 107.4 (Apr. 2007), pp. 926–952. ISSN: 0009-2665, 1520-6890.
- [46] A V Nenashev, J O Oelerich, and S D Baranovskii. “Theoretical tools for the description of charge transport in disordered organic semiconductors”. In: *Journal of Physics: Condensed Matter* 27.9 (Mar. 2015), p. 093201. ISSN: 0953-8984, 1361-648X.
- [47] O. Ostroverkhova et al. “Bandlike transport in pentacene and functionalized pentacene thin films revealed by subpicosecond transient photoconductivity measurements”. en. In: *Physical Review B* 71.3 (Jan. 2005). ISSN: 1098-0121, 1550-235X.
- [48] Karl F. Freed and Joshua Jortner. “Multiphonon Processes in the Nonradiative Decay of Large Molecules”. en. In: *The Journal of Chemical Physics* 52.12 (June 1970), pp. 6272–6291. ISSN: 0021-9606, 1089-7690.
- [49] Burkhard Fueckel et al. “Theoretical investigation of electronic excitation energy transfer in bichromophoric assemblies”. In: *The Journal of Chemical Physics* 128.7 (2008), p. 074505. ISSN: 00219606.
- [50] Allen Miller and Elihu Abrahams. “Impurity conduction at low concentrations”. In: *Physical Review* 120.3 (1960), p. 745.
- [51] Vinay Ambegaokar, B. I. Halperin, and J. S. Langer. “Hopping Conductivity in Disordered Systems”. en. In: *Physical Review B* 4.8 (Oct. 1971), pp. 2612–2620. ISSN: 0556-2805.

- [52] W. F. Pasveer et al. “Unified Description of Charge-Carrier Mobilities in Disordered Semiconducting Polymers”. en. In: *Physical Review Letters* 94.20 (May 2005). ISSN: 0031-9007, 1079-7114.
- [53] R. Coehoorn and P. A. Bobbert. “Effects of Gaussian disorder on charge carrier transport and recombination in organic semiconductors”. en. In: *physica status solidi (a)* 209.12 (Dec. 2012), pp. 2354–2377. ISSN: 18626300.
- [54] Rudolph A. Marcus. “Electron transfer reactions in chemistry. Theory and experiment”. en. In: *Reviews of Modern Physics* 65.3 (July 1993), pp. 599–610. ISSN: 0034-6861, 1539-0756.
- [55] Rudolph A Marcus. “On the Theory of Oxidation-Reduction Reactions Involving Electron Transfer. I”. In: *The Journal of Chemical Physics* 24.5 (1956), pp. 966–978.
- [56] Stephen F. Nelsen, Silas C. Blackstock, and Yaesil Kim. “Estimation of inner shell Marcus terms for amino nitrogen compounds by molecular orbital calculations”. en. In: *Journal of the American Chemical Society* 109.3 (Feb. 1987), pp. 677–682. ISSN: 0002-7863.
- [57] V. Stehr et al. “First-principles calculations of anisotropic charge-carrier mobilities in organic semiconductor crystals”. en. In: *Physical Review B* 83.15 (Apr. 2011). ISSN: 1098-0121, 1550-235X.
- [58] Pascal Friederich et al. “Ab Initio Treatment of Disorder Effects in Amorphous Organic Materials: Toward Parameter Free Materials Simulation”. In: *Journal of Chemical Theory and Computation* 10.9 (2014), pp. 3720–3725.
- [59] Pascal Friederich et al. “A QM/QM approach to model energy disorder in amorphous organic semiconductors”. In: *Journal of Chemical Theory and Computation* 11.2 (2015), 560–567.
- [60] Th. Foerster. “Zwischenmolekulare Energiewanderung und Fluoreszenz”. en. In: *Annalen der Physik* 437.1-2 (1948), pp. 55–75. ISSN: 1521-3889.
- [61] D. L. Dexter. “A Theory of Sensitized Luminescence in Solids”. In: *The Journal of Chemical Physics* 21.5 (1953), pp. 836–850. ISSN: 00219606.
- [62] J. J. M. van der Holst et al. “Monte Carlo study of charge transport in organic sandwich-type single-carrier devices: Effects of Coulomb interactions”. en. In: *Physical Review B* 83.8 (Feb. 2011). ISSN: 1098-0121, 1550-235X.
- [63] A. Masse, R. Coehoorn, and P.A. Bobbert. “Universal Size-Dependent Conductance Fluctuations in Disordered Organic Semiconductors”. en. In: *Physical Review Letters* 113.11 (Sept. 2014). ISSN: 0031-9007, 1079-7114.
- [64] H. Baessler. “Charge Transport in Disordered Organic Photoconductors a Monte Carlo Simulation Study”. de. In: *physica status solidi (b)* 175.1 (Jan. 1993), pp. 15–56. ISSN: 03701972, 15213951.
- [65] L Pautmeier, R Richert, and H Baessler. “Poole-Frenkel behavior of charge transport in organic solids with off-diagonal disorder studied by Monte Carlo simulation”. en. In: *Synthetic Metals* 37.1-3 (Aug. 1990), pp. 271–281. ISSN: 03796779.

- [66] M. Mesta et al. “Kinetic Monte Carlo modeling of the efficiency roll-off in a multilayer white organic light-emitting device”. en. In: *Applied Physics Letters* 108.13 (Mar. 2016), p. 133301. ISSN: 0003-6951, 1077-3118.
- [67] L. Zhang et al. “Analysis of the phosphorescent dye concentration dependence of triplet-triplet annihilation in organic host-guest systems”. en. In: *Chemical Physics Letters* 662 (Oct. 2016), pp. 221–227. ISSN: 00092614.
- [68] Robin G. E. Kimber et al. “Mesoscopic kinetic Monte Carlo modeling of organic photovoltaic device characteristics”. en. In: *Physical Review B* 86.23 (Dec. 2012). ISSN: 1098-0121, 1550-235X.
- [69] Peter K. Watkins, Alison B. Walker, and Geraldine L. B. Verschoor. “Dynamical Monte Carlo Modelling of Organic Solar Cells: The Dependence of Internal Quantum Efficiency on Morphology”. en. In: *Nano Letters* 5.9 (Sept. 2005), pp. 1814–1818. ISSN: 1530-6984, 1530-6992.
- [70] James Kirkpatrick et al. “Charge Mobility of Discotic Mesophases: A Multiscale Quantum and Classical Study”. en. In: *Physical Review Letters* 98.22 (May 2007). ISSN: 0031-9007, 1079-7114.
- [71] J. J. Kwiatkowski et al. “Simulating charge transport in tris(8-hydroxyquinoline) aluminium (Alq 3)”. en. In: *Physical Chemistry Chemical Physics* 10.14 (2008), pp. 1852–1858.
- [72] Pascal Kordt et al. “Modeling of Organic Light Emitting Diodes: From Molecular to Device Properties”. en. In: *Advanced Functional Materials* 25.13 (Apr. 2015), pp. 1955–1971. ISSN: 1616301X.
- [73] Bjoern Baumeier et al. “Stochastic modeling of molecular charge transport networks”. In: *Physical Review B* 86.18 (2012), p. 184202.
- [74] weiyang Gao and Antoine Kahn. “Controlled p doping of the hole-transport molecular material N,N-diphenyl-N,N-bis(1-naphthyl)-1,1-biphenyl-4,4-diamine with tetrafluorotetracyanoquinodimethane”. en. In: *Journal of Applied Physics* 94.1 (July 2003), pp. 359–366. ISSN: 0021-8979, 1089-7550.
- [75] Y Sakuratani et al. “Enhanced electron injection and electroluminescence in poly(N-vinyl carbazole) film doped with ammonium salt”. en. In: *Synthetic Metals* 123.2 (Sept. 2001), pp. 207–210. ISSN: 03796779.
- [76] X. Zhou et al. “Enhanced hole injection in a bilayer vacuum-deposited organic light-emitting device using a p -type doped silicon anode”. en. In: *Applied Physics Letters* 74.4 (Jan. 1999), pp. 609–611. ISSN: 0003-6951, 1077-3118.
- [77] Ken-Tsung Wong et al. “4,5-Diazafluorene-Incorporated Ter(9,9-diarylfuorene): A Novel Molecular Doping Strategy for Improving the Electron Injection Property of a Highly Efficient OLED Blue Emitter”. en. In: *Organic Letters* 7.10 (May 2005), pp. 1979–1982. ISSN: 1523-7060, 1523-7052.
- [78] J. Campbell Scott. “Metal–organic interface and charge injection in organic electronic devices”. en. In: *Journal of Vacuum Science & Technology A: Vacuum, Surfaces, and Films* 21.3 (May 2003), pp. 521–531. ISSN: 0734-2101, 1520-8559.

- [79] Eduard Tutis, Ivo Batistic, and Detlef Berner. “Injection and strong current channeling in organic disordered media”. en. In: *Physical Review B* 70.16 (Oct. 2004). ISSN: 1098-0121, 1550-235X.
- [80] Zheng Liu and Qihuang Gong. “Enhancement of light-emitting efficiency of OLED by the electromagnetic-wave tunneling”. en. In: *Physics Letters A* 359.6 (Dec. 2006), pp. 733–736. ISSN: 03759601.
- [81] Woo Sik Jeon et al. “Ideal host and guest system in phosphorescent OLEDs”. en. In: *Organic Electronics* 10.2 (Apr. 2009), pp. 240–246. ISSN: 15661199.
- [82] K.O. Cheon and J. Shinar. “Bright white small molecular organic light-emitting devices based on a red-emitting guest–host layer and blue-emitting 4,4-bis(2,2-diphenylvinyl)-1,1-biphenyl”. en. In: *Applied Physics Letters* 81.9 (Aug. 2002), pp. 1738–1740. ISSN: 0003-6951, 1077-3118.
- [83] Shizuo Tokito et al. “Confinement of triplet energy on phosphorescent molecules for highly-efficient organic blue-light-emitting devices”. en. In: *Applied Physics Letters* 83.3 (July 2003), pp. 569–571. ISSN: 0003-6951, 1077-3118.
- [84] Kenichi Goushi et al. “Triplet exciton confinement and unconfinement by adjacent hole-transport layers”. en. In: *Journal of Applied Physics* 95.12 (June 2004), pp. 7798–7802. ISSN: 0021-8979, 1089-7550.
- [85] S. R. Forrest, M. A. Baldo, and M. E. Thompson. “High-efficiency fluorescent organic light-emitting devices using a phosphorescent sensitizer”. In: *Nature* 403.6771 (Feb. 2000), pp. 750–753. ISSN: 00280836.
- [86] Cheng-Han Yang et al. “Blue-Emitting Heteroleptic Iridium(III) Complexes Suitable for High-Efficiency Phosphorescent OLEDs”. de. In: *Angewandte Chemie* 119.14 (Mar. 2007), pp. 2470–2473. ISSN: 00448249, 15213757.
- [87] Chihaya Adachi et al. “Nearly 100% internal phosphorescence efficiency in an organic light-emitting device”. en. In: *Journal of Applied Physics* 90.10 (Nov. 2001), pp. 5048–5051. ISSN: 0021-8979, 1089-7550.
- [88] Jiangshan Chen and Dongge Ma. “Effect of dye concentration on the charge carrier transport in molecularly doped organic light-emitting diodes”. en. In: *Journal of Applied Physics* 95.10 (May 2004), pp. 5778–5781. ISSN: 0021-8979, 1089-7550.
- [89] Neetu Chopra et al. “Effect of the Charge Balance on High-Efficiency Blue-Phosphorescent Organic Light-Emitting Diodes”. en. In: *ACS Applied Materials & Interfaces* 1.6 (June 2009), pp. 1169–1172. ISSN: 1944-8244, 1944-8252.
- [90] Yong-Jin Pu et al. “Optimizing the Charge Balance of Fluorescent Organic Light-Emitting Devices to Achieve High External Quantum Efficiency Beyond the Conventional Upper Limit”. en. In: *Advanced Materials* 24.13 (Apr. 2012), pp. 1765–1770. ISSN: 09359648.
- [91] Qi Wang and Hany Aziz. “Degradation of Organic/Organic Interfaces in Organic Light-Emitting Devices due to Polaron–Exciton Interactions”. en. In: *ACS Applied Materials & Interfaces* 5.17 (Sept. 2013), pp. 8733–8739. ISSN: 1944-8244, 1944-8252.

- [92] Sebastian Reineke, Karsten Walzer, and Karl Leo. “Triplet-exciton quenching in organic phosphorescent light-emitting diodes with Ir-based emitters”. en. In: *Physical Review B* 75.12 (Mar. 2007). ISSN: 1098-0121, 1550-235X.
- [93] Rico Meerheim et al. “Influence of charge balance and exciton distribution on efficiency and lifetime of phosphorescent organic light-emitting devices”. en. In: *Journal of Applied Physics* 104.1 (July 2008), p. 014510. ISSN: 0021-8979, 1089-7550.
- [94] Pascal Friederich et al. “Molecular origin of the charge carrier mobility in small molecule organic semiconductors”. In: *Adv. Functional Mater.* 26.31 (2016), pp. 5757–5763.
- [95] Tobias Neumann et al. “Modeling disordered morphologies in organic semiconductors”. en. In: *Journal of Computational Chemistry* 34.31 (2013), pp. 2716–2725. ISSN: 01928651.
- [96] Mosè Casalegno, Guido Raos, and Riccardo Po. “Methodological assessment of kinetic Monte Carlo simulations of organic photovoltaic devices: The treatment of electrostatic interactions”. en. In: *The Journal of Chemical Physics* 132.9 (Mar. 2010), p. 094705. ISSN: 0021-9606, 1089-7690.
- [97] Toshinori Matsushima et al. “Optical, morphological, structural, electrical, molecular orientation, and electroluminescence characteristics of organic semiconductor films prepared at various deposition rates”. en. In: *Thin Solid Films* 520.6 (Jan. 2012), pp. 2283–2288. ISSN: 00406090.
- [98] Shigeki Naka et al. “Carrier transport properties of organic materials for EL device operation”. en. In: *Synthetic Metals* 111-112 (June 2000), pp. 331–333. ISSN: 03796779.
- [99] S. C. Tse, K. C. Kwok, and S. K. So. “Electron transport in naphthylamine-based organic compounds”. en. In: *Applied Physics Letters* 89.26 (Dec. 2006), p. 262102. ISSN: 0003-6951, 1077-3118.
- [100] C. H. Cheung et al. “Using thin film transistors to quantify carrier transport properties of amorphous organic semiconductors”. en. In: *Applied Physics Letters* 93.8 (Aug. 2008), p. 083307. ISSN: 0003-6951, 1077-3118.
- [101] J. Cottaar, R. Coehoorn, and P. A. Bobbert. “Scaling theory for percolative charge transport in molecular semiconductors: Correlated versus uncorrelated energetic disorder”. en. In: *Physical Review B* 85.24 (June 2012). ISSN: 1098-0121, 1550-235X.
- [102] J. Cottaar et al. “Scaling Theory for Percolative Charge Transport in Disordered Molecular Semiconductors”. en. In: *Physical Review Letters* 107.13 (Sept. 2011). ISSN: 0031-9007, 1079-7114.
- [103] J. Cottaar. “Ph.D. thesis,” in: *Eindhoven University of Technology* (2012).
- [104] N.S. Hush. “Distance Dependence of Electron Transfer Rates”. en. In: *Coordination Chemistry Reviews* 64 (May 1985), pp. 135–157. ISSN: 00108545.

- [105] Dvira Segal et al. “Electron Transfer Rates in Bridged Molecular Systems 2. A Steady-State Analysis of Coherent Tunneling and Thermal Transitions †”. en. In: *The Journal of Physical Chemistry B* 104.16 (Apr. 2000), pp. 3817–3829. ISSN: 1520-6106, 1520-5207.
- [106] C. Lambert, G. Noll, and J. Schelter. “Bridge-mediated hopping or superexchange electron-transfer processes in bis(triarylamine) systems”. In: *Nat Mater* 1.1 (2002), pp. 69–73.
- [107] Jing Zhang et al. “Sulfur-Bridged Annulene-TCNQ Co-Crystal: A Self-Assembled Molecular Level Heterojunction with Air Stable Ambipolar Charge Transport Behavior”. en. In: *Advanced Materials* 24.19 (May 2012), pp. 2603–2607. ISSN: 09359648.
- [108] Lingyun Zhu et al. “Prediction of Remarkable Ambipolar Charge-Transport Characteristics in Organic Mixed-Stack Charge-Transfer Crystals”. en. In: *Journal of the American Chemical Society* 134.4 (Feb. 2012), pp. 2340–2347. ISSN: 0002-7863, 1520-5126.
- [109] Lingyun Zhu et al. “Electronic Properties of Mixed-Stack Organic Charge-Transfer Crystals”. en. In: *The Journal of Physical Chemistry C* 118.26 (July 2014), pp. 14150–14156. ISSN: 1932-7447, 1932-7455.
- [110] Yuichiro Kawamura et al. “Intermolecular Interaction and a Concentration-Quenching Mechanism of Phosphorescent Ir(III) Complexes in a Solid Film”. en. In: *Physical Review Letters* 96.1 (Jan. 2006). ISSN: 0031-9007, 1079-7114.
- [111] H. van Eersel et al. “Monte Carlo study of efficiency roll-off of phosphorescent organic light-emitting diodes: Evidence for dominant role of triplet-polaron quenching”. en. In: *Applied Physics Letters* 105.14 (Oct. 2014), p. 143303. ISSN: 0003-6951, 1077-3118.
- [112] P. M. Borsenberger, E. H. Magin, and S. A. Visser. “Charge Trapping in Molecularly Doped Polymers”. en. In: *Japanese Journal of Applied Physics* 37.Part 1, No. 4A (Apr. 1998), pp. 1945–1949. ISSN: 0021-4922, 1347-4065.
- [113] Y Y Yimer, P A Bobbert, and R Coehoorn. “Charge transport in disordered organic host–guest systems: effects of carrier density and electric field”. In: *Journal of Physics: Condensed Matter* 20.33 (Aug. 2008), p. 335204. ISSN: 0953-8984, 1361-648X.
- [114] Joshua Jortner et al. “Charge transfer and transport in DNA”. In: *Proceedings of the National Academy of Sciences* 95.22 (1998), pp. 12759–12765.
- [115] Christoph Lambert, Gilbert Noell, and Juergen Schelter. “Bridge-mediated hopping or superexchange electron-transfer processes in bis (triarylamine) systems”. In: *Nature materials* 1.1 (2002), pp. 69–73.
- [116] Pascal Friederich. “phd-thesis: Simulation of Charge Transport in Amorphous Semi-Conductors”. In: *Karlsruhe Institute of Technology* (2016).

-
- [117] Anna B. Chwang, Raymond C. Kwong, and Julie J. Brown. “Graded mixed-layer organic light-emitting devices”. en. In: *Applied Physics Letters* 80.5 (Feb. 2002), pp. 725–727. ISSN: 0003-6951, 1077-3118.
- [118] S. L. M. van Mensfoort et al. “Predictive modeling of the current density and radiative recombination in blue polymer-based light-emitting diodes”. en. In: *Journal of Applied Physics* 109.6 (Mar. 2011), p. 064502. ISSN: 0021-8979, 1089-7550.
- [119] Gregory D. Scholes. “Long Range Resonance Energy Transfer In Molecular Systems”. en. In: *Annual Review of Physical Chemistry* 54.1 (Oct. 2003), pp. 57–87. ISSN: 0066-426X, 1545-1593.
- [120] D. L. Dexter. “A Theory of Sensitized Luminescence in Solids”. en. In: *The Journal of Chemical Physics* 21.5 (May 1953), pp. 836–850. ISSN: 0021-9606, 1089-7690.
- [121] Minlu Zhang et al. “Bulk Heterojunction Photovoltaic Cells with Low Donor Concentration”. en. In: *Advanced Materials* 23.42 (Nov. 2011), pp. 4960–4964. ISSN: 09359648.
- [122] Koen Vandewal et al. “Increased Open-Circuit Voltage of Organic Solar Cells by Reduced Donor-Acceptor Interface Area”. en. In: *Advanced Materials* 26.23 (June 2014), pp. 3839–3843. ISSN: 09359648.

List of Publications

Articles

1. Igor Beljakov, Velimir Meded, Franz Symalla, Karin Fink, Sam Shallcross, Wolfgang Wenzel
Magnetic anisotropy of graphene quantum dots decorated with a ruthenium adatom
Beilstein J. Nanotechnol. **2013**, 4, Pages 441–445.
2. Igor Beljakov, Velimir Meded, Franz Symalla, Karin Fink, Sam Shallcross, Mario Ruben and Wolfgang Wenzel
Spin-Crossover and Massive Anisotropy Switching of 5d Transition Metal Atoms on Graphene Nanoflakes
Nano Lett., **2014**, 14(6), Pages 3364-3368
3. Pascal Friederich, Franz Symalla, Velimir Meded, Tobias Neumann and Wolfgang Wenzel
Ab initio treatment of disorder effects in amorphous organic materials: Toward parameter free materials simulation
J. Chem. Theory Comput., **2014**, 10 (9), Pages 3720-3725
4. Pascal Friederich, Velimir Meded, Franz Symalla, Marcus Elstner and Wolfgang Wenzel
QM/QM Approach to Model Energy Disorder in Amorphous Organic Semiconductors
J. Chem. Theory Comput., **2015**, 11 (2), Pages 560-567
5. Franz Symalla, Sam Shallcross, Igor Beljakov, Karin Fink, Wolfgang Wenzel and Velimir Meded
Band-gap engineering with a twist: Formation of intercalant superlattices in twisted graphene bilayers
Phys. Rev. B., **2015**, 91,205412
6. Vadim Rodin, Franz Symalla, Velimir Meded, Pascal Friederich, Denis Danilov, Angela Poschlad, Gabriele Nelles, Florian von Wrochem and Wolfgang Wenzel
Generalized effective-medium model for the carrier mobility in amorphous organic semiconductors
Phys. Rev. B, **2015**, 91, 155203
7. Velimir Meded, Pascal Friederich, Franz Symalla, Tobias Neumann, Denis Danilov and Wolfgang Wenzel
A self-consistent first-principle based approach to model carrier mobility in organic materials
AIP Conf. Proc., **2015**, 1702, 090027
8. Andrea Massé, Pascal Friederich, Franz Symalla, Wolfgang Wenzel, Robert Nitsche, Reinder Coehoorn and Peter A. Bobbert

- Ab-initio charge-carrier mobility model of amorphous molecular semiconductors*
Physical Review B, **2016**,93 (19), 195209
9. Pascal Friederich, Velimir Meded, Angela Poschlad, Tobias Neumann, Vadim Rodin, Vera Stehr, Franz Symalla, Denis Danilov, Gesa Lüdemann, Reinhold F. Fink, Ivan Kondov, Florian von Wrochem and Wolfgang Wenzel
Molecular origin of the charge carrier mobility in small molecule organic semiconductors
Advanced Functional Materials, **2016**, 26 (31), 5757-5763
 10. Tobias Neumann, Jianxi Liu, Tobias Wächter, Pascal Friederich, Franz Symalla, Alexander Welle, Veronica Mugnaini, Velimir Meded, Michael Zharnikov, Christof Wöll and Wolfgang Wenzel
Superexchange Charge Transport in Loaded Metal Organic Frameworks
ACS nano , **2016**,10 (7), 7085-7093
 11. Feilong Liu, Andrea Masse, Pascal Friederich, Franz Symalla, Robert Nitsche, Wolfgang Wenzel, Reinder Coehoorn and Peter A. Bobbert
Ab initio modeling of steady-state and time-dependent charge transport in hole-only alpha-NPD devices
Applied Physics Letters, **2016**, 109 (24), 243301
 12. Franz Symalla, Pascal Friederich, Andrea Massé, Velimir Meded, Reinder Coehoorn, Peter Bobbert and Wolfgang Wenzel
Charge transport by superexchange in molecular host-guest systems Physical Review Letters , **2016**, 117 (27), 276803
 13. Andrea Massé, Pascal Friederich, Franz Symalla, Feilong Liu, Velimir Meded, Reinder Coehoorn, Wolfgang Wenzel, Peter A Bobbert
Effects of energy correlations and superexchange on charge transport and exciton formation in amorphous molecular semiconductors: An ab initio study
accepted in PRB

Acknowledgement

Prof. Dr. Wolfgang Wenzel and Prof. Dr. Gerd Schön I would like to thank for refereeing my thesis in particular for their flexibility in the end. Thank you, Wolfgang, for giving me the opportunity and support to work on exciting research topics and also giving me the freedom to follow my own projects.

I would like to thank my roommates Pascal Friederich and Manuel Rommel for countless discussions, ideas and support during my time at the INT.

Dr. Velimir Meded I empathetically thank for freely sharing his music, discussing interesting ideas and giving support of all kind.

I would like to thank everyone from AG Wenzel for fun discussions, being nice people and helping me with whatever, whenever needed, in particular Dr.Timo Strunk for sharing his bottomless IT-knowledge and his *unique jokes*.

Last but not least, I thank my wife Alexandra for her support and dish washing during the end of the thesis.